University of Louisville
ThinkIR: The University of Louisville's Institutional Repository

Electronic Theses and Dissertations

5-2015

Nanoscale electrode architectures for electrochemical energy conversion and storage.

Venkat Kalyan Vendra
University of Louisville

Follow this and additional works at: http://ir.library.louisville.edu/etd

 Part of the Chemical Engineering Commons

Recommended Citation
Vendra, Venkat Kalyan, "Nanoscale electrode architectures for electrochemical energy conversion and storage." (2015). *Electronic Theses and Dissertations.* Paper 2071.
https://doi.org/10.18297/etd/2071

This Doctoral Dissertation is brought to you for free and open access by ThinkIR: The University of Louisville's Institutional Repository. It has been accepted for inclusion in Electronic Theses and Dissertations by an authorized administrator of ThinkIR: The University of Louisville's Institutional Repository. This title appears here courtesy of the author, who has retained all other copyrights. For more information, please contact thinkir@louisville.edu.

NANOSCALE ELECTRODE ARCHITECTURES FOR ELECTROCHEMICAL ENERGY CONVERSION AND STORAGE

By

Venkat Kalyan Vendra
B.S., Andhra University, 2008
M.S., Clarkson University, 2010

A Dissertation
Submitted to the Faculty of the
J.B. Speed School of Engineering
at the University of Louisville
in Partial Fulfillment of the Requirements
for the Degree of

Doctor of Philosophy
in Chemical Engineering

Department of Chemical Engineering
University of Louisville
Louisville, KY 40292

May 2015

© Copyright 2015 by Venkat Kalyan Vendra
All rights reserved

NANOSCALE ELECTRODE ARCHITECTURES FOR ELECTROCHEMICAL ENERGY CONVERSION AND STORAGE

By

Venkat Kalyan Vendra
B.S., Andhra University, 2008
M.S., Clarkson University, 2010

A Dissertation Approved on

March 30, 2015

by the following Dissertation Committee:

_____
Dissertation Director
Dr. Delaina A. Amos

_____
Dissertation Director
Dr. Mahendra K. Sunkara

_____
Dr. Frank Zamborini

_____
Dr. Thomas Starr

_____
Dr. Shamus McNamara

DEDICATION

This dissertation is dedicated to my teachers and parents. A special feeling of gratitude to my dear and loving parents Mr. Satyanarayana Murthy and Mrs. Sita Mahalakshmi, and all my childhood teachers who taught me the most important lessons in life.

ACKNOWLEDGEMENTS

I owe a great deal to my advisors, mentors and fellow students. I would like to begin by thanking Dr. Thad Druffel for his mentoring, for all the interesting discussions we had on my solar cell work. I feel fortunate to have two great people – Dr. Delaina Amos and Dr. Mahendra Sunkara as my advisors and acknowledge them for their invaluable motivation and guidance throughout my doctoral degree. Dr. Sunkara was the reason I came to work at the University of Louisville. I met him while finishing my Masters at Clarkson University and was very excited to hear about the work from his research group. I was amazed at his ability to motivate people and to put things into perspective. I learned several important life skills from him and I am a better person for knowing him. Sincere thanks to Dr. Amos for her help in planning my experiments and her guidance in planning my career. I would also like to acknowledge my lab mates- Tu Nguyen, Maria Carreon, Ben Russell, Swathi Sunkara, Alejandro Martinez, Daniel Jaramillo, Apollo Nambo, Brandon Lavery, Gabriel Draper and Patrick for all the technical discussions we had. I will always remember that discussing interesting problems with my advisors and lab mates and coming up with new ideas as most enjoyable times I had during my PhD. I would also like to thank the postdoctoral researchers that I had the pleasure of working with – Dr. Sudesh Kumari, Dr. Arjun Thapa and Dr. Ruvini Dharamdasa for their assistance with my work. Special thanks to Dr. Jacek Jasinksi for all the interesting discussions and his lectures on structural characterization techniques. Last but not the least, I would like to acknowledge Patty Lumley for her patience and all her reminders about registering for classes on time.

ABSTRACT

NANOSCALE ELECTRODE ARCHITECTURES FOR ELECTROCHEMICAL ENERGY CONVERSION AND STORAGE

Venkat KalyanVendra

March 30, 2015

Nanoscale electrode architectures are at the heart of photoelectrochemical devices converting sunlight into electricity and electrochemical devices that store energy. Advanced nanomaterials encompassing 1-D architectures such as single crystalline metal oxide nanowires, 2-D architectures such graphene nanosheets and nanoparticle-nanowire hybrids have garnered significant interest as promising materials for fabricating thicker electrodes due their unique electronic, phase transformation and strain relaxation properties. However, electrode architectures incorporating these advanced nanomaterials will have a transformational impact on large scale electrode manufacturing only if the challenges associated with the electrode durability are addressed. At a fundamental level, the reactions happening at the electrode-electrolyte interface need to be studied in detail in order to address the durability issues. The overall objective of this dissertation is to develop electrode architectures with high durability for solar energy conversion and storage by employing engineered materials with excellent charge transport and charge separation properties. Specifically, electrodes architectures that enable high durability for dye-sensitized solar cells using alternate redox electrolytes and moisture resistant perovskite solar cells, and lithium manganese oxide cathodes for Li ion batteries have been developed.

In dye-sensitized solar cells, there is immense interest in replacing the conventionally used, highly corrosive iodide redox electrolyte with non-corrosive one-electron redox electrolytes that can result in higher cell stability. However, a major shortcoming of one-electron redox electrolytes is their fast electron recombination kinetics when compared to the iodide electrolyte. To address this issue, tin oxide nanowires are investigated as an alternative for conventionally used titania nanoparticles in dye sensitized solar cells. Further, hybrid architectures comprising of titania nanoparticles-tin oxide nanowires are found to be effective in overcoming the limitations of low dye adsorption and low open-circuit voltage, posed by nanowire electrodes. To gain deeper insight into the electron transport and recombination kinetics of different electrode architectures in conjunction with different redox electrolytes, fundamental studies are performed using electrochemical techniques. In addition, the application of alternate absorbers in solar cells is crucial in attempting to address the challenges posed by the state-of-the art dyes. Of particular interest are the metal-organic hybrid perovskites that have high absorption coefficient and excellent hole conductivity. Though perovskites have resulted in breakthrough performance for solar cells, degradation of perovskites due to moisture is a huge road block limiting the progress of perovskite solar cells. The moisture instability of perovskites is addressed using a novel concept of a thick, highly conductive graphene-conductive polymer composite for the encapsulation of the perovskite nanocrystals.

Electrode architectures for highly durable cathode materials for application in Li ion batteries have also been developed in this dissertation. Most of the widely investigated anodes have higher capacity when compared to the cathodes. In order to balance the capacity of both electrodes, the cathodes need to be made thicker. Nanoparticle

electrodes are not ideal for making thicker electrodes as the poor charge transport characteristics result in increased series in thicker nanoparticle electrodes and subsequently lead to a loss in cell voltage. Further, electrode materials for Li ion batteries require the structural integrity of the material to be maintained through several charge-discharge cycles. Layered transition metal oxides and their alloys have been widely investigated as cathode materials in Li ion batteries due to their potential for achieving high capacity. Poor surface stability and increased strain on the lattice associated with the phase transformation occurring during battery charging and discharging are the major reasons for poor cycle stability of the commonly used layered transition metal cathodes. In this work, single crystalline nanowires of a layered transition metal oxide, namely Li_2MnO_3 are investigated as cathode materials in Li ion batteries in order to address the limitations posed by layered transition metal cathodes. A detailed investigation of the cycled electrodes showed that single crystalline nanowires allow for the facile phase transformation of the Li_2MnO_3 to a zero strain spinel phase of $LiMn_2O_4$. The phase transformation on single crystalline Li_2MnO_3 NWs result in the formation of conformal and thicker (20-30 nm) spinel $LiMn_2O_4$ shell that is very effective in improving the surface stability of the electrodes and hence prevents the capacity loss during cycling.

TABLE OF CONTENTS

PAGE

ACKNOWLEDGEMENTS……v
ABSTRACT……...vi

LIST OF FIGURES……xiii

CHAPTER 1. INTRODUCTION……...1

1.1 Energy challenge……1

1.2 Motivation for this study……...1

1.3 Objectives of this study……11

1.4 Outline of this dissertation……...11

1.5 Intellectual merit and impact of this work……...12

CHAPTER 2. BACKGROUND……15

2.1 Basic principles of photoelectrochemical cells……15

2.1.2 Photoelectrochemical solar cells employing single crystals…….18

2.1.3 Dye-sensitized solar cells (DSCs)……19

2.2 Challenges associated in electrodes architectures in DSCs using alternate redox couples ……21

2.3 Literature attempts to address challenges with one electron electrolytes in DSCs….24

2.3.1 Conformal coatings of insulating layers……24

2.3.2 1-D nanostructures……25

2.3.3 Engineering dye molecules……26

2.4 Perovskites as Alternate Absorbers for Solar Cells ……..27

2.4.1 Attempts to improve moisture stability of perovskites……...29

2.5 Li ion Batteries……30

2.6 Challenges with lithium manganese oxide based cathodes for Li ion batteries….32

2.6.1 $LiMn_2O_4$ based electrodes…….33

2.6.2 Li_2MnO_3 based electrodes…….35

2.7 Literature attempts to address challenges with lithium manganese oxide cathodes…37

2.7.1 Nanowire based architectures……37

2.7.2 Element doping……...37

2.7.3 Surface coating……38

2.7.4 Electrolyte development……..38

CHAPTER 3. EXPERIMENTAL METHODS AND CHARACTERIZATION TECHNIQUES…….40

3.1 Synthesis of tin oxide nanowires by reactive vapor transport……....40

3.2 Solvo-plasma technique for synthesizing metal oxide nanowires…….41

3.3 Atomic layer deposition (ALD)…….43

3.4 Electrophoretic deposition (EPD)……...46

3.5 Procedure for fabricating dye-sensitized solar cells……46

3.6 Procedure for fabricating perovskite solar cells…….50

3.7 Procedure for fabricating Li ion battery coin cells……..52

3.8 Electrochemical Techniques……...53

3.8.1 Current-voltage (I-V) characterization……53

3.8.2 Open circuit-voltage decay technique…….56

3.8.3 Short-circuit current decay……..58

3.8.4 Incident photon to charge carrier conversion efficiency (IPCE)…….59

3.8.5 Scanning laser spot technique……....60

3.9 Structural Characterization…….61

3.9.1 Scanning electron microscopy (SEM)……...61

3.9.2 Transmission electron microscopy (TEM)…….62

3.9.3 X-ray diffraction (XRD)……63

CHAPTER 4. FUNDAMENTAL STUDIES OF ELECTRON DYNAMICS IN DYE-SENSITIZED SOLAR CELLS……..64

4.1 Electron dynamics in nanoparticle based architectures……64

4.2 Electron dynamics in nanowires and nanoparticle/nanowire hybrid architectures….75

4.2.1 Studies with iodide/tri-iodide redox couple……..75

4.2.2 Studies with alternate redox couples…….79

4.3 Macroscale effects: Influence of electrode dimensions on electron transport and recombination…….83

4.4 Summary……..96

CHAPTER 5. HYBRID NANOWIRE-NANOPARTICLE ARCHITECTURES FOR DYE-SENSITIZED SOLAR CELLS……..97

5.1 Introduction……97

5.2. Experimental…… 99

5.3. Results and Discussion……102

5.4 Summary……...117

CHAPTER 6. MOSITURE RESISTANT PEROVSKITE SOLAR CELLS……..118

6.1 Introduction …… .118

6.2. Experimental……119

6.3. Results and Discussion…….122

6.4 Summary……..131

CHAPTER 7. LITHIUM INTERCALATION IN NANOWIRE BASED MATERIALS……132

7.1 Introduction……. 132

7.2. Experimental……...133

7.3. Results and Discussion…….....135

7.4 Summary……..151

CHAPTER 8. CONCLUSIONS…….152

CHAPTER 9. RECOMMENDATIONS FOR FUTURE WORK……..154

REFERENCES……156

APPENDIX 1……..165

CURRICULUM VITAE…….167

LIST OF FIGURES

Figure 1.1. Keeling Curve show rapid raise in global CO_2 level with time.

Figure 1.1.1. Schematic describing the fundamental challenges with solar energy conversion & storage.

Figure 1.1.2. Schematic depicting the challenges with conventionally used mesoporous electrodes for photoelectrochemical solar cells and Li ion batteries.

Figure 1.1.3. Schematic depicting the interesting properties of nanowire arrays for use as electrodes in electrochemical cells.

Figure 1.6.1 Impact of using nanowires based architectures for dye-sensitized solar cells

Figure 1.6.2. Impact of using single crystal nanowire cathodes for Li ion batteries

Figure 2.1.1 Energy diagram illustrating (a) energy levels in an n-type semiconductor (b) semiconductor-liquid junction in dark (c) semiconductor-liquid junction under illumination. (d) Schematic illustrating the buildup of a photovoltage in a photoelectrochemical device.

Figure 2.1.2 Schematic depicting photoelectrochemical solar cells employing single crystals.

Figure 2.1.3. Schematic depicting different electron transfer process in a dye-sensitized solar cell.

Figure 2.2. State of the art of different redox electrolytes (from References 2-12) used for dye-sensitized solar cells for the conventional Ru based dyes (a) and (b) alternative dyes

Figure 2.3.1. Schematic illustrating fast electron transport in nanowires electrodes

Figure 2.3.2. Schematic illustrating electron recombination from trap states in SnO_2 NWs and TiO_2 NPs.

Figure 2.4.1 Two dimensional representation of the layered $(R\text{-}NH_3)_2\ MX_4$ perovskite.

Figure 2.4.2 .Proposed pathways for degradation of methyl ammonium lead iodide perovskites in the presence of water.

Figure 2.5.1 Schematic illustrating the working principle of a Li ion battery

Figure 2.6.1. Comparison of operating voltage and capacity of different transition metal oxides used as cathode for Li ion batteries.

Figure 2.6.2. Crystal structure of cubic $LiMn_2O_4$ and tetragonal $Li_2Mn_2O_4$ drawn using Crystal Maker™ software.

Figure 2.6.3. Crystal structure of layered Li_2MnO_3drawn using Crystal Maker™ software.

Figure 2.7 Reaction showing HF scavenging using HEDMS electrolyte additive.

Figure 3.1(a) Schematic of the low pressure CVD reactor using for synthesizing tin oxide NWs (b) picture of the reactor showing the quartz window for temperature measurement (c) alumina coated tungsten basket connected to copper feedthroughs.

Figure 3.2. Atmospheric upstream microwave plasma reactor used for the solvo-plasma technique.

Figure 3.3 Schematic of the ALD reactor setup

Figure 3.5.1. Schematic showing the different components of a DSC.

Figure 3.7.1. Different components used in the assembly of a Li ion coin cell.

Figure 3.8.1. Schematic depicting the equivalent circuit of a solar cell.

Figure 3.8.2. I-V characteristic curve of a solar cell under illumination. The dotted lines in red show the deviation of the I-V curve due to different losses within the cell.

Figure 3.8.3 (a) Schematic illustrating the experimental setup for performing the open-cicrcuit voltage decay method (b) Typical plots of open-circuit voltage decay and plot of electron lifetimes calculated using the voltage decay.

Figure 3.8.4. Schematic showing the experimental setup for the scanning laser spot technique to monitor current density and voltage variations across the width of the cell.

Figure 4.1.1 Schematic depicting the formation of bridges between commercially available P25 TiO_2 NPs to improve electron transport and lower electron recombination.

Figure 4.1.2 XRD diffraction pattern of anatase nanoparticles (NP) formed from thermal decomposition of TALH at 500 ℃.

Figure 4.1.3. Transmission electron microscopy image of titanium dioxide nanoparticles after sintering – (a) P25 nanoparticles (b) anatase titanium dioxide NPs from TALH sintered at 500ºC and (c) P25 nanoparticles with anatase nanoparticle bridging formed from TALH.

Figure 4.1.4 (a) Current-Voltage characteristics, (b) overall efficiency of DSCs fabricated with formulations containing different concentrations of TALH with active and layer only

and, (c) Current-Voltage curve for an optimized formulation with both active layer and scattering layer.

Figure 4.1.5 (a) Electron transport time constant and (b) electron lifetimes for DSCs fabricated with varying amounts of TALH.

Figure 4.1.6 (a) XPS spectrum for different TALH concentrations (b) chronoampereometry measurements at -0.8 V Ag/AgCl in a 0.5 M $LiClO_4$ electrolyte, inset shows the surface density of trap states, at varying concentrations of TALH.

Figure 4.1.7. Scanning electron images of titanium dioxide films fabricated with formulations containing varying amount of TALH (a) 0 M TALH (b) 0.14 M TALH (c) 0.43 M TALH (d) 1.30 M TALH. (e) Absorbance of N-719 dye on the titanium dioxide films fabricated with varying TALH concentrations.

Figure 4.2.1.1. Electron lifetimes in tin oxide NWs, tin oxide NPs and tin oxide NW/titania NP Hybrids.

Figure 4.2.1.2. (a) Electron transport and (b) recombination time scales in DSC with titania NW and NP based architectures using iodide redox couple.

Figure 4.2.1.3. Electron lifetimes in tin oxide NW/titania nanoparticle architectures and titania nanoparticles in DSCs fabricated with alternate one-electron redox couples.

Figure 4.2.1.4. Electron transport times scales in tin oxide NW/titania nanoparticle architectures in DSCs fabricated with alternate one-electron redox couples.

Figure 4.2.1.5 Electron lifetimes in different electrode architectures passivated with Al_2O_3in DSCs using TEMPO redox couple.

Figure 4.2.1.6 Band edge offsets between the core and shell of the hybrid architectures prepared in this work, prevent back electron transfer from the core back to the shell.

Figure 4.3.1. (a) Short-circuit current density and (b) Efficiency of DSCs fabricated using P25 titania nanoparticles as a function of photoanode area at 1 sun illumination (100 mW/cm^2). Inset shows the change in short-circuit current density vs. area for larger cell areas.

Figure 4.3.2. (a) Fill factor and (b) open-circuit voltage for DSCs of different areas constructed from titania nanoparticles.

Figure 4.3.3. (a) Transport time constants at 1 sun illumination and (b) recombination time scales for cells fabricated from P25 titania nanoparticles as a function of cell area. The error bars represent the standard deviation from the measurements on three cells.

Figure 4.3.4. (a) Short-circuit current density and (b) % efficiency of DSCs fabricated using tin oxide NW and tin oxide NW/titania NP composites as a function of photoanode area at 1 sun illumination, (c) Transport time constants at 1 sun illumination and (d) recombination time constants for cells fabricated from tin oxide nanowires as a function of cell area. The error bars represent the standard deviation from the measurements on three different cells.

Figure 4.3.5 Normalized photovoltage profiles along the lateral dimension of different area P25 nanoparticle based DSCs obtained using the scanning laser spot technique.

Figure 4.3.6 Efficiency vs. area for DSC fabricated with commercially available anatase nanoparticles with only an active layer and with 3-layer configuration. The 3-layer

architecture comprises of a compact layer formed by $TiCl_4$ treatment, an active layer made from commercially available 15 nm anatase nanoparticles (Dyesol). The scattering layer comprised of anatase titania nanoparticles (Dyesol) of 200 nm in diameter.

Figure 4.3.7. Normalized photovoltage profile along the lateral dimension of the cell for DSCs of different areas fabricated using only active layer of anatase titania nanoparticles.

Figure 4.3.8 Normalized photovoltage profile for a 0.04 cm^2 DSC fabricated from P25 nanoparticles and filled with a quasi-solid state electrolyte.

Figure 5.1 J-V characteristics of SnO_2NWs, TiO_2 NPs and $TiCl_4$ treated SnO_2 NWs using ferrocene redox couple at 1 Sun illumination.

Figure 5.2. Dark J-V curves of DSCs tin oxide nanowires, titania nanoparticles and ferrocene-ferrocenium redox couple.

Figure 5.3. J–V curves of DSCs employing ferrocene redox couple with different film thickness of tin oxide NWs

Figure 5.4. J-V curve comparing the performance of unpassivated SnO_2 NWs and TiO_2 NPs under 1 Sun illumination.

Figure 5.5 Band edge location of tin oxide, titania, conventionally used N-719 Ru based dye, ferrocene and TEMPO redox electrolytes.

Figure 5.6. (a) Schematic showing the structure of SnO_2 NW/TiO_2 NP Hybrid architecture (b) SEM image of SnO_2 NWs/TiO_2 NP Hybrid architecture (c) SEM image of TiO_2 NW/TiO_2 NP Hybrid architectures

Figure 5.7. Transmission electron microscopy images of TiO_2 nanoparticle-SnO_2 nanowire hybrid architectures.

Figure 5.8 Current- voltage characteristics of the TiO_2 NP/SnO_2 NW hybrid architecture and TiO_2 NP based DSCs with ferrocene and the tempo redox electrolytes

Figure 5.9. J-V curves for different architectures coated with 1 cycle of Al_2O_3 when using TEMPO redox electrolyte.

Figure 5.10. (a) Comparison of absorbance spectrum of the N-719 sensitized TiO_2 NPs and TiO_2 NP-SnO_2 NW Hybrids (b) picture showing TiO_2 NPs and TiO_2 NP-SnO_2 NW Hybrids after sensitization with N-719 dye.

Figure 5.11. Power conversion efficiency vs. thermodynamic driving force for dye-regeneration for (a) conventional Ru based dye and (b) alternate dyes (organic) plotted from literature.

Figure 6.1.Schematic illustrating the role of graphene/conductive polymer composite as a multifunctional coating that protects the perovskite crystals from moisture while stilling allowing efficient electron and hole transport through encapsulated layer - (a) shows the graphene-conductive polymer composite (b) illustrates the tortuous path of oxygen and water molecules to reach the perovskite encapsulated in the graphene/conductive polymer composite, and efficient electron transport through graphene and hole transport through hole conductive polymer (c) short transport path of water and air molecules towards unprotected perovskite crystals.

Figure 6.2. (a), (b) Time evolution of the XRD pattern of unprotected $CH_3NH_3PbI_3$ perovskite sample and different time degradation of $CH_3NH_3PbI_3$ at 99% relative humidity

(c) Time evolution of the XRD pattern of Graphene/PANI coated $CH_3NH_3PbI_3$ at 99 % relative humidity. XRD pattern of lead iodide and methyl ammonium iodide are also shown for comparison.

Figure 6.3. Images depicting (a) unprotected perovskite sample and (b) graphene/PANI composite coated perovskite sample, after exposure to air at 99 % humidity for 2h.

Figure 6.4. Cross-sectional scanning electron microscopy image of the (a) $CH_3NH_3PbI_3$ solar cell without any protective solar cells, (b) /Graphene/PANI protected $CH_3NH_3PbI_3$solar cell and (c) magnified image of FTO and TiO_2 with Graphene/PANI composite region showing infiltration of the composite into the perovskite.

Figure 6.5. (a) Schematic of the electrode architecture of the moisture perovskite solar cells prepared in this work (b) Energy level diagram showing band edge locations of different materials used in the perovskite cells.

Figure 6.6.TEM image of (a) unprotected $CH_3NH_3PbI_3$crystal and (b) $CH_3NH_3PbI_3$ encapsulated Graphene/PANI composite (c) EDS color map of the encapsulated $CH_3NH_3PbI_3$ in Figure 6.6 (b) indicating complete coverage of the perovskite crystal with the Graphene/PANI composite.

Figure 6.7. Time evolution of the current density–voltage characteristics measured at 1 Sun and AM 1.5 condition as a function of time for(a) unprotected $CH_3NH_3PbI_3$ solar cell (b),(c),(d) Graphene/PANI composite protected perovskite cells with different thickness of composite overlayer. The cells were exposed to air at 99 % relative humidity throughout the duration of the testing.

Figure 6.8.J-V curve of the perovskite solar cell using the graphene-PANI composite coating as the hole transport material. The counter electrode is a gold sputtered glass slide that is sandwiched against the perovskite electrode.

Figure 7.1. Schematic of the solvo-plasma process for synthesizing MnO_2 NWs followed by solid-state alloying to prepare Li_2MnO_3 NWs.

Figure 7.3. (a) Charge and discharge capacities, columbic efficiency of manganese oxide NWs for the first 12 cycles at 0.2 C rate(b) Charge and discharge voltage profiles for the cycles 1 and 10.

Figure 7.4. (a) Scanning electron microscopy image shows that the morphology of the MnO_2 NW is still retained after 10 cycles, (b) cyclic voltammogram of the MnO_2 NWs.

Figure 7.2 (a) SEM image of the as synthesized Li2MnO3 NWs and (b) TEM image of the as-synthesized Li_2MnO3 NW

Figure 7.5. Cyclic voltammogram of Li_2MnO_3NWs at a scan rate of 1 mV/s (b) HRTEM image of single crystallineLi_2MnO_3NWs.

Figure 7.6. Charge-discharge capacity curves and cycleability of Li_2MnO_3NWs at (a) 1C-rate and (b) at 5 C-rate respectively.

Figure 7.7. XRD of (a) as-synthesized Li_2MnO_3 nanowires (b) Li_2MnO_3 NWs discharged to 3.5 V and (c) Li_2MnO_3 NWs discharged to 2 V.

Figure 7.8. (a) & (b) HRTEM images of Li_2MnO_3 NWs discharged to 2 V and (c) HRTEM image of Li_2MnO_3 NW discharged to 3.5 V.

Figure 7.9. HRTEM images showing a polycrystalline shell along Li_2MnO_3 NWs discharged to 2 V.

Figure 7. 10 (a) and (c) depict the SAED pattern of the sample discharged to 3.5 V and 2V respectively. (b) and (d) show the rotational average analysis of these SAED patterns respectively.

Figure 7.11. Schematic illustrating the formation of a $LiMn_2O_4$ shell on the Li_2MnO_3 NWs.

Figure 7.12. Charge-Discharge curves for Li_2MnO_3 NWs cycled in the 2 V to 4.8 V voltage window.

Figure 7.13.C-rate test of Li_2MnO_3 NWs at different current densities.

CHAPTER 1

INTRODUCTION

1.1 Energy Challenge

As Nobel laureate Richard Smalley noted, energy will be the top most challenging problem facing mankind for the next several years.[1] The cost of producing solar electricity is still considerably higher than electricity generated from coal and natural gas. It has been estimated that less than 0.1 % of our total electricity is generated from solar panels.[2] It is well known that CO_2 emissions from burning fossil fuels pose a major problem. The Keeling curve (Figure 1.1), based on the data taken from the Mauna Loa observatory in Hawaii, shows an exponential increase in the CO_2 levels in the past few years.

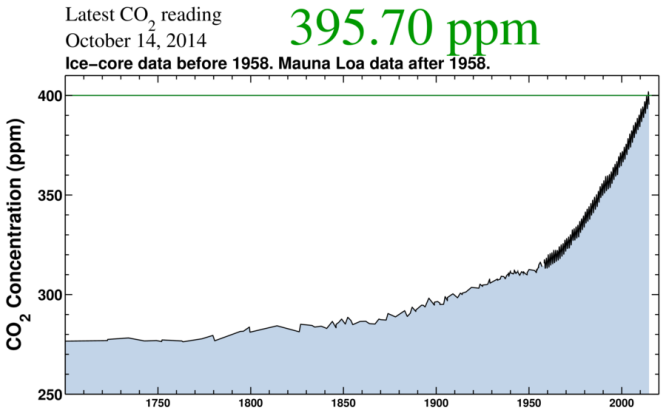

Figure1.1.0 Keeling Curve show rapid raise in global CO_2 level with time. (Source: https://scripps.ucsd.edu/programs/keelingcurve).

Several reports indicate that the current CO_2 readings have reached the 400 ppm milestone and suggest that increase in CO_2 levels beyond 450 ppm could result in

catastrophic changes in the climate.[3] Hence, there is an urgent need for carbon neutral energy production.

In order to compete with costs of fossil fuels, breakthrough technologies that can harness and store solar energy efficiently need to be developed. Nanoscale materials possessing interesting charge transport and phase transformation properties can play a key role in developing these technologies if the challenges associated with controlling interfacial reactions and phase transformations are engineered for optimum device performance and durability. Therefore, successful integration of nanoscale electrode architectures into electrochemical devices require fundamental measurements to understand how the nanostructure, defects, charge transport, nanoscale phase transformation and surface composition effect the electrochemical device performance.

Commercially viable solution: A commercially viable solution to address this urgent clean energy demand is to harness sunlight using solar cells and store it in Li ion batteries. Figure 1.1.1 depicts this scheme and describes the basic challenges in implementing this scheme.

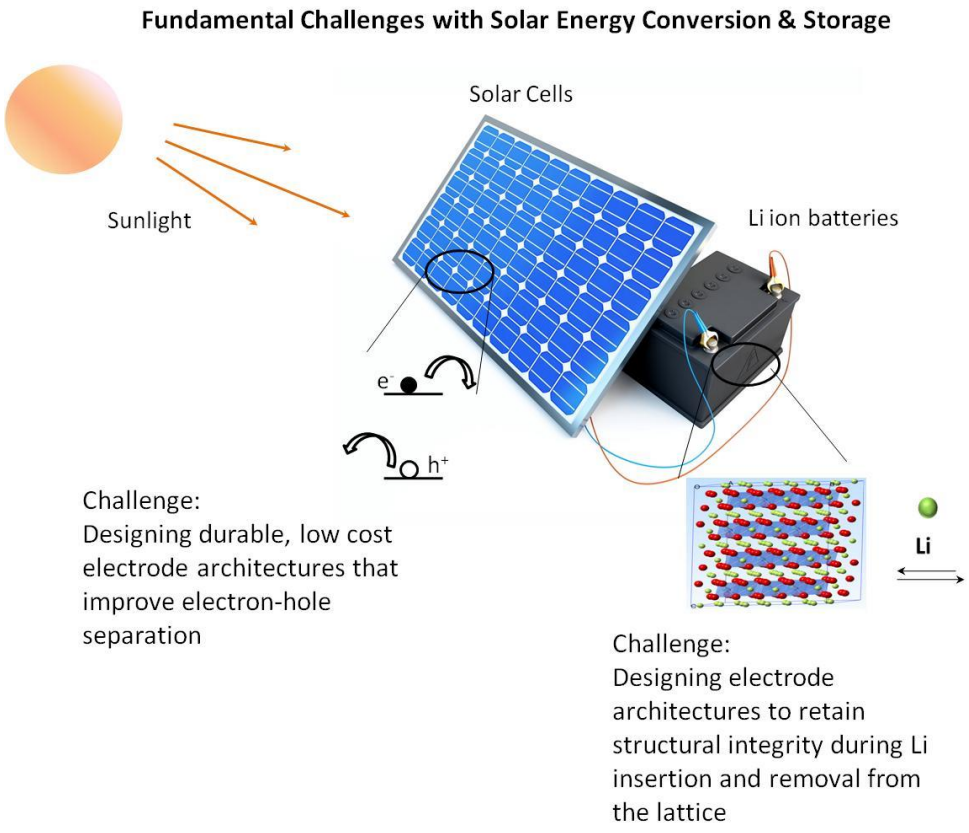

Figure 1.1.1. Schematic describing the fundamental challenges with solar energy conversion & storage.

Mesoporous semiconductor electrodes having a high surface area are typically employed as electrode materials in photoelectrochemical solar cells and Li ion batteries. In both these electrochemical devices there is a strong need for developing electrode architectures that enable the use of thicker electrodes. This requirement is explained in more details as follows. The development of electrodes for solar cells requires that the electrode architectures enable efficient light harvesting and electron-hole separation. Diffusion length of the charge carriers, defined as the minimum distance the charge carriers diffuse in the semiconductor network before they recombine, is typically small (on the order of hundreds of nanometers) for nanoparticle electrodes.[4] This small diffusion

length in conventionally used nanoparticle electrodes is a direct consequence of recombination at grain boundaries and trap limited diffusive transport of electrons. In the trap limited diffusive transport of electrons, the electrons get trapped and detrapped several times before they finally diffuse and reach the current collecting substrate.[5] Hence, higher number of surface traps in nanoparticles slows down the transport of electrons to the conducting substrate. The low diffusion length in nanoparticle networks places a severe limitation on the thickness of nanoparticle electrodes that can be employed. Hence there is a need to develop electrode architectures that can result in increased thickness of the electrodes to increase light absorption by the electrodes and obtain higher currents from the solar cells.

Development of electrodes for Li ion batteries also have a similar requirement of thicker electrodes. The presence of non-active components such as separator and binder lowers the specific capacity of cell. For example, it has been reported that graphite/$LiNi_xMn_yCo_{1-x-y}O_2$ cells exhibit a specific capacity of 150 mAh/g basing on the weight of active materials.[6] This capacity drops by 60 % (to about 60 mAh/g) if the weight of all the cell components is considered.[6] An interesting approach to address this issue is to increase the thickness of the cathode. Most of the widely investigated anodes have higher capacity when compared to the cathodes. In order to balance the capacity of both electrodes, to prevent overcharging of the cathodes, the cathodes need to be made thicker. Nanoparticle electrodes are not ideal for making thicker electrodes as the poor charge transport characteristics in nanoparticles result in increased series from thicker nanoparticle electrodes and subsequently lead to a loss in cell voltage. In addition, the strain relaxation in not very efficient in a closely packed nanoparticle network due lack of

sufficient free space to accommodate the expansion of the nanoparticles during Li ion insertion. This is even more important when there is a phase transition occurring during Li insertion or removal from the lattice. The change in lattice parameter introduces significant strain on the lattice. The incomplete strain relaxation due to lack of free space for the expansion of nanoparticles leads to the fracturing of the nanoparticles and disrupts the electrical connectivity between the particles. Another key issue with nanoparticle electrodes is the poor interface stability at the electrode-electrolyte interface. Typically the reduction of electrolyte species on the electrode surface results in the formation of a passivating layer, called solid electrolyte interface (SEI), on the electrode that has poor electrical conductivity. Further, the dissolution of surface atoms into the electrolyte is a challenge for many electrode materials. The high surface area of nanoparticle electrodes results in thick SEI formation and higher dissolution of surface atoms resulting in reduced battery performance. Typically a highly conformal protective layer is required for reducing these surface effects.

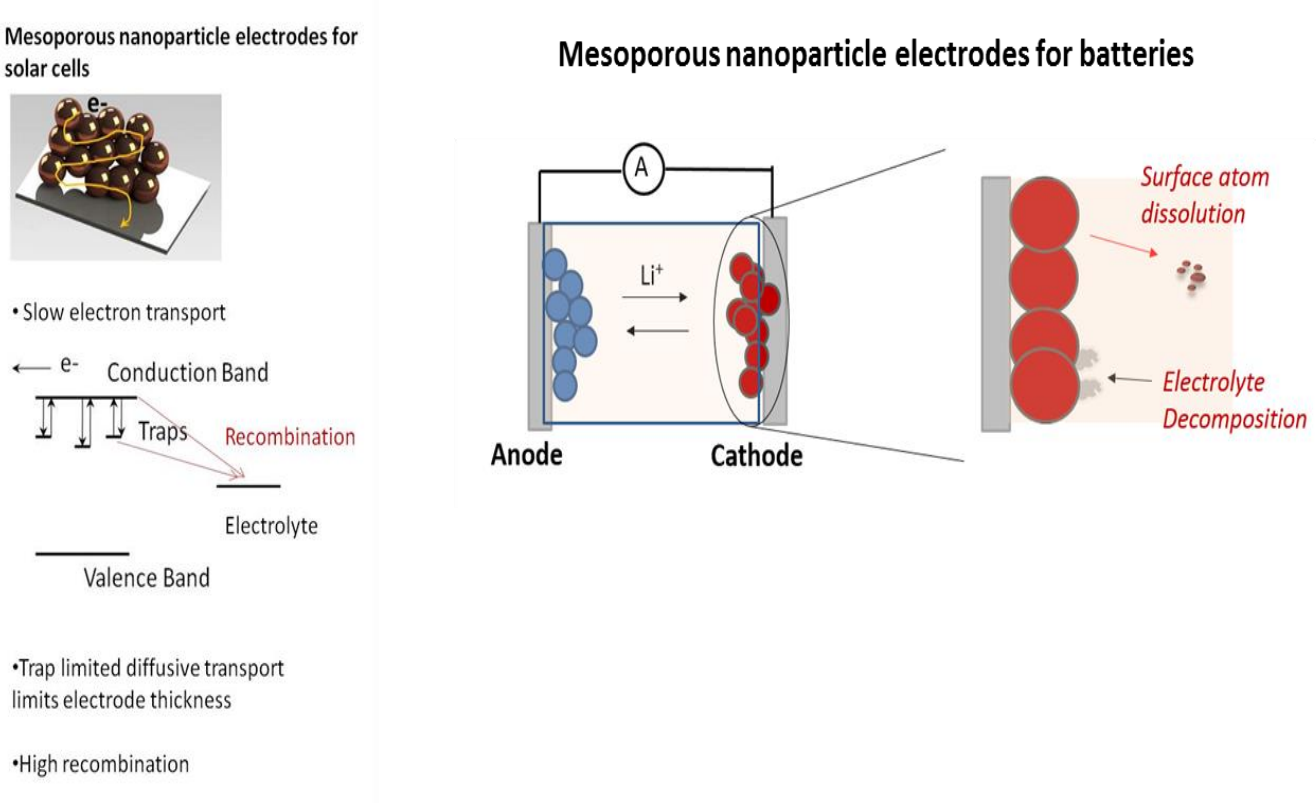

Figure 1.1.2. Schematic depicting the challenges with conventionally used mesoporous electrodes for photoelectrochemical solar cells and Li ion batteries.

In summary, the following are the specific challenges associated with electrodes for solar energy conversion and storage:

- Poor charge transport characteristics in conventionally used nanoparticle electrodes resulting in loss in solar cell and battery performance.
- Lack of durability and long term stability of the electrodes. In case of photoelectrochemical cells the durability is associated with electrolyte and absorber material. Replacing the electrolyte and the absorber requires the proper design of electrode materials as the conventional used nanoparticle architectures result in lowered performance due to their poor electronic properties. Further, fundamental

studies are crucial for the rational design of electrode architectures that result in improved performance.

- In Li ion batteries, retaining the structural and morphological integrity over several charge-discharge cycles is a challenge due to the strain on the lattice of the host material during Li ion insertion and extraction. In addition, understanding the mechanism of phase transformation of these layered lithium transition metal oxides is of significant importance for designing more durable battery electrodes.

The use of nanowires as electrode materials can have several advantages such as fast charge carrier transport, reduced defects because of the single crystallinity, large surface to volume ratio increase chemical reactivity and facile strain relaxation properties. Figure 1.1.3 illustrates the unique properties of these semiconducting nanowires.

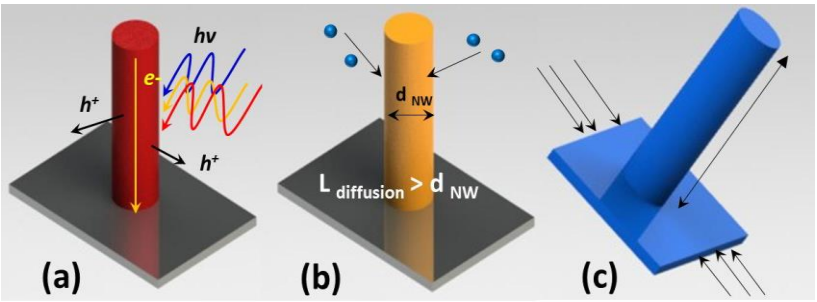

Figure 1.1.3. Schematic depicting the interesting properties of nanowire arrays for use as electrodes in electrochemical cells.

Figure 1.1.3 (a) shows the fast surface charge transport characteristics for photogenerated carriers and low recombination in solar cells. Figure 1.1.3 (b) illustrates smaller diffusion length scales for reacting species toward doping/phase transformation and short diffusion

length scales for minority carriers and Figure 1.1.3 (c) illustrates nanowires being utilized as semi-rigid and strain relaxing substrates for Li ion battery applications.

Similarly, graphene has gained interest due to its high electrical conductivity and has been reported to act as an effective barrier against moisture and oxygen. This should permit the use of graphene as an interesting barrier material where the moisture and oxygen stability of the electrode is challenge.

To enable the use of engineered electrodes for designing electrochemical devices the different charge transfer processes in solar cells and Li insertion/removal reaction mechanisms in Li ion battery cathodes need to be studied in detail.

1.2 Motivation for this study

The overall objective of this dissertation is to develop electrochemical devices such as solar cells and Li ion batteries by using engineered materials with improved electron transport, electron recombination and phase transformation properties.

The following calculation shows the maximum power conversion efficiency than be obtained from a photoelectrochemical solar cell. The calculation will be used to identify the critical parameters necessary to fabricate a high efficiency photoelectrochemical cell.

Assuming an IPCE of 90 %, maximum short-circuit current density is calculated as

$$Jsc_{max} = 0.9 * q \int \emptyset_{\lambda} \left[1 - e^{(-\alpha_{\lambda} \cdot d)}\right] d\lambda$$

For E_g =1.6 eV, Jsc_{max}= 21.7 mA/cm^2,

Maximum open-circuit voltage, Voc_{max} = Band gap- Loss in potential = (1.6-0.2) eV = 1.4 eV

Power conversion efficiency is defined as $\% \eta = \frac{Jsc \,.\, Voc \cdot FF}{P_i} * 100$

Assuming a fill factor of 0.7, the maximum power conversion efficiency that can be obtained can be estimated as 21.3 %.

Hence, the maximum power conversion efficiency is obtained with:

(i) Absorber materials that have high absorption coefficient (α) are required for absorbing high fraction of the incident light and generate a high number of electron-hole pairs. Also this reduces the thickness of the absorber material that is required to absorb most of the incident light (which called absorption depth 1/α).

(ii) Nanoscale electron architectures with fast electron transport time scales and low charge carrier recombination are required for achieving high IPCE and consequently high short-circuit current density. Lower electron recombination losses from the electrode architecture and the oxidized species of the electrolyte are also required for achieving high V_{oc}, defined as the difference between the Fermi-level in the semiconductor and the redox potential of the electrolyte.

(iii) Proper tuning of the energy levels of the redox couple and sensitizer is crucial for achieving low loss potential, which determines the maximum V_{oc} that can be obtained.

In the case of Li ion batteries, it is essential to develop electrode architectures that can

(i) Exhibit high cycling stability by maintaining the structural integrity of the electrode materials

(ii) Have high columbic efficiency by preventing undesirable side reactions that lead to degradation of the electrode materials and subsequent loss in capacity

(iii) Maintain high capacity retention at high C-rates to enable the application of Li ion batteries for commercial scale applications.

Though use of engineered materials such as nanowires as mesoporous electrodes have strong potential to satisfy the above requirements, several fundamental questions such as the following need to be answered to effectively integrate the nanowires into electrochemical devices- Do the electron dynamics in the electrodes vary with change of electrolyte used in photoelectrochemical solar cells? What is the role of traps states and how does it affect the electron dynamics? Does the electrode area affect the electron dynamics, are there any macroscale effects that need to be considered? Can thick conductive protective coatings effectively protect alternate solar cell absorber that are not stable to air and moisture? What is the Li ion intercalation mechanism in nanowire based cathodes?

Hence, the dissertation employs electrochemical and structural characterization techniques to obtain a fundamental insight about the reactions at the electrode interface to enable effective utilization of engineered materials in electrochemical devices.

1.3 Objectives of this dissertation

The following are the specific technical objectives of this work:

- Fundamental investigation of different electron dynamics in the architectures such as charge carrier transport and recombination for understanding the factors limiting the photoelectrochemical performance.
- Understanding the role of surface trap states and their passivation on the photoelectrochemical performance of the nanoparticle and nanowire based architectures.
- Develop electrode architectures for using iodide free redox couples in dye-sensitized solar cells.
- Develop electrode architectures with thick conductive protective coatings that have improved stability against moisture and oxygen when alternate absorbers such metal-organic perovskites are used in solar cells.
- Demonstrate the use of nanowires as interesting strain relaxation platform to relax the strain the associated with phase transformations during Li insertion and removal in cathode materials.

1.4 Outline of this dissertation

This dissertation is divided into nine chapters. Chapter 1 introduces the energy challenge, operating principles of photoelectrochemical solar cells, Li ion batteries and the need for the development of nanoscale electrode architectures for solar energy conversion and electrochemical energy storage. Chapter 2 includes a detailed review of challenges for developing electrode architectures for dye sensitized solar cells, perovskite solar cells and

manganese oxide based cathodes for Li ion batteries and the state-of-the art approaches for addressing these challenges. Chapter 3 describes the experimental methods used for fabricating the electrode architectures and the structural and electrochemical characterization for the electrodes. Chapter 4 investigates the electron transport and recombination characteristics in nanoparticles, nanowires, nanoparticle/nanowire hybrid architectures of titania and tin oxide, with the conventionally used iodide redox couples and alternate redox electrolytes such as ferrocene/ferocenium and TEMPO/$TEMPO^+$ which exhibit fast recombination kinetics. The origin of edge effects and area effects on the efficiency of dye-sensitized solar cells are also described. Chapter 5 discuses the fabrication and electrochemical characterization of iodide free dye-sensitized solar cells employing nanowire/nanoparticle hybrid architectures of titania and tin oxide. Chapter 6 talks about the protection of methyl ammonium lead iodide perovskite absorbers against moisture using novel graphene-conductive polymer protective coatings. A simple sandwich approach for the scalable assembly of perovskite solar cell is also discussed. Chapter 7 describes the application of layered Li_2MnO_3 nanowires as cathode material to develop high rate capacity Li ion batteries with negligible capacity loss during cycling. The mechanism of the formation of a spinel $LiMn_2O_4$ protective shell during the initial charge and discharge cycles and the reasons for high capacity retention is detail.

1.6 Intellectual Merit & Impact of this work

- A fundamental understanding of charge carrier transport and recombination in different nanoscale architectures would provide more insight into improved electrode designs for improving the performance of photoelectrochemical cells.

- The use of nanowires for achieving improved charge carrier collection by lowering recombination losses eliminates the use of expensive single crystal substrates for achieving high efficiency in photoelectrochemical cells
- All the prior studies on using nanowire architectures have been limited to the conventionally used iodide electrolyte. The results of this work would identify and address the challenges to be overcome for using alternate one electron redox electrolytes in DSCs employing nanowire architectures. The impact of this work is schematically depicted in Figure 1.6.1.

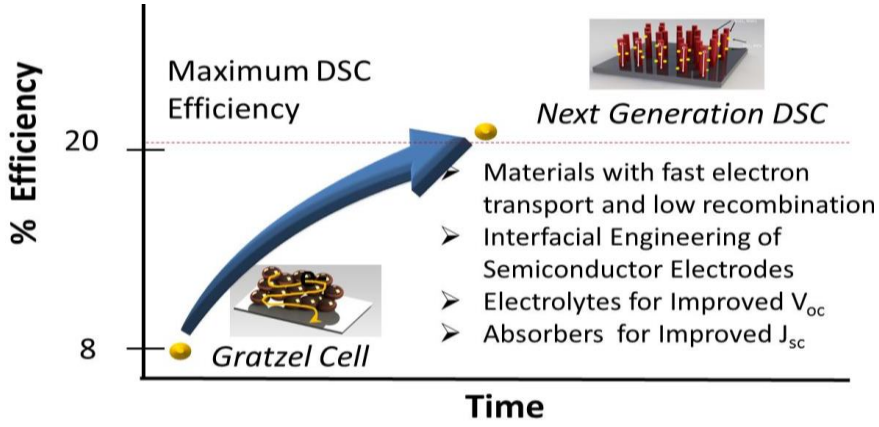

Figure 1.6.1 Impact of using nanowires based architectures for dye-sensitized solar cells

The first DSC reported an efficiency of 8 %. An increase in the efficiency is anticipated with proper engineering of the electrode materials.

- Moisture resistant protective coating developed for methyl ammonium lead iodide perovskites used in this work can be extended to other lead-free metal organic perovskites that are both moisture and oxygen sensitive. The composite coating developed in this work could enable the fabrication of perovskite cells under

atmospheric conditions and using scalable approaches such as roll to roll techniques.

- Nanowire based cathode materials with high surface stability resulting in enhanced capacity retention and coulombic efficiency. Figure 1.6.2 shows the impact of using NW based electrodes as cathode for Li ion batteries.

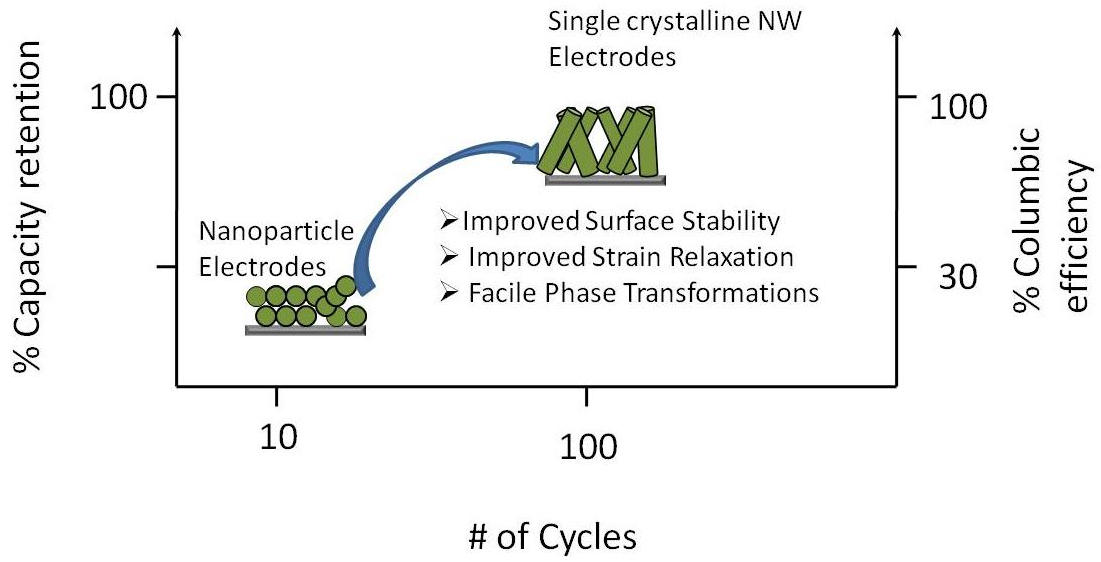

Figure 1.6.2. Impact of using single crystal nanowire cathodes for Li ion batteries

CHAPTER 2
BACKGROUND

In Chapter 2, the basic principles behind the working of photoelectrochemical solar cells and Li ion batteries are discussed. The state-of-the-art of electrode architectures used in literature are reviewed and the specific challenges with electrode architectures for photoelectrochemical cells, perovskite absorbers and lithium manganese oxide based cathodes for Li ion batteries are discussed in detail.

2.1 Basic principles of photoelectrochemical cells

Photoelectrochemical cells provide a cost-effective method for meeting the demand for carbon-neutral energy production. The main motivation for photoelectrochemical cell over solid-state p-n junction cell arose from the ease of junction formation and the low cost associated with it, especially when polycrystalline semiconductors are used. In case of p-n junctions formed with polycrystalline semiconductors, the surface of the semiconductors are doped, followed by thermal annealing to diffuse the dopants to an appropriate depth inside the semiconductor. During this process, the rapid diffusion of the dopants at grain boundaries makes it challenging to form a well-defined boundary between the p-type and n-type semiconductors and often resulting in the shunting of the cell. [7] The replacement of one of the semiconductors with a liquid electrolyte allowed the easy formation of a semiconductor–electrolyte junction for charge separation, without any expensive processing steps.

The first detailed report on the working principles of photoelectrochemical cells was put forward by Gerischer in 1975[8] and was motivated by Fujishama and Honda's report on the photocatalytic decomposition of water in 1972.[9] Gerischer explained that the photocurrents and photovoltages observed in photovoltaic cells is the result of the formation a Schottky barrier formed at the semiconductor electrolyte interface. Figure 2.1 illustrates the formation of a semiconductor-liquid junction for an n-type is immersed in redox couple with a redox potential E_{redox}. Figure 2.1a, shows the energy levels on n-type semiconductor before contact with the electrolyte. Upon immersion of the semiconductor in an electrolyte, a semiconductor–liquid junction is formed resulting in the band bending of the semiconductor at the interface and the formation of a depletion region.

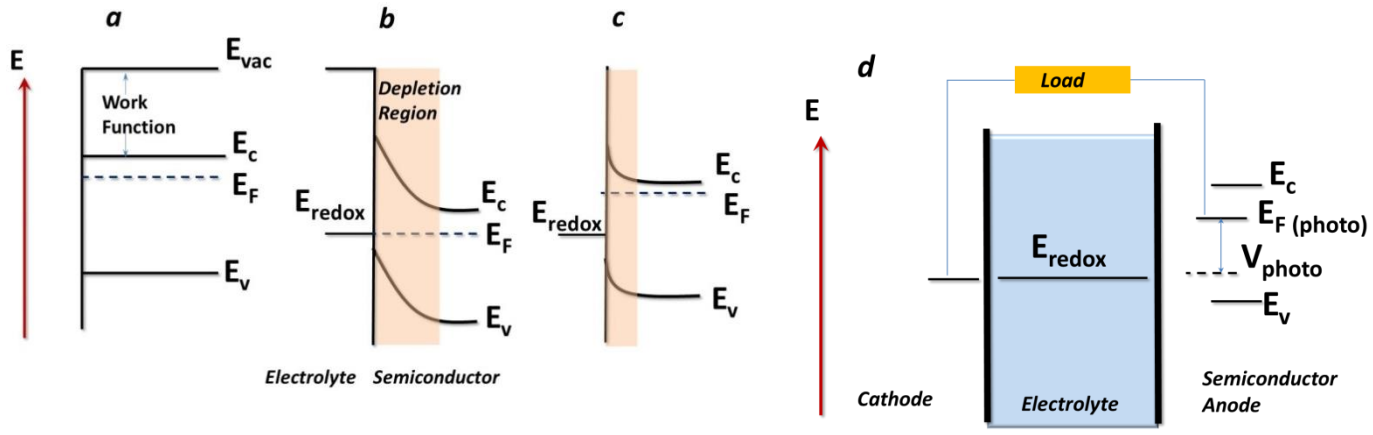

Figure 2.1.1 Energy diagram illustrating (a) energy levels in an n-type semiconductor (b) semiconductor-liquid junction in dark (c) semiconductor-liquid junction under illumination. (d) Schematic illustrating the buildup of a photovoltage in a photoelectrochemical device.

The extent of the band bending or the height of the barrier at the semiconductor – electrolyte interface is the energy difference between the Fermi level of the semiconductor

and the redox potential of the electrolyte. For simplicity, it is assumed that the surface states do not play in significant role in determining the extent of band bending. However, in reality, the trapping of electrons and holes in surface states occurs and can have an effect of extent of band bending. When the semiconductor-liquid junction is in the dark (Figure 2.1.1 b), the Fermi-level of the semiconductor and the redox potential of the electrolyte are in equilibrium. Under illumination (Figure 2.1.1 c), the excitation of electrons into the conduction band of the semiconductor leads to the formation of electron-hole pairs in the semiconductor, further resulting in the reduction of band bending. The formation of a Schottky barrier at the semiconductor-electrolyte interface causes the majority charge carrier move into the bulk of the semiconductor while the minority charge carriers move to the surface of the semiconductor and are subsequently transferred to the electrolyte. When the semiconductor is connected to a counter electrode, an open circuit voltage is established between the two electrodes. The open-circuit voltage is defined as the difference between the Fermi-level of the semiconductor and the redox potential of the electrolyte (Figure 2.1.1 d). Taking into account the different energy losses that occur in the photoelectrochemical device, an energy balance can be written as follows.[10]

$$hv = E_c - E_v = (E_{redox} - E_v) + (E_{F,vacuum} - E_{F,photo}) + (E_c - E_F) + iR + \eta_c + \eta_p + V$$

where *iR* are resistance loses in the system, η_c and η_p are the overpotentials at the counter electrode and photoelectrode.

The criteria that need to be satisfied for an efficient photoelectrochemical cell have been summarized by some earlier reports: The energy difference between the valence band

of the semiconductor the redox potential of the electrolyte, $(E_{redox} - E_v)$ has to be chosen to be equal or greater than the reorganization energy, λ. The difference $(E_{F,vacuum} - E_{F,photo})$ has to have a non-zero value for charge separation to occur. Basing on typical values for these energy differences, and overpotential losses, it was estimated that difference between the obtained photopotential and band gap of the semiconductor could be at least 1 eV. Majority of this difference in energy comes from the fact that high overpotential associated with the photoelectrode (η_p), necessary to ensure a slow back reaction and sluggish charge transfer kinetics. Further, the semiconductor should have a band gap of 1.3 $\pm$ 0.3 eV where a vast majority of the solar radiation is concentrated. Below, a band gap of 1 eV, the photocurrents increase due to increased spectral irradiance but the photovoltage drops. Above a band gap of 1.6 eV, photocurrents drop due to reduced spectral irradiance in the solar spectrum. In general, a direct correlation has been found between the stability of semiconductor and the band gap. The higher the band gap, the higher the stability and vice versa.

2.1.2 Photoelectrochemical solar cells employing single crystals: The earliest reports on photoelectrochemical solar cells comprised of single crystal immersed in a non-aqueous electrolyte along with a catalytic counter electrode such as Pt to complete the circuit. A redox electrolyte shuttles the charge between the two electrodes. A schematic of the cell setup is shown in Figure 2.1.2.

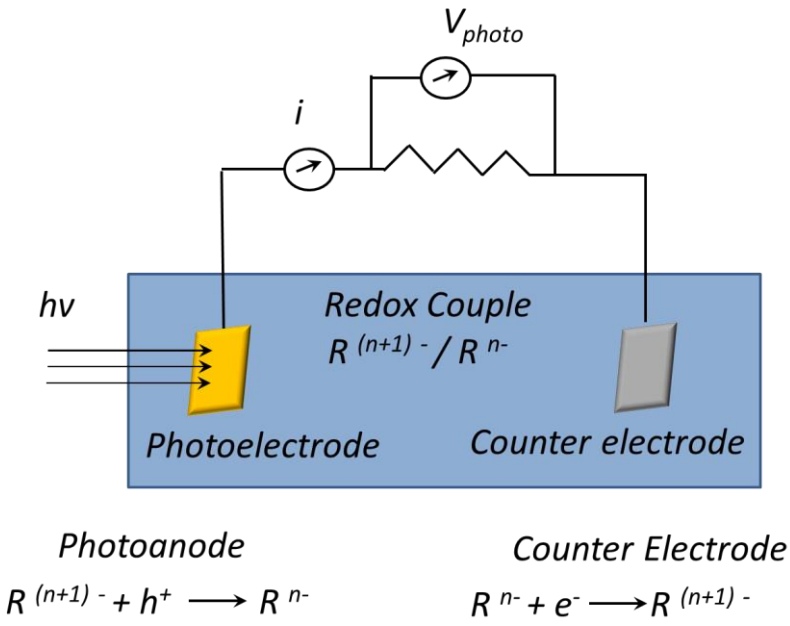

Figure 2.1.2 Schematic depicting photoelectrochemical solar cells employing single crystals.

Although power efficiencies a high as 14 % were attained with these cells, the high cost associated with single crystal substrates and their poor stability in aqueous electrolytes limited their practical applications.[11]

2.1.3 Dye-sensitized solar cells: The first successful attempt to use a polycrystalline semiconductor in a liquid-junction solar cell was put forth by Michael Gratzel in 1991.The working principle and key components of a DSC can be summarized as follows. A monolayer of dye adsorbed on mesoporous semiconducting film forms the photoanode. Absorption of incident light by the dye results in electron injection into the mesoporous semiconductor. The redox electrolyte plays has a dual role in a DSC. It regenerates the oxidized form of the dye and shuttles electrons back and forth between photoanode and the platinum counter electrode. Figure 2.1.3 shows a schematic of the working principle of a

DSC. The electron recombination is a major energy loss mechanism in the dye-sensitized solar cell (DSC). The two major recombination pathways of the photoinjected electrons in the TiO_2 are (i) reduction of the oxidized dye, $e\text{-}(TiO_2) + D^+ \rightarrow D$ and (ii) reduction of the oxidized electrolyte species, $e\text{-}(TiO_2) + O \rightarrow R$, where O stands for the oxidized species and R stands for the reduced species. The conventional Gratzel cell uses an iodide/triiodide redox couple which has very slow kinetics of recombination electrons on the TiO_2 surface with the oxidized species in the electrolyte.

The following are the challenges associated with the use of iodide redox electrolyte in DSCs: (a) severe corrosion of the metal current collectors, (b) low redox potential limits the maximum open circuit voltage than can be achieved, toxic nature, (c) the triiodide competes with light for dye absorption in the visible region, (d) huge barrier for dye regeneration (~ 0.5 eV) resulting in a loss of potential.

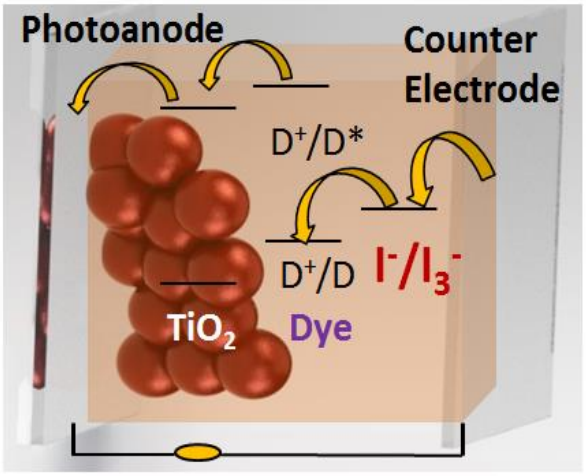

Figure 2.1.3. Schematic depicting different electron transfer process in a dye-sensitized solar cell.

2.2 Challenges associated in electrodes architectures in DSCs using alternate redox couples

The following are the challenges associated with the use of iodide redox electrolyte in DSCs: (a) severe corrosion of the metal current collectors, (b) low redox potential limits the maximum open circuit voltage than can be achieved, toxic nature, (c) the triiodide competes with light for dye absorption in the visible region, (d) huge barrier for dye regeneration (~ 0.5 eV) resulting in a loss of potential.

Several attempts have been made to replace the corrosive iodide redox shuttle with alternate redox electrolytes. Attempts to use many Ni, Cu and Fe based alternate redox couples with conventional Ru based dyes have resulted in low efficiency as shown in Figure 2.2. An organic disulfide redox electrolyte resulted in an efficiency of 6.2 %[12] and cobalt based electrolytes have resulted in efficiencies around 10%[13] and 12%[14] in DSC sensitized with alternate organic dyes. However, these redox electrolytes are not commercially available. One electron redox are commercial available on a large scale and hence can be easily integrated into DSCs if the recombination losses are lowered. The significant developments with various redox couples used for dye-sensitized solar cells are graphically reviewed here in Figure 2.2. Figure 2.2a depicts the power conversion efficiency as a function of short-circuit current density for the newly engineered organic dyes [15-22] and Figure 2.2 b shows the same for the conventional ruthenium based dyes (N-719, N3, Z-907) respectively.[15, 20, 21, 23-27] From Figure 2.2, two major reasons can be identified for the low performance of alternate redox electrolytes. First, alternate redox electrolytes using N-719 dye yield poor performance due to the poor matching of the HOMO energy level of the dye with the redox potential of the electrolyte leading to an

insufficient driving force for dye regeneration. The slow regeneration kinetics of the dye increases the recombination of the electrons in the semiconductor with the oxidized state of the dye, lowering the efficiency. Second, the electrode characteristics such as fast electron transport, slow recombination kinetics, good dye adsorption, low over potential and fast electron transfer kinetics at the counter electrode were not necessarily engineered for these alternate redox electrolytes to achieve high short-circuit current densities. The high efficiencies observed with the iodide electrolyte and the N-719 dye are due to an optimized energetic alignment between the redox potentials of the electrolyte with the dye. Further, the slow recombination kinetics allows for high collection efficiencies even with nanoparticle based electrodes.

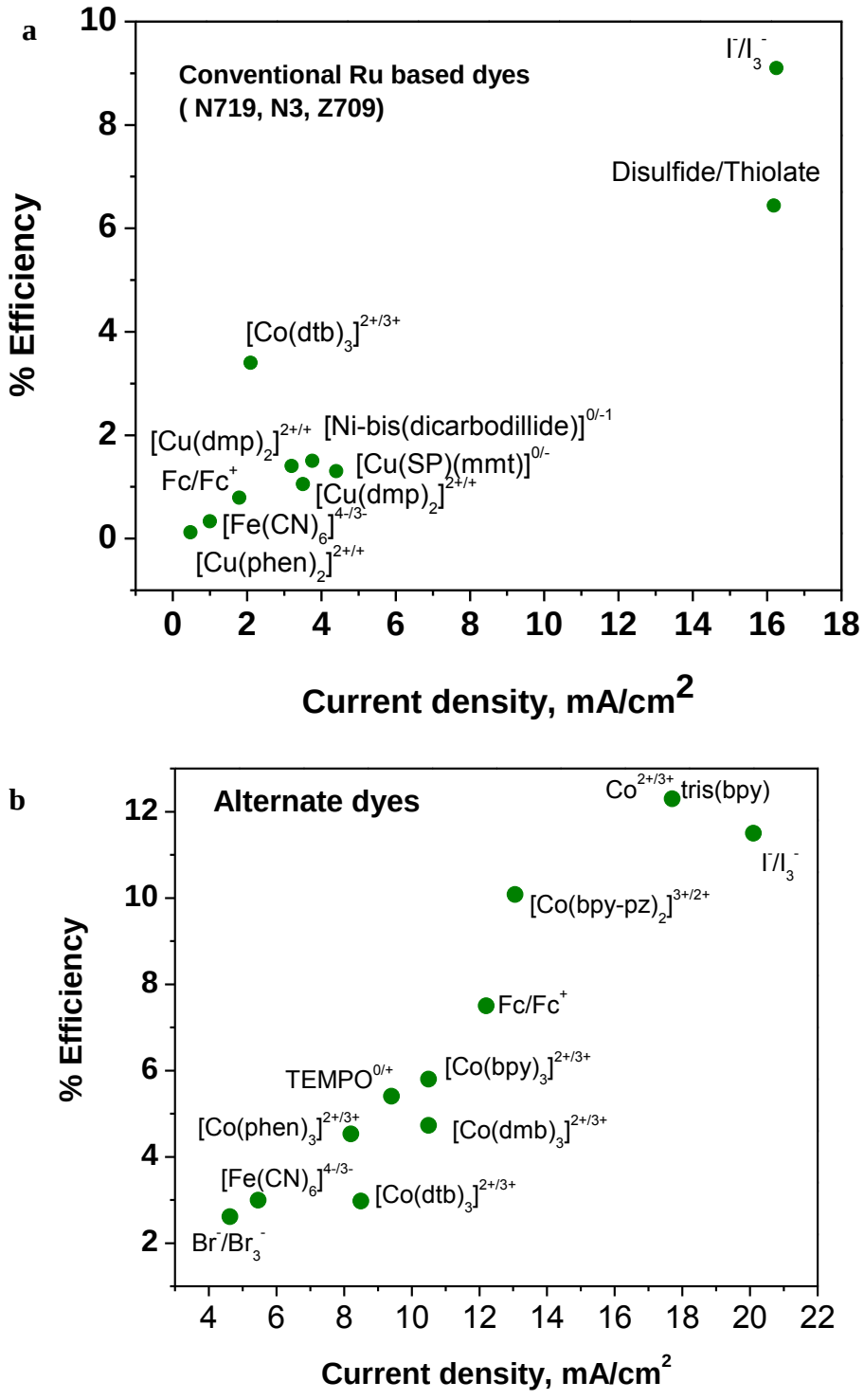

Figure 2.2. State of the art of different redox electrolytes (from References 2-12) used for dye-sensitized solar cells for the conventional Ru based dyes (a) and (b) alternative dyes

In general, the attempts to lower recombination losses in DSC using one electron redox couples can be classified into the following –

2.3 Literature attempts to address challenges with one electron electrolytes in DSCs

2.3.1 Conformal coatings of insulating layers*:* Attempts to lower recombination from TiO_2 to iodine in the redox electrolyte involved the use of pyridine derivatives.[28] It was found that the recombination via trapped electrons is the major route of electron back transfer from TiO_2 surface to the oxidized form of the electrolyte.[29, 30] Gregg and co-workers made the first attempt to use kinetically fast alternate redox electrolytes in DSC by passivating the TiO_2 surface and the tin oxide conductive substrate using films of insulating polymers and silanization treatments respectively. Recombination of electrons occurred from two major sites - (i) electrons from the conducting substrate and (ii) potential dependent fraction of electrons from semiconducting particles. These two parasitic interfacial reactions were found to annihilate all the photogenerated electrons when kinetically fast redox electrolytes are used. Control of the silanization reaction to obtain a uniform coating over the nanoparticles was a major challenge. Further, the amount of adsorbed water on TiO_2 nanoparticles was found to a lot of variability leading to poorly reproducible results. Thickness of the insulating coating is another important aspect as this could displace the dye or result in the degradation of the dye, the electrolyte would be isolated from the dye thus rendering the regeneration impossible. Wide band gap materials such as Nb_2O_5, SiO_2, ZrO_2 and Al_2O_3 have investigated as barrier layer coating in DSC. The coating is usually formed by a dip coating process. The formation of pinhole free films with precise control of thickness is difficult to achieve using dip coating methods. Hupp and co-workers used atomic layer deposition to create conformal coatings of Al_2O_3 on TiO_2

and SnO_2 nanoparticles. Atomic layer deposition of Al_2O_3gives an angstrom level control of thickness.[31, 32] The distance between the oxidized electrolyte species and the surface of TiO_2 plays an important role in determining the performance. The electrons at surface need to be shielded against recombination and the dye needs to efficiently regenerate without altering the injection kinetics.

2.3.2 ***1-D nanostructures:*** One dimensional nanostructures such as nanowires exhibit fast electron transport and suppressed electron recombination due to their single crystalline nature and low number of surface trap states. Prior work from our group has shown that tin oxide nanowires exhibit two orders of magnitude higher electron lifetimes when compared with tin oxide or titania nanoparticles when iodide redox electrolyte was used.[33, 34]Aydil and co-workers found that single crystalline nature of rutile nanowires does not ensure fast charge transport but ensures suppressed recombination in case of rutile TiO_2 nanowires.[35] These results indicate that transport rate in nanowires can be limited by the number of surface trap states. Differences between the distributions of surface trap states are believed to account for the observed differences

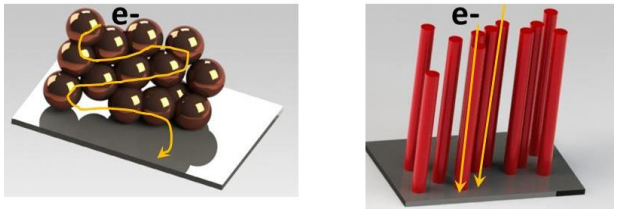

Figure 2.3.1. Schematic illustrating fast electron transport in nanowires electrodes

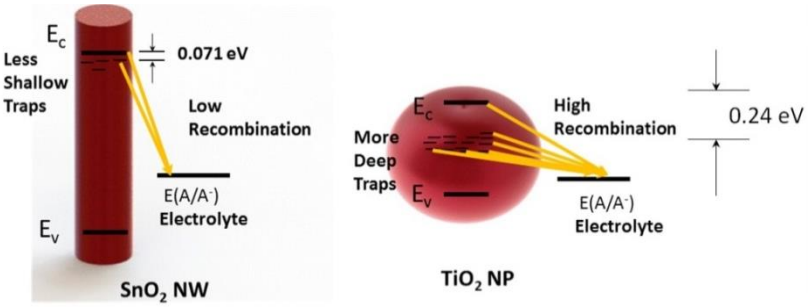

Figure 2.3.2. Schematic illustrating electron recombination from trap states in SnO_2 NWs and TiO_2 NPs.

between nanowires and nanoparticles. Similar observations were made by Frank et al. who synthesized vertically oriented polycrystalline anatase nanotubes on Ti foils.[36] Approaches looking at passivating traps states are critical for using nanowire based photoanodes with alternate redox electrolytes in DSCs. In spite of nanowires demonstrating interesting electron transport and recombination properties, all of the studies to date have employed iodide redox electrolyte in conjunction with nanowires. A fundamental understanding of the challenges that need be overcome for using nanowires in DSCs with alternate redox electrolytes is required. The current density and hence the efficiencies of nanowire based DSC is primarily limited by their surface area.

2.3.3 Engineering dye molecules: Controlling the film thickness of photoanode film offers an interesting way to control the number surface recombination centers in the photoanode film. Lowering the film thickness from 10 microns in a conventional DSC to 2-6 microns leads to a substantial lowering of recombination losses. When these relatively thin films are sensitized with a dye of high extinction coefficient a considerable enhancement in the performance of the DSC employing alternate redox couple can be achieved. Using this approach, Gratzel and co-workers employed an organic redox shuttle, 2,2,6,6-tetramethyl-1-piperidinyloxy (TEMPO), in D-419 sensitized DSCs to achieve a power conversion efficiency of 5.4%.[37] Similarly, Daeneke et al. used a high extinction coefficient metal free organic dye (Carbz-PAHTDT) on a 6 micron TiO_2 film to lower recombination losses with ferrocene redox electrolyte.[15] Due to lowering of the regeneration barrier, a 100 mV improvement of the open circuit potential was achieved when compared with the N-719/iodide electrolyte system and efficiency of 7.2 %. Also, ferricynaide-ferrocyanide water based one-electron redox electrolyte used in conjunction with a 5 micron thick TiO_2

film sensitized with a highly absorbing hydrophobic dye has shown a power conversion efficiency of 4.2 %.[21]

2.4 Perovskites as Alternate Absorbers for Solar Cells

Metal-organic perovskites were originally developed by David Mitzi for application towards solution processed metal-organic transistors because of their unique optical and electrical properties. [38] The mobility in organic material is poor due to weak Vanderwaal interactions between the molecules when compared to inorganic materials where ionic forces and covalent bonds are more predominant. The metal organic perovskites can be thought of as hybrid between organic and inorganic materials combining the solution processability of organic materials with the high mobilities found in inorganic materials. Mitzi was the first to describe the structure of layered perovskites. A two-dimensional representation of the arrangement of the organic and inorganic layers in the perovskite is shown in Figure 2.4.1

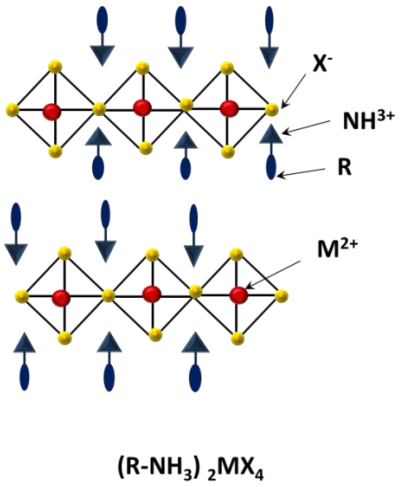

Figure 2.4.1 Two dimensional representation of the layered $(R\text{-}NH_3)_2\ MX_4$ perovskite.

In the inorganic layer, the halide ions are arranged at the corners of octahedra, with the metal atoms in the center of the octahedra to balance the charge. The inorganic layers have the molecular formula of the type ABX_3 and are called as perovskite layers. The optical and electronic properties of the perovskite can be tuned by varying the organic ligands (R) or the metal halides making them very promising solar absorber materials.

There has been a revived interest in these materials as alternate absorber materials in dye sensitized solar cells after Miyasaka's report. [39] The slow dissolution of perovksites in liquid electrolytes has been identified as one of the factors limiting the performance [40] and subsequent reports have focused using solid state hole transport materials instead of liquid electrolytes.[41, 42] Improvements of perovskite solar cell efficiencies over the past few years have been achieved using different anode architectures,[43-45] deposition methods,[46-50] varying the halides and organic cations in the perovskite structure,[39, 51, 52] and by the application of materials with improved electron and hole transport characteristics.[53, 54]

The deterioration of the perovskite when exposed to moisture still remains a major roadblock limiting the progress and commercialization of perovskite solar cells. Walsh and co-workers proposed an acid-base mechanism for explaining the degradation of the perovskite.[55] The reaction of perovskite and water is considered as a Lewis acid-Lewis base reaction respectively. The degradation mechanism is depicted in schematic 2.4.2, according which hydroiodic acid, lead(II) iodide, methyl amine. Further experiments are still required to confirm the degradation mechanism.

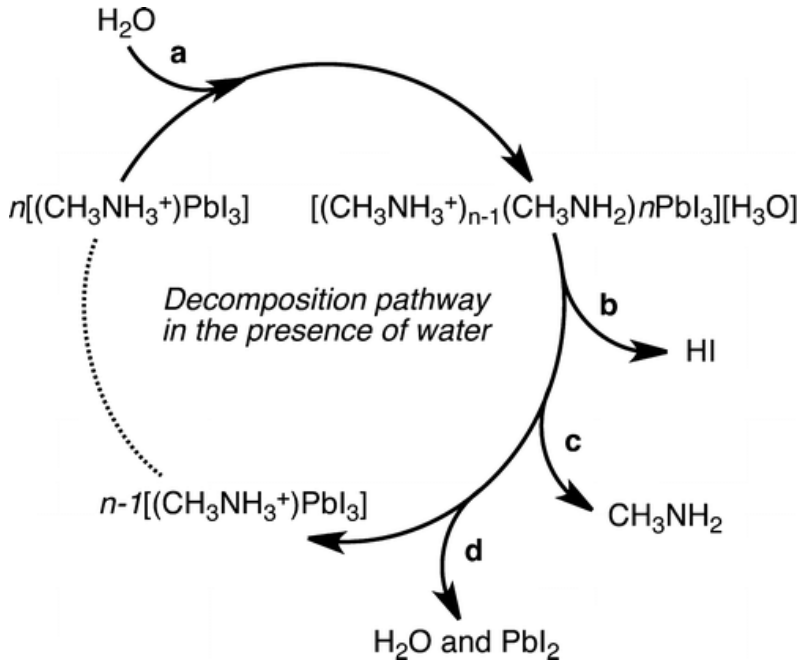

Figure 2.4.2 .Proposed pathways for degradation of methyl ammonium lead iodide perovskites in the presence of water. (Reproduced with permission from Ref [55])

Grätzel *et al*. noted that the perovskite cell fabrication needs to be performed under controlled atmospheric conditions with a relative humidity of <1% for achieving consistent results.[56]

2.4.1 Attempts to improve moisture stability of perovskites: Attempts to improve the moisture stability of perovskites cell have investigated using hydrophobic hole transport materials,[57] fabricating layered perovskites, and using alumina coatings on the surface of the perovskite.[58, 59] However, none of these strategies prevent the complete penetration of moisture through films and ultimately result in perovskite deterioration and eventually result in degradation of the perovskite. Further, the stability of these coatings has only been evaluated in low to moderate humidity (20-60 % relative humidity). The use

of insulating Al_2O_3 as protective coating puts a stringent limitation on using extremely thin layers, which are not completely impermeable to moisture. After 18 h of testing at 60 % relative humidity, Niu *et al.* observed that the power conversion efficiency of Al_2O_3 dip-coated perovskite solar cells dropped by half from 4.6% to 2.1%.[58]

In the reminder of this chapter, the challenges and issues with transition metal oxide materials specifically, on manganese oxide based materials are highlighted.

2.5 Li ion Batteries.

Among the different battery technologies, Li ion technology have gained wide spread importance as portable rechargeable batteries for a range of applications of their high specific energy density (100-200 W.h/Kg) and high volumetric energy density (200-400 W.h/L) that directly translate into small size and lighter weight batteries.[60]

Working principle of a Li ion battery: A Li ion battery consists of a cathode and anode separated by an electrolyte permeable separator. The space between the electrodes is filled with a non-aqueous electrolyte. In Li ion battery literature, Li ion insertion into the lattice is referred to as intercalation, while Li ion removal is termed as deintercalation. During the charge cycle, Li ions are deintercalated from the cathode, diffuse through the electrolyte and intercalate into the anode. Electrons move in the external circuit from the cathode to the anode. During the discharge cycle, the process is reversed. A schematic shown in Figure 2.5.1 illustrate these processes, i.e., Li ion deintercalate from the anode, diffuse and intercalate at the cathode while the electrons move from the anode to the cathode.

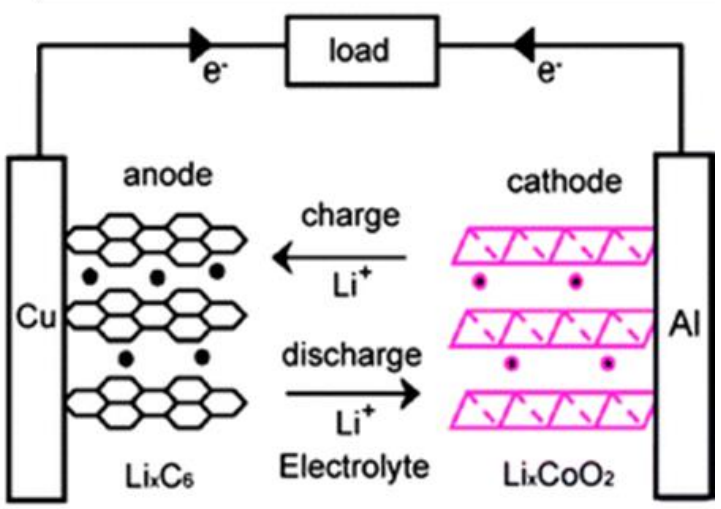

Figure 2.5.1 Schematic illustrating the working principle of a Li ion battery

The following is a glossary of some typical terminology used with Li ion batteries

- *Coulumbic Efficiency*: The coulombic efficiency of a Li ion battery is defined as follows-
    - $\%\ Coulombic\ Efficiency = \frac{Discharge\ Capacity}{Charge\ Capacity} * 100$

  The coulombic efficiency gives an indication of the current (or charge) wasted in undesirable side reactions such as electrolyte decompositions and phase transformation or corrosion of electrode materials of the battery.
- *C-rate*: The C-rate is a convenient way of expressing the charge or discharge current rate of a battery. For example discharge rates of 1C would imply that current corresponding to this discharge rate would cause the battery to be discharged in one hour.

- *Specific Capacity*: The specific capacity of a Li ion battery is defined as the amount of charge that a Li ion battery contains per unit weight of the active electrode material. It is expressed in mAh/g and depends on the current rate.
- *Solid-Electrolyte Interface:* A passivating layer formed on the electrodes due to the electrode-electrolyte reactions. The layer is ionically conducting and electronically insulating and adds to mechanical stability of the electrodes.

In the next few sections, the specific challenges associated with electrode architectures for dye-sensitized solar cells, perovskite solar cells and for lithium manganese oxide cathodes in Li ion batteries are detailed.

2.6 Challenges with lithium manganese oxide based cathodes for Li ion batteries

Oxides of transition metal oxides have been widely investigated as cathode materials for Li ion batteries. Typically, the lithium intercalation/deintercalation in these materials is associated with a change in the oxidation state of the transition metal cation in order to maintain charge neutrality. Changes in the composition of cathode material during Li insertion and removal results in phases changes in the material and hence maintaining structural stability during is the biggest challenge in transition metal oxide based cathode materials.[61] Specifically, there has been tremendous interest in developing manganese oxide based cathodes with high capacity retention because of their low cost, low toxicity and high thermal stability. In particular $LiMn_2O_4$ and Li_2MnO_3 have been widely investigated as cathode materials for Li ion batteries due their potential for achieving high voltage and high capacity as shown in Figure 2.6.1.

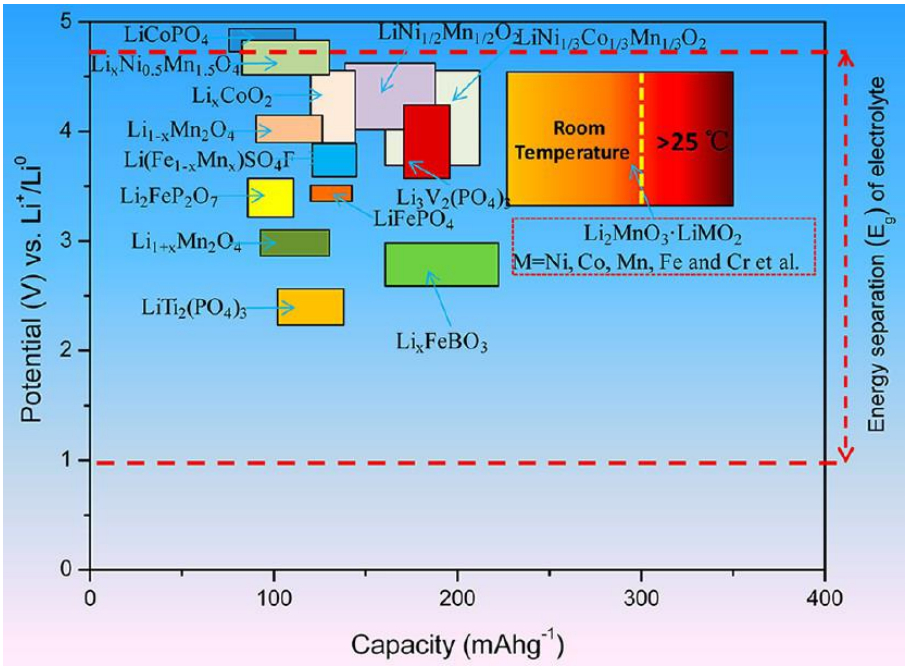

Figure 2.6.1. Comparison of operating voltage and capacity of different transition metal oxides used as cathode for Li ion batteries. (Reproduced with permission from Reference [62].)

The interesting properties of these materials along with their, technical issues and attempts to address them are summarized as follows-

2.6.1 $LiMn_2O_4$ based electrodes

$LiMn_2O_4$ has a spinel crystal structure as illustrated in Figure 2.6.2 The Mn_2O_4 spinel framework provides three dimensional channels for the fast charge transport of Li ions. The average of oxidation state of Mn is in $LiMn_2O_4$ is +3.5, i.e., a stoichiometric amount of Mn^{+3} and Mn^{+4} cations are located in the octahedral 16d sites of the lattice.[63] The capacity fade during cycling of $LiMn_2O_4$ has been observed due to the following reasons: (i) Mn dissolution by the following disproportionation reaction[64] $2\,Mn^{3+} \rightarrow Mn^{2+} + Mn^{4+}$, due the formation HF in $LiPF_6$ based electrolytes (ii) irreversible phase

transformation from $LiMn_2O_4$ to $Li_2Mn_2O_4$ due to Jahn-Teller distortion effect, introducing significant strain on the lattice.[65]

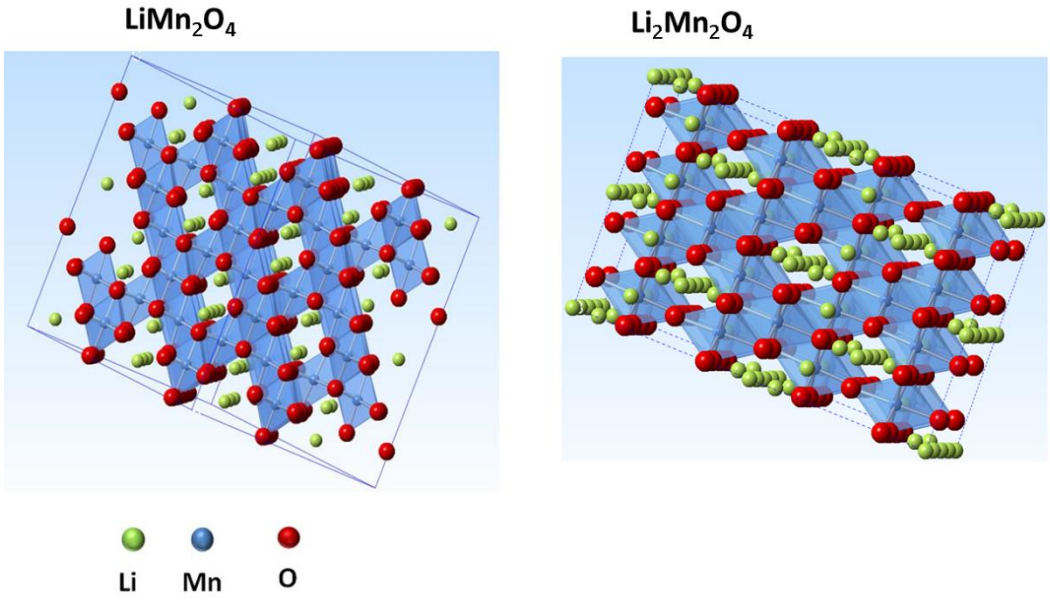

Figure 2.6.2. Crystal structure of cubic $LiMn_2O_4$ and tetragonal $Li_2Mn_2O_4$ drawn using Crystal Maker™ software.

The reaction for Mn dissolution in $LiMn_2O_4$ proposed by Aurbach and Wang *et al.*[66, 67] is written as follows:

$$LiPF_6 \rightarrow LiF + PF_5$$

$$PF_5 + H_2O \rightarrow 2HF + PF_3O$$

HF has been proposed to dissolve Mn according to the Hunter's mechanism [68]

$$LiMn_2O_4 + 4H^+ \rightarrow 3MnO_2 + Mn^{2+} + 2Li^+ + 2H_2O$$

As mentioned earlier, the other significant issue with $LiMn_2O_4$ based electrodes is due to capacity fade associated with Jahn-Teller effect. The Jahn-Teller effect states that no non-linear molecule (atoms in the molecule are not arranged in a straight line) is stable in a degenerate electronic state and it distorts to a lower symmetry configuration that is less energetic to break the degeneracy.[69] When significant amounts of Li ions are inserted into the $LiMn_2O_4$ lattice during deep discharge (voltage < 3.5 V vs. Li/Li^+), the cubic $LiMn_2O_4$ where Li ions occupy the tetrahedral sites undergoes a phase transition to tetragonal $Li_2Mn_2O_4$ where Li ions occupy the octahedral sites of the lattice. The Mn^{3+} ions in high spin states present in the lattice have been shown to be responsible for the Jahn-Teller distortion due to their electronic configuration.[70] This crystallographic distortion with a 16 % change in the (c/a) ratio sets up significant strain in the lattice resulting in poor structural stability of the material leading to severe capacity fading during cycling.[71]

2.6.2 Li_2MnO_3 based electrodes

Li_2MnO_3 has a layered structure as shown in Figure 2.6.3. The oxidation state of Mn in Li_2MnO_3 is +4 and hence it was initially thought that this particular material is electrochemically inactive as Mn cannot be further oxidized to a higher oxidation state than +4 in an octahedral environment. [72] However, subsequent investigations have shown that the charge process (or delithiation) in these electrodes can by electrochemical activation by charging upto 4.5 V [73], and by simultaneous removal of Li and O[74], presence of oxygen vacancies in the as-synthesized material [75] and by ion exchange of Li^+ with H^+ from the electrolyte [76].The initial delithiation in Li_2MnO_3 occurs by a small loss of oxygen anions from the lattice to balance the charge associated with Li^+ extraction. Further Li extraction occurs by ion exchange of Li^+ with H^+.

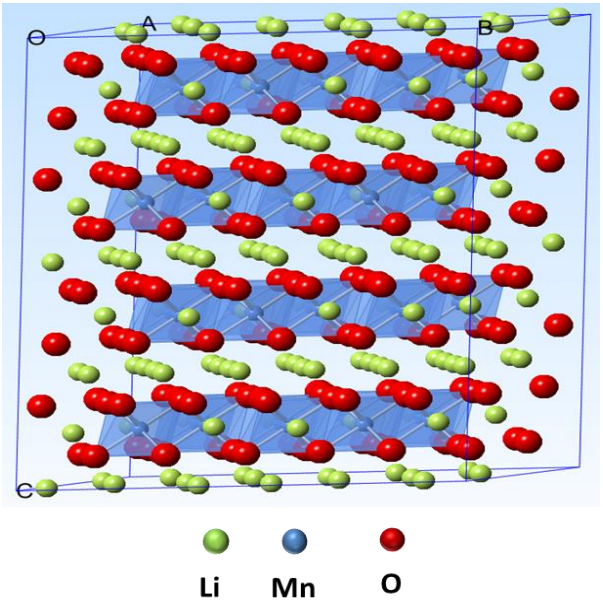

Figure 2.6.3. Crystal structure of layered Li_2MnO_3drawn using Crystal Maker^{TM} software.

The technical issues facing Li_2MnO_3 are: (i) poor columbic efficiencies associated with oxygen evolution and phase transformations in the lattice[77], (ii) poor surface stability due to repeated shearing of oxygen atoms during cycling and subsequent loss in capacity[78], (iii) low Li ion diffusion coefficients and (iv) lack of proper understanding of the reaction mechanism of charging and discharging of Li_2MnO_3.[62]

2.7 Literature attempts to address challenges with lithium manganese oxide cathodes

Attempts to address technical issues with lithium manganese oxide based electrodes can be classified as follows:

2.7.1 Nanowire based architectures. Single crystalline nanowires of the lithium manganese oxide can offer superior advantages in terms of stress relaxation and prevent the capacity associated with the capacity fading associated with the phase transformation. In the case of $LiMn_2O_4$, the capacity fade associated with the Jahn-Teller distortion effect can reduced by using single crystal nanowires that allow for facile stress relaxation.[79] In addition, nanowire based electrodes also exhibit faster kinetics of Li ion intercalation and deintercalation due to short diffusion lengths for Li ions in the radial direction of the nanowires and also due to their single crystallinity.[80]

2.7.2 Element doping. Several approaches have looked at doping cations of Ni [81], Cr[82], Fe[83], Ga[63], Mg[84], Al[85] to reduce Jahn-Teller distortion effect in $LiMn_2O_4$. These approaches inhibit the Jahn-Teller distortion by reducing the number of Mn^{+3}cations that induce the distortion. In the case of Li_2MnO_3, most of these would be ineffective as they cannot get oxidized further below 5 V vs. Li/Li^+, and this is would result in oxygen evolution from the lattice to maintain charge neutrality during lithium deintercalation. Although Cr and Ru have been found to be effective in improving the Li ion diffusion coefficient in Li_2MnO_3, the toxicity of Cr and high cost Ru limit the commercial viability of these Li_2MnO_3 doped with these cations.[86, 87] From theoretical calculations, doping Li_2MnO_3 with Mo has been found to more advantageous as Mo can oxidized from +4 to +6 oxidation state thereby reducing oxygen loss from the Li_2MnO_3. Further, Mo doping can also improve the conductivity by reducing the band gap and reducing Li deintercalation potential.[88]

2.7.3 Surface coating. Metal oxides such as Al_2O_3, ZnO, ZrO_2, MgO, Cr_2O_3,TiO_2, SiO_2 and metal phosphates $AlPO_4$, $FePO_4$, YPO_4, $LaPO_4$ such as have been investigated as protective coatings as $LiMn_2O_4$.[89] The protective effect is hypothesized due to coating as physical barrier for Mn dissolution from HF attack[90], retention of oxide vacancies in the lattice[91], suppression of electrolyte decomposition[92]. However, more detailed studies are required to probe the reasons for protective effect of these coatings. In case of layered Li_2MnO_3 based materials the protective coatings such as AlF_3[93] have been reported to form spinel phases on the shell but the mechanism of formation of these shells and their conformality and thickness has not been investigated. More recent reports on surface modification of Li_2MnO_3 based materials have involved the forming conformal shells of $Li_{1+x}Mn_2O_4$ spinel phases which enhance capacity retention by acting as a barrier for erosion of the layered material into the electrolyte while still permitting fast ion transport through the 3D Li ion transport channels in the spinel.[94],[95]

2.7.4 Electrolyte development. Efforts on electrolyte development have focused on additives that can inhibit the formation of HF and PF_5 which result in degradation of lithium manganese oxide based cathodes. For example, the addition of $LiPF_6$ salt stabilizers such as tris (2, 2, 2-trifluoroethyl) phosphite (TTFP), 1-methyl-2-pyrrolidinone (NMP).[96, 97] These stabilizers can acts as Lewis bases and form complexes with PF_5 which otherwise is known to attack and destabilize the protective solid electrolyte interface (SEI).Similarly additives such as heptamethyl-disilazane (HEMDS) can scavenge the HF and H_2O by reacting with them to form stable products as shown in the reaction scheme below and thereby reduce the Mn dissolution.[98]

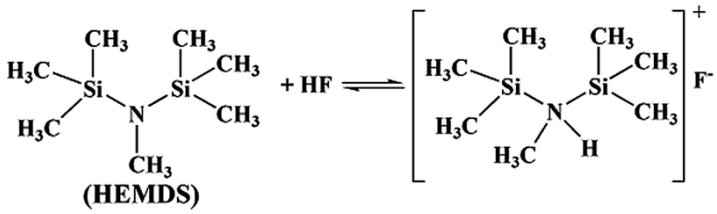

Figure 2.7 Reaction showing HF scavenging using HEDMS electrolyte additive.

CHAPTER 3

EXPERIMENTAL METHODS AND CHARACTERIZATION TECHNIQUES

This chapter discusses the experimental procedures used for synthesizing the electrode materials. The fabrication procedure for dye-sensitized solar cells, perovskite solar cells and Li ion batteries coin cells are also described. The structural characterization techniques for the electrode materials and the electrochemical characterization techniques used to characterize these devices are also summarized.

3.1 Synthesis of Tin Oxide Nanowires by Reactive Vapor Transport

The synthesis of tin oxide nanowires on quartz substrates is carried out using a low pressure CVD reactor, which is equipped with a basket shaped resistive heater. A schematic of the reactor is shown in Figure 3.1. Pellets of tin metal powder are loaded in the alumina coated tungsten basket screwed onto copper feedthroughs connected to a voltage transformer. The inert alumina coating improves heat transfer and prevents the molten tin from wetting the alumina, and results in a point contact, thereby ensuring no resistant change in the basket heater when the tin melts. The reactor is equipped with a quartz window the permits the measurement of heater temperature using a dual wavelength pyrometer A quartz substrate is placed on the heater with a small clearance at the sides to allow the gases to flow into the basket heater.. The reactor is purged 3-4 four times with Ar gas and is pumped down to a pressure of 700 m torr, monitored using a capacitance manometer. Oxygen and hydrogen are admitted into the reactor at flow rates of 5 sccm and 20 sccm respectively. The heater temperature is ramped up to 1100 ℃ by increase the voltage on the transformer in steps of 5 V until 20 V is reached and 2.5 V steps until 22.5

V is reached. After 20 minutes, the reactor is cooled using the same voltage steps. The vent valve of the reactor is opened and the tin oxide coated quartz substrates are removed from the reactor for further characterization and processing.

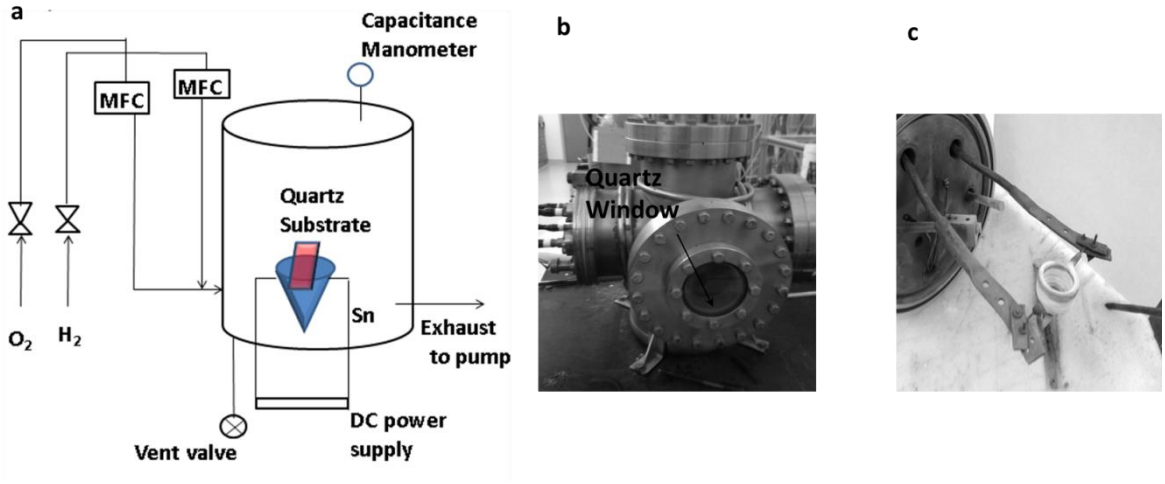

Figure 3.1(a) Schematic of the low pressure CVD reactor using for synthesizing tin oxide NWs (b) picture of the reactor showing the quartz window for temperature measurement (c) alumina coated tungsten basket connected to copper feedthroughs.

3.2 Solvo-plasma technique for Synthesizing Metal Oxide Nanowires

Atmospheric Microwave Plasma Reactor: An upstream microwave plasma reactor is employed for synthesizing metal oxide nanowires by solvo-plasma technique. Details of the reactor design have been described in prior publications from our group (Refs).[99-102] In brief, the reactor comprises of a magnetron that generates microwaves of 2.45GHz frequency also called as the S-band. The microwaves from the magnetron are transmitted by a rectangular waveguide (WR-284) which allows the propagation of microwaves in the TE_{10} mode.

The custom built microwave plasma reactor (Figure 3.2) is equipped with a power detector which measures the forward and reflected power, a circulator connected to a water cooled dummy load and an impedance matching system. The circulator only allows the propagation in one direction and is used to prevent the reflected microwaves from entering the magnetron.[103] The impedance matching system comprises of a circuit of capacitors and resistors matches the impedance of the source (magnetron) and the load (plasma) for maximum power transmission and to reduce the reflected power to zero. Reflected power leads to the buildup of standing waves in waveguide which lead to deterioration of electrical components of the reactor. The electric field is maximum at a distance of $\lambda_g/4$ (where the wavelength of the microwaves in the waveguide $\lambda_g = \frac{\lambda}{\sqrt{1-(\frac{f}{f_c})}}$, where λ is the wavelength of microwaves generated from the magnetron = 12.24 for a 2.45 GHz magnetron and f_c is the cut frequency of the waveguide = c/2a, where c is the velocity of light in vacuum and a is the width of the rectangular waveguide)from the applicator end of the waveguide.[99]

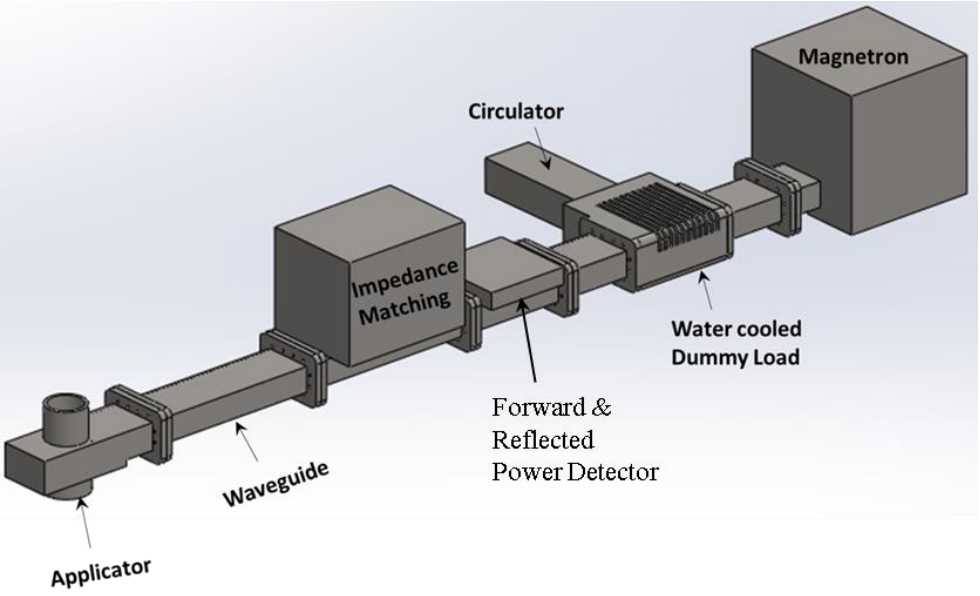

Figure 3.2. Atmospheric upstream microwave plasma reactor used for the solvo-plasma technique. (Image Courtesy: Tu Quang Nguyen)

The maximum electric field is concentrated at the center of a dielectric tube (usually made of quartz) inserted in the applicator. The resultant concentrated electric field in the middle of the quartz tube leads to the dielectric breakdown of the gases introduced into the applicator.

Gases are admitted tangentially at a 60 degree angle, to create a helical flow path that prevents the dielectric tube from melting due to heating by the plasma. A metal rod is used to ignite the plasma at the applicator. Initially, an easily ionizable gas such as Ar with low dielectric breakdown constant is introduced into the reactor and a metal rod with is used to strike the plasma. Subsequently, air is admitted to the reactor and the flow Ar is turned off.

Solvo-plasma Technique: In this technique, metal oxide nanoparticles and alkali metal salt are mixed in a fixed ratio and exposed to the atmospheric plasma flame for a short duration of time to form alkali metal oxide nanowires. The salt is removed by rinsing several times with distilled water, and the samples are immersed in 1 M HCl to exchange in alkali metal with hydrogen in the as-synthesized nanowires. The samples are annealed either in an oven for a long time (~12 h) or in the plasma flame for a short times (~ order of 2-5 minutes) to form the respective metal oxide nanowires.

3.3 Atomic Layer Deposition (ALD)

Atomic layer deposition is a vapor phase technique used to grow thin films with high conformality and uniformity. The technique involves the self-limiting surface

reactions occurring on a substrate heated to a certain temperature. The reactant gases are sequentially pulsed into the reactor chamber using solenoid valves. The individual surface reactions are called half reactions. During each of these half reaction a precursor is pulsed in a low pressure reactor for a fixed amount of time to allow the precursor to fully react at the substrate and form a monolayer. An inert gas such as nitrogen is typically used as a carrier gas to deliver the precursors to the reactor chamber. The carrier gas is typically in viscous flow and two main parameters are considered for optimizing the pressure in a viscous flow ALD reactor – (i) Gas interdiffusion and (ii) entrainment.[104] In the viscous flow regime, the diffusion coefficient is inversely proportional to pressure, i.e., D ~ 1/P, where D is interdiffusion coefficient of a precursor into the carrier gas. The resulting displacement of the gas can be calculated as $x = \sqrt{6\,D.t}$. This equation gives the time (t) required for the displacement of the stagnant precursor gas from the reactor. Secondly, the mean free path of the carrier gas should be small enough (on the order of μm) to entrain the precursor gases and deliver them to the reactor chamber. The mean free path (λ) is function of pressure according the kinetic theory of gases[105], $\lambda = \frac{kT}{\sqrt{2}\pi P.d^2}$ (where k= Boltzmann constant, T is temperature in K, P is pressure, d is the diameter of the molecule). The reactor chamber is purged before the next pulse of the reactant gas is introduced in order to remove unadsorbed surface species and reaction by-products. The introduction of the next precursor leads to a self-limited surface reaction on the heated substrate and the process is repeated to stack monolayers of the film. For self-limiting growth to occur, ALD needs to be carried in a specific temperature window. Temperatures outside the ALD temperature window result in a deviation from the self-limiting growth-

at very low temperatures due to the slow kinetics of reaction and condensation of the precursors cause this deviation while at high temperatures due to the increased rate of desorption of precursors from the surface.

For deposition of high aspect ratio structure, an exposure mode is used where the substrate is exposed the precursors after being pulsed into the reactor. This ensures sufficient time to diffuse through trenches or holes in the high aspect ratio structures.

A commercially available ALD reactor from Cambridge instruments (Savannah 200) was used for the deposition of aluminum oxide and titanium dioxide. In the case of aluminum oxide by ALD, trimethyl aluminum and water are used the precursors while for titanium dioxide deposition titanium isopropoxide and water were employed as the precursors.

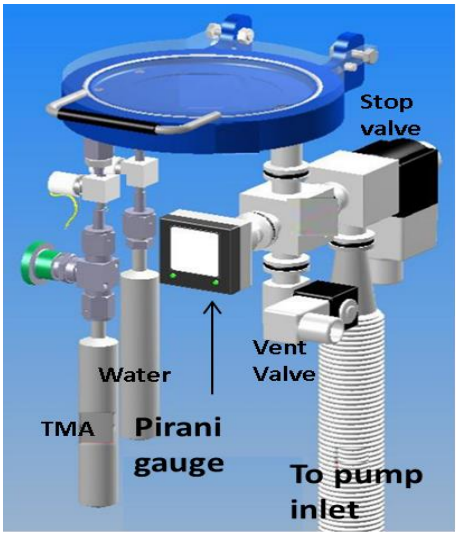

Figure 3.3 Schematic of the ALD reactor setup

One ALD reaction cycle comprises of one dose of the metal precursor followed by a few seconds of purging and one dose of water followed by a few seconds of purging. The reactor assembly comprises of a stainless steel chamber equipped with an inner disk heater

to heat the substrate. Pulses of precursors are delivered to the reactor chamber by the action of solenoid valves and using nitrogen as carrier gas. A nitrogen flow rate of 20 sccm is typically used. The solenoid valves are resistively heated to 70 ℃ to prevent precursor condensation near the valves. The pressure in the reactor chamber is monitored by using convection enhanced Pirani Gauge. The by-products from the ALD reaction chamber are exhausted into fume hood using a rotary vane pump.

3.4 Electrophoretic deposition (EPD)

Electrophoretic deposition is an electrochemical technique to coat nanoparticles uniformly on the surface of electrodes. It involves the movement of charged particles dispersed in a solvent under the presence of an applied electric field. [106] In this dissertation, EPD is used to coat nanoparticles on the surface of nanowires to form hybrid architectures. To fabricate hybrid architectures, the nanowire electrodes are immersed in colloidal solutions (2% by wt.) of the appropriate nanoparticles (tin oxide or titania), a bare FTO slide is used as a counter electrode and a potential of 5 V is applied for 15s.

3.5 Procedure for fabricating dye-sensitized solar cells

The following is the procedure for fabricating high efficiency dye-sensitized solar cells:

(i) **Cleaning glass slides:** The fluorinated tin oxide (FTO) coated glass electrodes cut to an appropriate size using a Beetle Bits glass cutting system. The slides are cleaned in a detergent solution (Mucasol) for 30 minutes and rinsed with ethanol and DI water and dried with by flowing air over them. The slides are treated with

atmospheric RF plasma (Plamax reactor) for 15 minutes. An oxygen flow rate of 8 lpm and an argon flow rate of 10 sccm and a plasma power of 250 W are used.

(ii) **$TiCl_4$ treatment**: An aqueous solution of $TiCl_4$ is prepared as follows. The concentrated solution of $TiCl_4$ and DI water are cooled in an ice bath to zero degrees Celsius. The $TiCl_4$ precursor is added drop wise to the cooled DI water until a 40 mM aqueous solution of $TiCl_4$ is obtained. The $TiCl_4$ solution is transferred to a petri dish and the cleaned FTO slides are immersed in this solution with the conductive side facing up. The petri dish is transferred to an oven at 70 ° C for 30 min. The slides are then removed from the $TiCl_4$ solution, rinsed with ethanol and DI water and dried by flowing air. The $TiCl_4$ treatment on the FTO slides results in the formation of a TiO_2 blocking layer on the slides that prevents the contact between FTO and the electrolyte. The blocking layer minimizes the back electron transfer from the FTO to the electrolyte.

(iii) **Mesoporous layer:** For DSCs employing titania nanoparticle electrodes, a commercially available paste (Dyesol 18 NRT) purchased from Dyesol was used for fabricating the mesoporous layer. For a DSC utilizing all other materials such as tin oxide nanoparticles, tin oxide nanowires and titania nanowires a custom made paste is prepared by the following procedure. The electrodes materials are sonicated for 10 minutes in a 10 Wt % triton-X solution. The dispersion is then centrifuged at 300 rpm for 10 minutes. The supernatant is removed and sediment is separated and used for further steps. The sediment is weighed and an equal weight of ethyl cellulose dissolved in terpineol is added (weight ratio of ethyl cellulose: terpineol = 1:4) and mixed in a mortar until a uniform paste is obtained.

The paste is doctor bladed on the conductive side of the FTO using a scotch tape as a spacer. The scotch tape is removed and the FTO slide is heated to 500 ° C for 1h to remove the organics and sintering the electrode materials.

(iv) **Scattering layer**: After cooling the slides down to room temperature, the scotch tape is reapplied and a titania scattering layer paste comprising of 400-500 nm titania nanoparticles is applied. The scotch tape is removed and slides are sintered at 500 ° C for 1 h and cooled to room temperature. The larger nanoparticles in the scattering layer backscatter the light and enable more efficient light harvesting

(v) The $TiCl_4$ treatment is repeated on these slides and the slides are sintered again at 500 ° C for 30 min.

(vi) **Dye loading:** The FTO slides post $TiCl_4$ treatment are the immersed in a 0.3 mM N-719 dye solution for 12 h to adsorb a monolayer of the dye on the surface of the semiconductor. After 12 h, the slides are removed from the dye solution and rinsed with ethanol to remove the unadsorbed dye. This completes the preparation of the photoanode of the DSC.

(vii) **Preparation of Counter Electrode:** A hole is drilled **i**n a new FTO slide of the same dimensions used for preparing the photoanode. The slide is rinsed with 1 M HCl, acetone and DI water mixture (Volume ratio of HCl: Acetone: Water =2:1:1). The slide is then rinsed with DI water and ethanol and dried by flowing air over it. The plasma cleaning described in Step 1 is repeated. A solution of chloroplatinic acid in ethanol (2 mg/mL) is prepared and a couple of drops of this solution are spread onto the FTO using a cotton swab. The slide is heated at 400 °C for 30 min. This results in the formation of Pt nanoparticles on the slide.

(viii) **Cell Assembly:** A surlyn frame that encompasses the area of the photoanode is cut and placed around the active cell area of the photoanode. The counter electrode with placed on top of the surlyn frame. The assembly is clamped and heated at 80 °C for 3-5 minutes until all the surlyn has melted. The cell is cooled and a couple of drops the iodide triioide electrolyte is placed on top of the hole that was previously drilled in step (vii). A funnel is placed upside down on top of the cell and vacuum is pulled through a neck of the funnel using a rotary vane pump. This displaces the electrolyte into the cell. This technique of filling the electrolyte is called vacuum back filling. The hole is sealed with an epoxy (Crystalbond) to prevent the evaporation of the electrolyte.

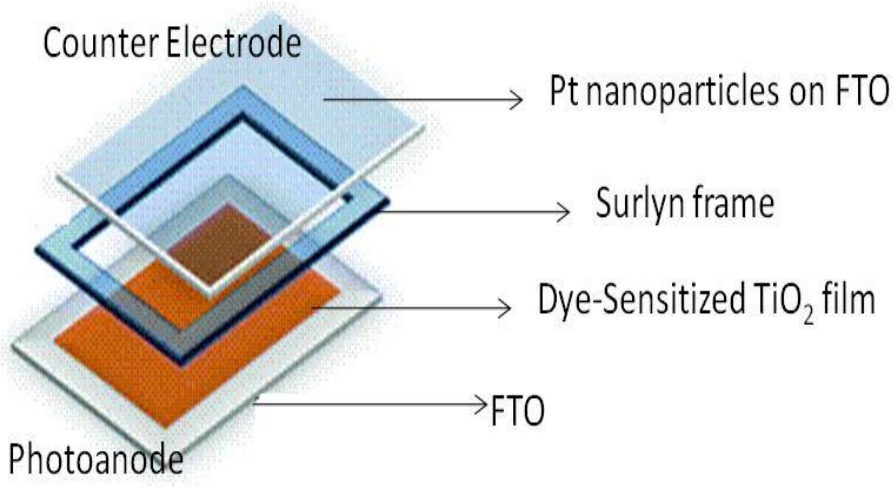

Figure 3.5.1. Schematic showing the different components of a DSC. Reproduced from Ref. [44]

3.6 Procedure for fabricating Perovskite Solar Cells

(i) **Substrate preparation.** Fluorine doped tin oxide (FTO) coated substrates (Hartford glass, USA) were etched using zinc metal powder and 2 M hydrochloric acid. The etched substrates were cleaned by ultra-sonication in an alkaline, aqueous washing solution, rinsed with deionized water, and ethanol and subjected to an oxygen plasma (PLAMAX 150S) treatment for 15 min.

(ii) **Blocking layer deposition:** To deposit the TiO_2 blocking layer, titanium diisopropoaxidebis-acetylacetonate (TAA) was dissolved in 1-butanaol and 0.15 M and 0.3 M solutions of TAA were prepared. The 0.15 M and 0.3 M (three times) TAA solutions were spin coated on the FTO substrates at 4000 rpm for 30s followed by heated the substrates at 500 °C for 30 min. After cooling to room temperature, the substrates were immersed in a 40 mM aqueous solution of $TiCl_4$ for 30 min at 70 °C, rinsed with deionized water and heated at 500 °C for 30 min.

(iii) **Mesoporous layer deposition**: The mesoporous TiO_2 layer was deposited by spin coating a commercial TiO_2 paste (Dyesol-18NRT, Dyesol) diluted in ethanol (1:3.5, weight ratio) at 5000 rpm for 30 s using. After drying at 125 °C, the TiO_2 films were gradually heated to 500 °C for 30 min and cooled to room temperature and $TiCl_4$ treatment was performed again on the substrates.

(iv) **Perovksite deposition:** The sequential deposition procedure developed by Gratzel and coworkers was used for the perovskite deposition.[107]The perovskite deposition discussed as follows was performed in an argon glove box, with humidity less than 1%. A 1.3 M solution of PbI_2 in anhydrous *N*,*N*-dimethyl formamide (DMF) was prepared, and was maintained at 70 °C. The mesoporous

TiO_2 films were then infiltrated with PbI_2 by spin coating the PbI_2 solution at 6500 rpm for 5 s and dried at 70 °C for 30 min. After cooling to room temperature, the film was again coated with PbI_2 by the above procedure and drying the electrode at 70 °C for 30 min. Then the films were dipped in a solution of CH_3NH_3I in 2-propanol (10 mg/ml) for 60 s, rinsed with 2-propanol and dried at 70 °C for 30 min to form the perovskite.

(v) **Protective coating deposition.** The protective coating deposition was performed outside the glove box and is detailed as follows. Solutions of graphene and PANI in 2-propanol are alternatively spin coated to form the composite coating. The procedure is repeated several times to build up the thickness of the composite layers. For instance, a 2x coating denotes that the alternate deposition of graphene and PANI was performed twice in an alternate fashion. Graphene flakes (Cheap tubes, USA) dissolved in 2-proponal (1:10, weight ratio) and the samples are dried for 80 °C for 10 min after spin coated at 2000 rpm for 10s. Then PANI (Aldrich) was dissolved in 2-propanol (2:5, weight ratio) and spin coated at 2000 rpm for 10s followed by drying at 80 °C for 10 min.

(vi) **Device fabrication**. The copper iodide (CuI) used as the hole transport material was then deposited by a doctor blade technique.[108] The CuI solution was prepared by dissolving 0.1 M of CuI in dipropylsulfide (Sigma Aldrich). Following the deposition, the substrates dried at 70-80 °C for 20 min after the doctor blading. The device fabrication was carried out under controlled atmospheric conditions and a humidity of <0.2%. Gold was deposited on separate glass plate by RF sputtering at 80 mTorr and 18 mV conditions for 4 min. The sputtered electrodes are

mechanically pressed onto the copper iodide coated electrode to sandwich the two electrodes.

3.7 Procedure for fabricating Li ion battery coin cells

Electrode preparation: The cathode paste was formed by mixing 10 mg of active electrode with 3mg of teflonized acetylene black (TAB-2) as a conducting binder. A stainless steel mesh is cut in the shape of a disc. The paste was pressed onto stainless steel mesh using a mechanical press. The average thickness of cathode was 18-20 μm. The cathode was dried at 150°C for 5 h under vacuum and then transferred to an Ar filled glovebox.

Cell Assembly: A CR2013 coin-type cell assembled in a dry argon-filled glove box. The different components of the coin cell are depicted in Figure 3.7.1. The electrode on the stainless steel mesh is inserted into the coin cell plate. On top of this electrode a separator comprising of a porous propylene film (ADVANTEC GB-100R) is placed. A couple of drops of electrolyte, enough to soak the separator are placed on the separator. A 1M solution of $LiPF_6$ dissolved in an ethylene carbonate (EC) and dimethyl carbonate mixture (DMC) (Volume ratio of EC: DMC=1:2) is used as the electrolyte. Li metal cut in the shape of a circular disc; the springs and the top cover are stacked on top of the separator. The whole assembly is placed under a crimping machine and the coin cell is crimped to seal battery core in the case.

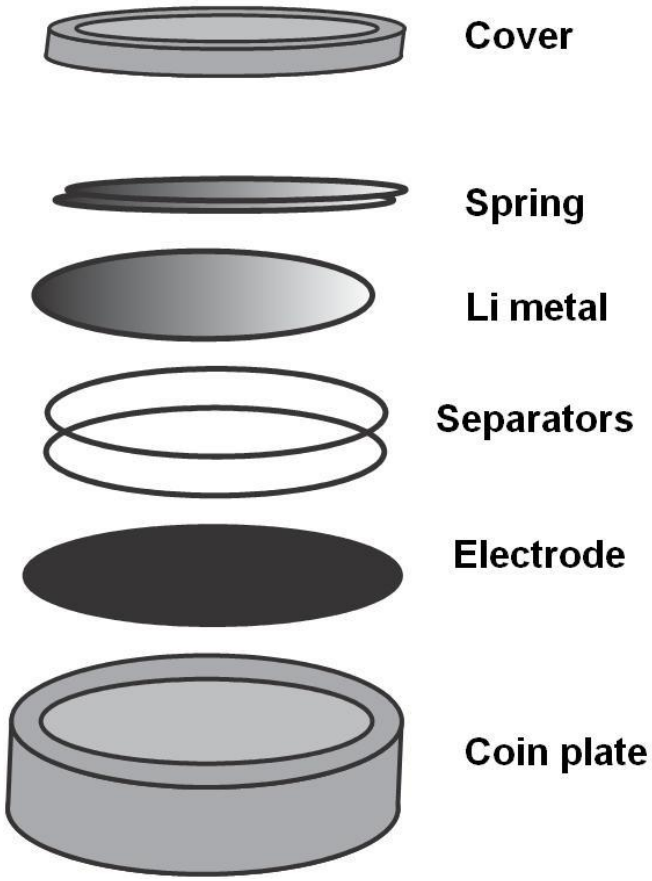

Figure 3.7.1. Different components used in the assembly of a Li ion coin cell.

3.8 Electrochemical Techniques

3.8.1 Current-Voltage (I-V) Characterization

The solar cell under illumination can be treated as the equivalent of a battery. The voltage developed across the two terminals of the cells is isolated, i.e., infinite cell load resistance, is called open-circuit voltage $V_{oc.}$ The current drawn when the terminals are connected (zero load resistance) is called short-circuit current, I_{sc}. The current per unit active of the solar cell is the short-circuit current density J_{sc}. For a finite load resistance

(R_L) greater than zero, the cell generates a voltage (V) and current (I) that can be expressed by the relationship, V= I $R_{L,}$ with current being determined from the I-V characteristic curve. In the dark, the solar cell acts as a diode and current generated in the dark (J_{dark}) flows in the opposite direction as the photocurrent. The dark can be expressed by the following equation.[109]

$$J_{dark} = J_o(\exp\left(\frac{qV}{mk_BT}\right) - 1)$$

Where m is called the ideality factor and takes into account the deviation from ideal diode behavior.

Two internal resistance R_s and R_{sh} are responsible for the lowering of the power conversion efficiency of the solar cell. Series resistance is caused by the resistance coming from the bulk of the semiconductor, metal contacts and the contact resistance of the semiconductor with the metal contacts. Shunt resistance arises from the leakage across the semiconductor junction and the presence of the crystals defect and impurities near the junction. The current voltage characteristics of a solar cell can be expressed by the following equation.[109]

$$J = J_{sc} - J_o\left(\exp(\frac{q(V + JAR_s)}{mk_BT}\right) - 1) - \frac{V + JAR_s}{R_{sh}}$$

where J_o is a constant, and A is the active area of the solar cell.

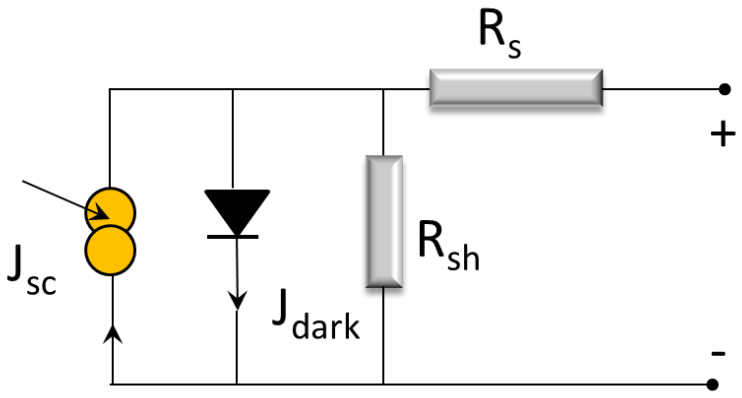

Figure 3.8.1. Schematic depicting the equivalent circuit of a solar cell.

Power conversion efficiency of a solar cell is the ratio of the maximum power(P_{max}) density delivered to the incident light power density (P_s).

$$\eta = \frac{P_{max}}{P_s} = \frac{J_{max}.V_{max}}{P_s}$$

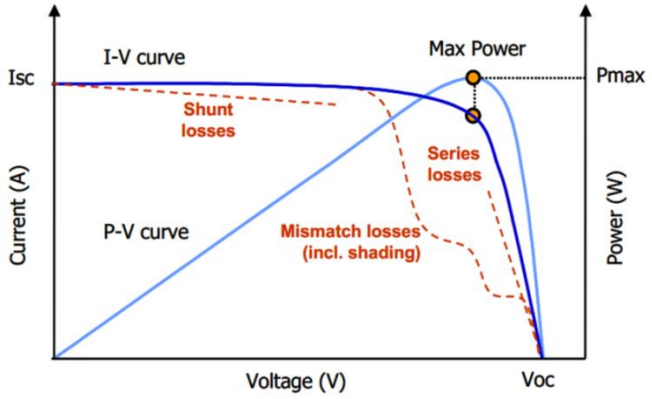

Figure 3.8.2. I-V characteristic curve of a solar cell under illumination. The dotted lines in red show the deviation of the I-V curve due to different losses within the cell.

Figure 3.8.2 depicts the I-V curve of a solar cell under illumination. The red dotted lines near the short-circuit current density and open-circuit voltage represent the deviation in the curve due lowering of shunt resistance and increase in series resistance respectively. The mismatch losses occur when several of the solar cells are connected in module and the photovoltaic parameters of all the cells are not identical. This leads to power dissipation across the inefficient cells, resulting in losses in the overall module efficiency.

The fill factor (FF) is another photovoltaic parameter that quantifies the performance of the solar cell and is defined by the following equation

$$FF = \frac{J_{max}.V_{max}}{J_{sc}.V_{oc}}$$

Hence, from the above equations power conversion efficiency (η), is calculated as

$$\eta = \frac{J_{sc}.V_{oc}.FF}{P_s}$$

3.8.2 Open circuit-Voltage decay technique:

In this technique, the illumination on the solar cells is turned off and the decay of open-circuit voltage of the solar cell is monitored with time. The rate of change of electron density in the film can be expressed as

$$\frac{dn}{dt} = \alpha I_o - U(n) \qquad (3.7.1)$$

where n is the instantaneous electron density in the film and U(n) is the rate of electron recombination with the electrolyte. When the cell is illuminated, the photogenerated electrons are injected into the semiconductor at a rate equal to αI_o, where α is the light

absorption by the dye and I_o is the incident light intensity. The open circuit voltage is defined as the difference between the Fermi-level in the semiconductor and the electrolyte redox potential.

$$Voc = \frac{E_{f_n} - E_f}{q} = \frac{kT}{q} ln \frac{n}{n_o} \qquad (3.7.2)$$

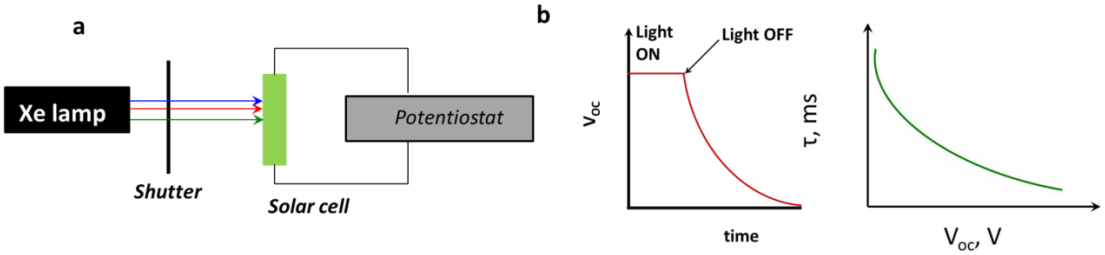

Figure 3.8.3 (a) Schematic illustrating the experimental setup for performing the open-cicrcuit voltage decay method (b) Typical plots of open-circuit voltage decay and plot of electron lifetimes calculated using the voltage decay.

Where n_o is the electron concentration in the dark. When the illumination is turned off

$$\frac{dn}{dt} = -U(n) \qquad (3.7.3)$$

Electron lifetime is defined as $\tau^{-1} = \frac{-1}{n}\frac{dn}{dt}$ (3.7.4)

Hence, $\tau = \frac{n}{U(n)}$ (3.7.5)

From equations (3.7.2) and (3.7.4) $\tau = \frac{-kT}{q}\left(\frac{dVoc}{dt}\right)^{-1}$ (3.7.6)

Equation 3.7.6 has been used to estimate the electron lifetimes in the different electrode architectures developed in this work.

3.8.3 Short-circuit current decay:

Transient short circuit current decay is an electrochemical technique that is used to determine the electron transport time scales in the mesoporous semiconductor network of dye sensitized solar cells. It is based on the theory developed by van de Lagemaat and Arthur Frank.[110]

For a dye sensitized solar cell at short-circuit conditions, the continuity equation for electrons can be written as

$$\frac{\partial n}{\partial t} = G(x,t) + D_n \frac{\partial^2 n}{\partial x^2} \quad (Eq\ 3.7.7)$$

The above equation assumes negligible recombination under short-circuit conditions[111] and non-dispersive or thermalized electron transport where the diffusion coefficient of electrons is not dependent on time and the location of the electrons. $G(x,t)$is the rate of electron injection by the absorber material into the semiconductor network, D_n is the diffusion coefficient of electrons, n is the electron density and x is the spatial location in the semiconductor film.

Solving equation (3.7.7) with the following two boundary conditions[111]

$k_{ext} \,.\, n(0,t) = D_n \frac{\partial n}{\partial x}\Big|_{x=0}$(where k_{ext} is rate of electron extraction)

$$\frac{\partial n}{\partial x}\Big|_{x=d} = 0$$

And using, $J = D_n \frac{\partial n}{\partial x}\Big|_{x=0}$

It can be shown that $J(t) = A.e^{(-\frac{t}{\tau_c})}$ (Eq. 3.7.8)

By fitting a single exponential decay to short-circuit current vs. time curve, the transport time scale τ_c can be determined.

The experimental setup consists of a DSC held at short-circuit conditions using a potentiostat/galvanostat setup and illuminated using a Xe lamp. Light from a laser pulse of a green diode laser (λ =532 nm) is superimposed on the background Xe lamp illumination. The decay of the short-circuit current with time is measured using the potentiostat/galvanostat setup and a single exponential decay given by equation (3.7.8) is fit to the curve to determine the transport time constant.

3.8.4 Incident Photon to Charge Carrier Conversion Efficiency (IPCE)

IPCE measures the fraction of incident photons that are converted to electrons. It is calculated as follows:

$$\text{IPCE} = \frac{\#\text{ of electrons, n}}{\#\text{ of photons, N}}$$

$$\text{IPCE} = \frac{qn}{qN} = \frac{qn/s}{qN/s} = \frac{I\ (amps)/cm^2}{\frac{qN}{s}\ /cm^2} \qquad (2.1)$$

where q is the charge of an electron.

Power, $P\ \left(\frac{W}{cm^2}\ or\ \frac{Joule}{s.m^2}\right) = N.h\ \frac{c}{\lambda}$

h = Planck's constant, c= velocity of light = 3 * 10^8 m/s, λ is wavelength in nm

$$\frac{N}{s.cm^2} = \frac{Power\left(\frac{W}{cm^2}\right) * \lambda(nm) * 10^{17}}{19.86} \quad (2.2)$$

From equations (2.1) and (2.2)

$$\%\ IPCE = \frac{I_{sc}(A) * 1240 * 100}{P(W) * \lambda(nm)}$$

In this technique, the light from a solar simulator is sent through a monochromator. The current density from the solar cells and incident light intensity are calculated at different wavelengths to calculate % IPCE.

3.8.5 Scanning Laser spot technique

Scanning laser spot technique was used in this thesis to determine the spatial variations in voltage across the dimensions of a DSC. In this technique, a small spot size was obtained by passing light from a diode through a small aperture. The spot is rastered along the width of the cell and the variations in photocurrent and photovoltage with distance is measured. Monitoring these variations provides valuable information about edge effects in a dye sensitized solar cell. The experimental setup comprised a 20 mW green laser (Model # GS32-20, Wavelength = 532 nm, Intelite Inc.) was used. The spot size was controlled using an iris (Thorlabs) and was measured to be 0.63 mm in diameter. The laser spot was then rastered laterally across the cell mounted on a XYZ stage and the current and voltage values were recorded using a potentiostat/galvanostat setup. A schematic of the setup is shown in Figure 3.8.4.

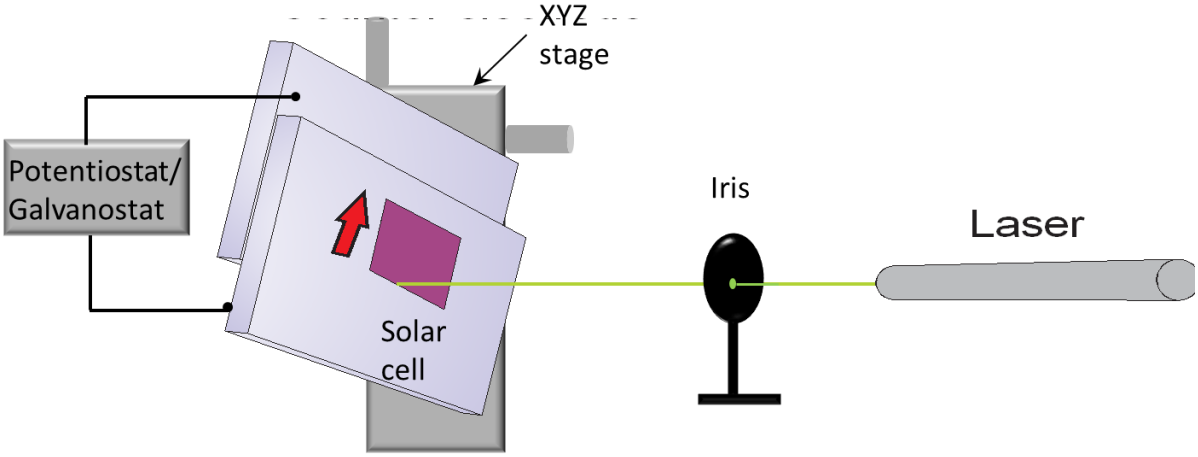

Figure 3.8.4. Schematic showing the experimental setup for the scanning laser spot technique to monitor current density and voltage variations across the width of the cell.

3. 9 Structural Characterization

3.9.1 Scanning electron microscope (SEM)

Scanning electron microscopy is used to obtain morphological information of the samples synthesized in this work. In this technique, the sample is bombarded with electrons from an electron gun, resulting in the emission of secondary electrons from the valence shell of the constituent atoms of the sample and the scattering of the incident electrons as backscattered electrons. The secondary electrons emanating from the sample and are detected using an Everhart-Thomley detector. The secondary electrons have smaller energies when compared to the incident electrons and the backscattered electrons, typically less than 50 eV. This would mean the secondary electrons emitted from the bulk of the sample are absorbed by the sample and only the secondary electrons near the surface of the sample reach the detector. Hence the secondary electrons are very surface sensitive give information regarding the surface of the sample.

3.9.2 Transmission Electron Microscopy (TEM)

The TEM is used to detect the elastically scattered electrons that are transmitted through the specimen. For a crystalline sample, the electrons diffract through the crystal planes of the sample and can interfere to form a diffraction pattern Images in the TEM can be obtained either in the bright field (BF) mode or dark field mode.[112] High Resolution TEM (HRTEM) is another mode in the TEM used for high resolution imaging of crystalline material and can provide resolution up to 0.8 A°.[113]In this technique several diffracted beams are used to form the image. The crystal planes in the sample that are parallel to the direction of propagation of the electron beam will be diffracted according to the Bragg's law. This diffraction pattern is a Fourier transform of the periodic potential of the electron in two dimensions. These diffracted electrons along with the electrons in the primary interfere leading a back transformation (or inverse Fourier transform) of the diffracted pattern to the periodic electron potential, thereby resulting in an enlarged image.

3.9.3 X-Ray Diffraction (XRD)

XRD is an experimental technique for obtaining crystallographic information of the material such the space group of the crystal, interplanar spacing, grain sizes, long range order.[114, 115] The generation of X-rays is achieved using an X-ray tube comprising of heated tungsten filament enclosed in an evacuated ceramic vessel. Electrons thermionically emitted from a tungsten cathode are accelerated towards a water cooled metal (typically copper) which acts as the anode. The electrons reaching the Cu anode losing their energy by two mechanisms. Firstly, the electrons can decelerate as they approach the nuclear cores of the atoms in the anode due to opposing electric field from the nucleus towards the

valence electrons. This type of deceleration produces Bremsstrahlung X-rays (meaning braking radiation in German). Secondly, the electrons can knock out the electrons in the inner shells of the Cu atoms. Electrons in the valence shells relax to the inner shells and the difference in energy is emitted in the form of continuous X-rays. In case of Cu, characteristic X-rays of two wavelengths namely Cu K_α (λ = 0.154 nm) and Cu K_β (λ = 0.139 nm) are produced. The detector is usually a scintillation counter, which measures the intensity of the diffracted X-rays in counts. The peaks observed in a diffraction pattern correspond to the particular angles at which the diffracted X-rays from the sample interfere constructively. This is described the Bragg's law of diffraction as follows

$$n\lambda = 2d\sin\Theta$$

where n is an integer, d is the interplanar spacing, 2Θ is the angle between the incident X-ray beam and the diffracted X-ray beam.

Scherrer equation, described the following equation, has been employed in this dissertation to calculate the crystal grain sizes.

$$\tau = \frac{K.\lambda}{\beta.cos\Theta}$$

Where τ is the crystalline grain size, λ is the wavelength of X-rays, K is the dimensionless shape factor (typically 0.9 for nanoparticle morphology) and Θ is the Bragg angle.

CHAPTER 4

FUNDAMENTAL STUDIES OF ELECTRON DYNAMICS IN DYE-SENSITIZED SOLAR CELLS

As discussed earlier in Chapter 2, replacing iodide redox couple with non-corrosive redox couples is necessary to improve the device durability. In this chapter, fundamental studies related to understanding electron transport and recombination in nanoparticles, nanowires, nanoparticle/nanowire hybrids are performed. The factors causing slow electron transport in nanoparticle architectures and application of nanowires and their hybrid architectures are investigated for using iodide free dye-sensitized solar cells are studied. Specifically, the role of surface traps states and surface passivation of these trap states are investigated. The knowledge gained from these studies would be of significant importance for designing electrodes for dye-sensitized solar cells that employ alternate redox couples.

4.1 Electron dynamics in nanoparticle based architectures

The electron transport in nanoparticle networks is limited due to the poor interconnectivity between the nanoparticles leading to longer time scales for electron transport through the nanoparticle films and high recombination rates. One possible approach to overcome this problem is to form electron transport bridges between the nanoparticles. This could be achieved by adding a stable precursor that decomposes to form these bridges on decomposition during the sintering process of nanoparticles. (Figure 4.1.1)

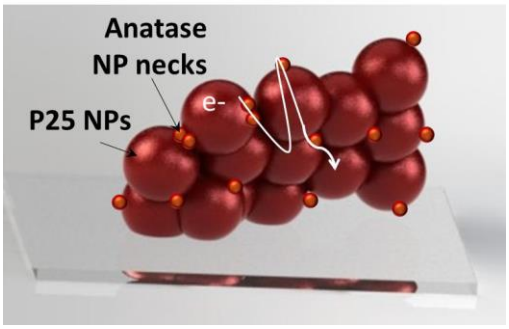

Figure 4.1.1 Schematic depicting the formation of bridges between commercially available P25 TiO_2 NPs to improve electron transport and lower electron recombination.

To study this hypothesis, titania nanoparticles are chosen and a water soluble titanium precursor namely, titanium (IV) bis(ammonium lactato)dihydroxide (TALH) was used. At the temperature used for sintering titania nanoparticle electrodes (~ 500 ℃), TALH decomposes according to the following reaction.

$$\mathbf{[CH(O-)CO_2NH_4]_2Ti(OH)_2 + 5O_2 \xrightarrow{500^oC} TiO_2 + 2NH_3 + 6CO_2 + 6H_2O}$$

The formulation to fabricate the titania nanoparticle films was designed by adding a small amount of TALH to a dispersion of commercially available P25 TiO_2 nanoparticles in water. Prior studies using dispersion of P25 nanoparticles in water showed poor efficiency due poor interconnectivity between the nanoparticles. The formation of electron transport bridges should show clearly show a remarkable improvement in efficiency due to improved electron transport and lowered electron recombination losses.

To validate the formation of TiO_2 during the thermal decomposition of TALH at 500ºC, the powder obtained by the thermal decomposition was analyzed by XRD. The XRD pattern of titania nanoparticles obtained by thermal treatment of TALH is shown in Figure

4.1.2. The dominant characteristic peak at 25.4°, 2θ was assigned to the (101) Miller index of anatase. The diffraction pattern of the titania nanoparticles formed by thermal decomposition of TALH showed other characteristic peaks of the anatase structure, corresponding to (004), (200), (211), and (213) crystalline planes (JCPDS schedule: 21-1272).

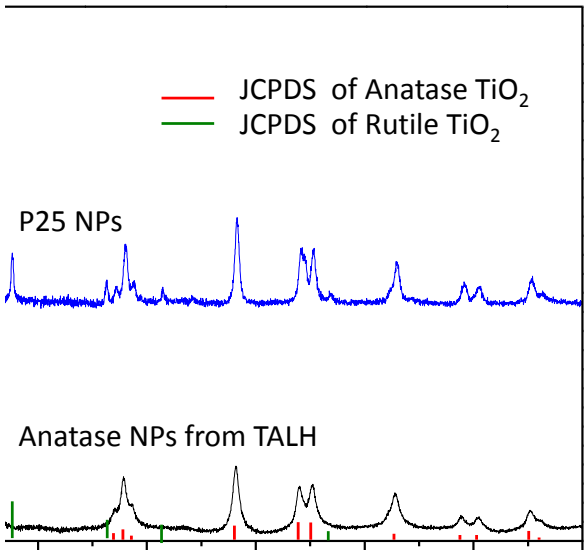

Figure 4.1.2 XRD diffraction pattern of anatase nanoparticles (NP) formed from thermal decomposition of TALH at 500 ℃.

The broader peaks in the XRD pattern of the titania formed by thermal decomposition of TALH when compared with commercially available P25 nanoparticles suggest smaller grain size according to Scherer equation. Thus, the anatase titania from the decomposition of TALH should result in the bridging between the P25 nanoparticles.

To validate the observation from XRD and further understand the morphology between the TiO_2 formed from thermally decomposed TALH and the P25 particles, the nanoparticle films were studied using high resolution TEM (Figure 4.1.3). High resolution TEM (HRTEM) images of P25 titania nanoparticles shows a rough surface on nanoparticles (Figure 4.1.3a), which implies a high number of uncoordinated surface defect sites which act as electron traps and recombination centers.[116, 117] HRTEM images of anatase TiO_2 nanoparticles obtained by thermal decomposition of TALH (Figure 4.1.3b) show that these nanoparticles are smaller in size than the P25 titania nanoparticles.

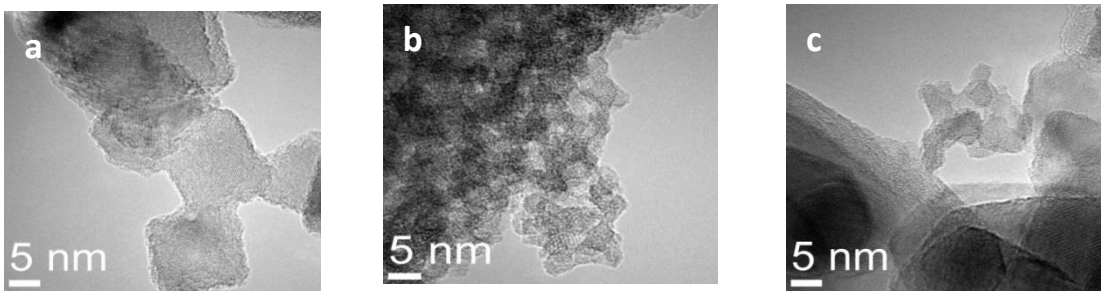

Figure 4.1.3. Transmission electron microscopy image of titanium dioxide nanoparticles after sintering – (a) P25 nanoparticles (b) anatase titanium dioxide NPs from TALH sintered at 500ºC and (c) P25 nanoparticles with anatase nanoparticle bridging formed from TALH.

Further, the anatase nanoparticles are observed to form bridges between the larger P25 nanoparticles (Figure 4.1.3c) respectively. This observed bridging results in the improved electron transport between P25 nanocrystals. Current-voltage characteristics of single layer DSCs fabricated from titania formulations with varying TALH concentrations are shown in Figure 4.1.4 and summarized in Table 4.1. DSCs fabricated from formulations

without TALH exhibit a short-circuit current density (J_{sc}) of 10.8 mA/cm^2, an open circuit voltage (V_{oc}) of 0.71V, a fill factor (FF) of 0.63, and an overall conversion efficiency (η) of 4.8%. These results are in agreement with a prior report using binder-free H_2O/t-butanol formulation.[118] As the TALH concentration in the aqueous P25 formulation was increased, the J_{sc}, V_{oc} and η increased until a maximum was reached at 0.43 molar (M).

Table 4.1. Performance of DSC with various TALH concentrations

Concentration of TALH, M (P25:TALH, molar ratio)	**J_{sc}, mA/cm^2**	**V_{oc}, V**	**FF**	**η, %**
0	10.8	0.71	0.63	4.8
0.04 (55.8:1)	10.9	0.71	0.61	4.8
0.14 (17.5:1)	16.4	0.73	0.56	6.7
0.43 (6.5:1)	16.64	0.74	0.66	8.1
1.30 (2.8:1)	13	0.7	0.64	5.8

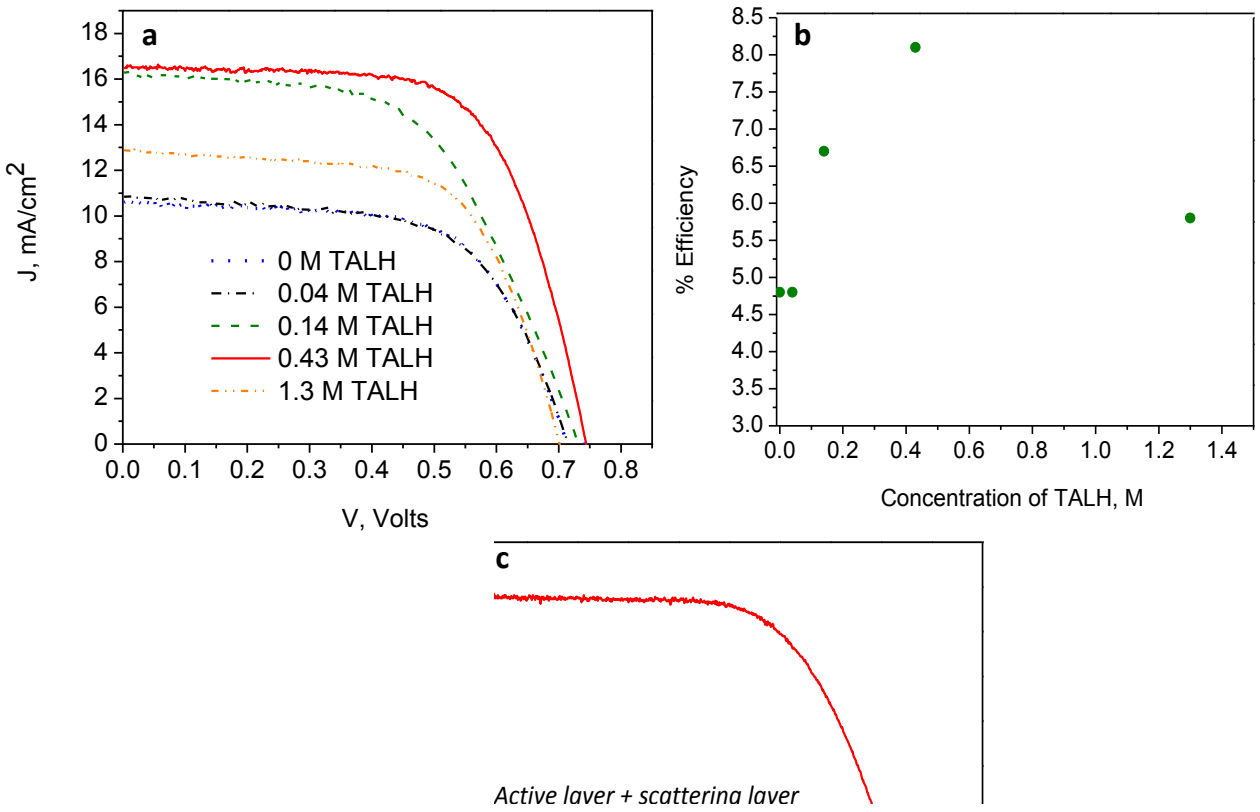

Figure 4.1.4 (a) Current-Voltage characteristics, (b) overall efficiency of DSCs fabricated with formulations containing different concentrations of TALH with active and layer only and, (c) Current-Voltage curve for an optimized formulation with both active layer and scattering layer.

A DSC prepared with blocking and scattering layers sandwiching the mesoporous layer using the optimized formulation resulted in an efficiency of 9.2%.

Further increase in TALH concentration in the formulation beyond the optimum concentration resulted in lower performance reducing both the V_{oc} and J_{sc}. Both the V_{oc} and J_{sc} are maximized at a TALH concentration of 0.43M that would suggest improved electron transport due to better electrical connectivity between the P25 TiO_2 particles. Further, increased surface area resulting in the higher dye loading and contribute to observed increase in the photovoltaic performance of the cells. To verify this hypothesis, electron transport and recombination and the dye loading characteristics, changes in the film morphology are investigated.

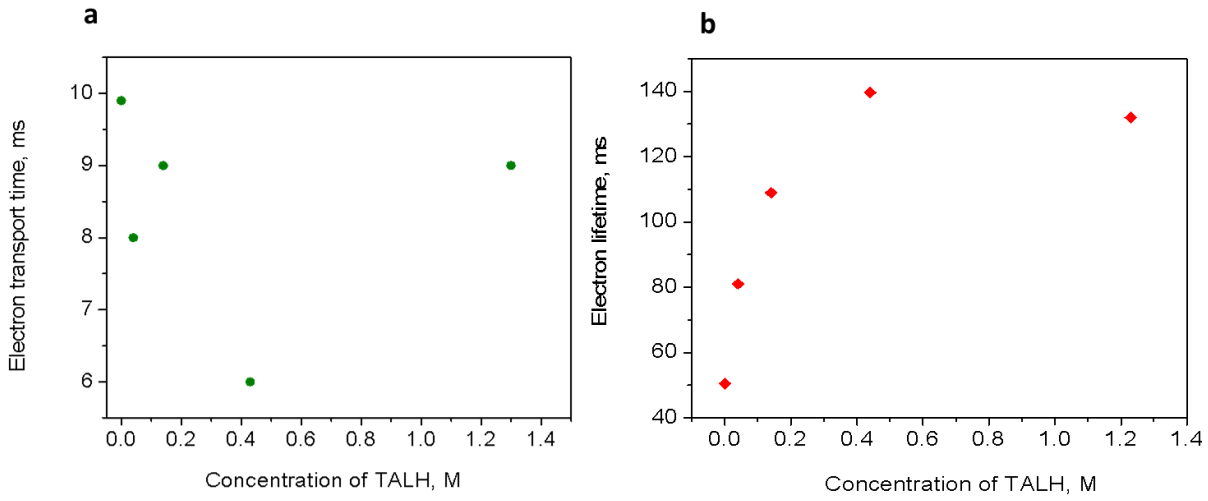

Figure 4.1.5 (a) Electron transport time constant and (b) electron lifetimes for DSCs fabricated with varying amounts of TALH.

Improved bridging between neighboring P25 titania nanoparticles by thermal decomposition of the TALH precursor leads to improve electron transport and lower recombination in the film. The electron recombination time constant and transport time

constant for DSCs made with different TALH concentration are shown in Figure 4.1.5are in agreement with studies using ethyl cellulose based pastes.[119]

The highest electron lifetime and the lowest transport time constants are observed with DSCs fabricated with formulation containing optimum TALH concentration (0.43 M TALH) and these closely correlate with observed maximum DSC performance. Faster electron transport and suppressed electron recombination also suggests that addition of TALH improves interconnections between the nanoparticles. The passivation of surface trap states can also lead to reduction in of transport time scales and improvement of electron lifetimes. Specifically, Ti^{3+} trap states have been reported to limit electron transport in TiO_2 films and the passivation of these states with increasing TALH concentration could be a likely reason for the observed improved electron transport. X-ray photoelectron spectroscopy (XPS) is used to determine the surface passivation of the films. Figure 4.1.6a shows the Ti 2p XPS spectrum of the titania films prepared with different TALH amounts. The Ti 2p3/2 and Ti 2p1/2 peaks at 458.3 eV and 464 eV indicate titanium in its +4 state. The lack of any peaks at 457.6 eV shows that there is no Ti^{+3} (457.6 eV) in any of the samples. Analysis of the XPS results shows that improvement in the transport and recombination properties with addition of TALH is not due to passivation of the Ti^{+3} traps. To further corroborate this observation, a chronoameperometric technique developed by Wang *et al.* was also used to measure the surface trap state concentration. The current decay in this technique is related to the filling of the surface traps states in TiO_2. The concentration of the traps can be estimated from the charge accumulated in these traps obtained by integrating the area under the current transients. Concentration of surface traps

remained constant at 10^{13} cm^{-2} indicating that no new trap states are created with the addition of TALH (Figure 4.1.6 b).

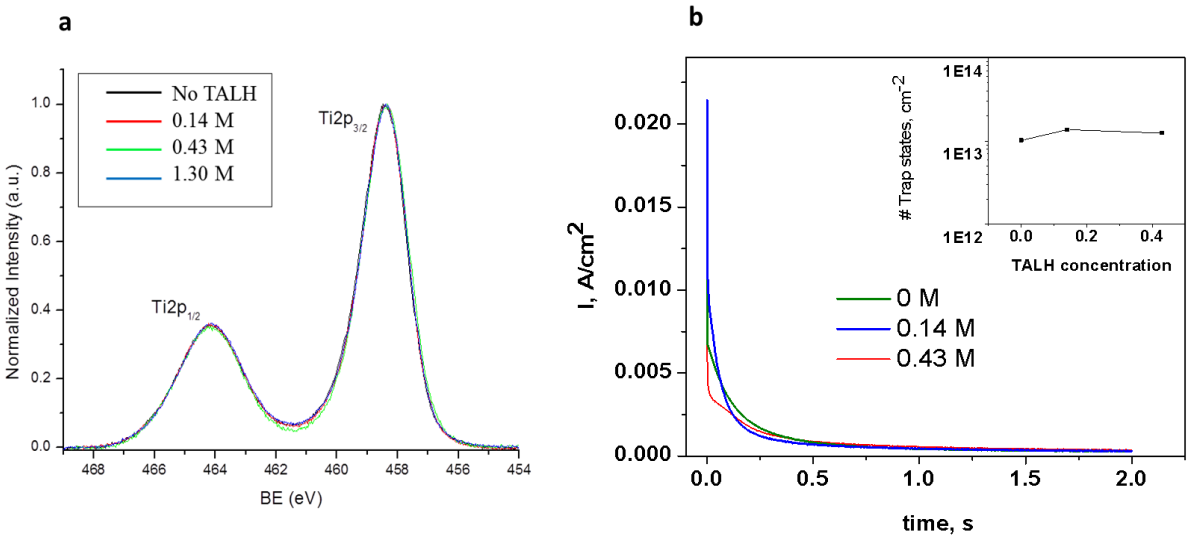

Figure 4.1.6 (a) XPS spectrum for different TALH concentrations (b) chronoampereometry measurements at -0.8 V Ag/AgCl in a 0.5 M $LiClO_4$ electrolyte, inset shows the surface density of trap states, at varying concentrations of TALH.

The porosity of the nanoparticle films has also been shown to be a significant factor affecting the solar cell performance and could explain the trends in recombination and transport at higher TALH concentrations. At very low porosities observed for high TALH concentrations the transport of electrolyte redox species into the pores is slow resulting in inefficient dye regeneration.[120] Further, the slow transport of electrolyte results in slow regeneration of the dye and increases recombination losses with oxidized species. It was also shown that the adsorption of the dye passivates the surface states on the TiO_2 particles, reducing the recombination losses. At very high porosity, surface trap states that increase the electron transit time and electron recombination and fewer coordination sites would imply a longer path for the electron to travel. Consequently, the slower electron transport

also leads to increased recombination losses in the TiO_2 film. The porosity of the P25 nanoparticle film is reduced at high TALH concentrations (> 1M) and the electron transit time would be expected to be faster when compared to transit times in the films made from the optimized formulation. The slower electron transport at high such concentration can be explained through fissures created during the thermal decomposition of TALH. Fissures in the nanoparticle film result in a longer path for the electron to travel to reach the conducting substrate, thus resulting in a slower transport time scale. The changes in the film morphology with varying TALH concentrations were analyzed by scanning electron microscopy. SEM images of the nanocrystalline mesoporous films prepared using formulation containing 0, 0.14, 0.43, and 1.30 M TALH is shown in Figure 4.1.7. The images clearly indicate that the porosity and hence the surface area of films increases with TALH concentration. BET measurement of the surface area resulted in 53 m^2/g for pure P25 nanoparticle film, and is 60 m^2/g for the titania nanoparticle films at the optimal TALH concentration. UV-Vis measurements on the dye-sensitized films made with varying TALH concentrations showing increased absorbance with increasing TALH concentration (Figure 4.1.7e) also support the observation from SEM.

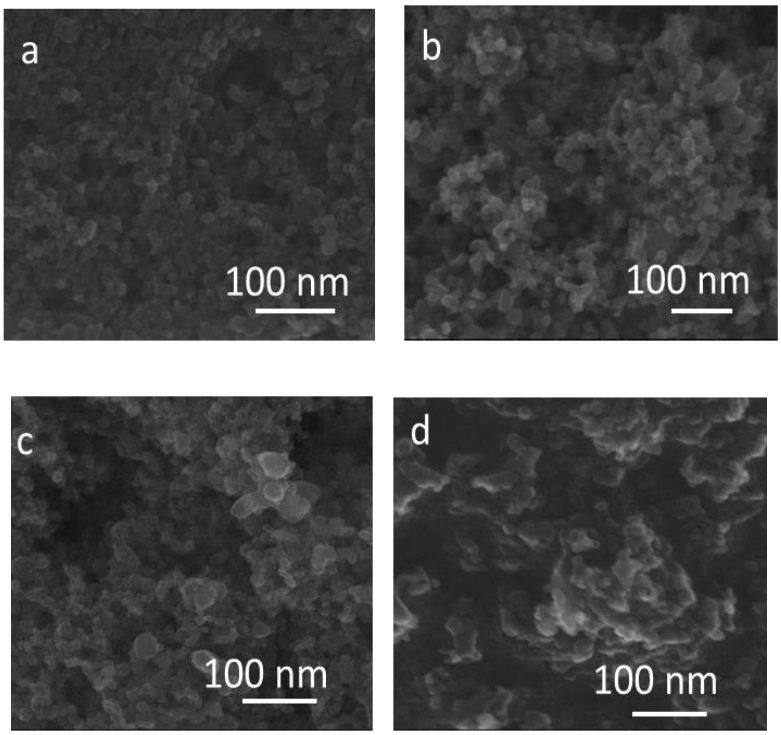

(e)

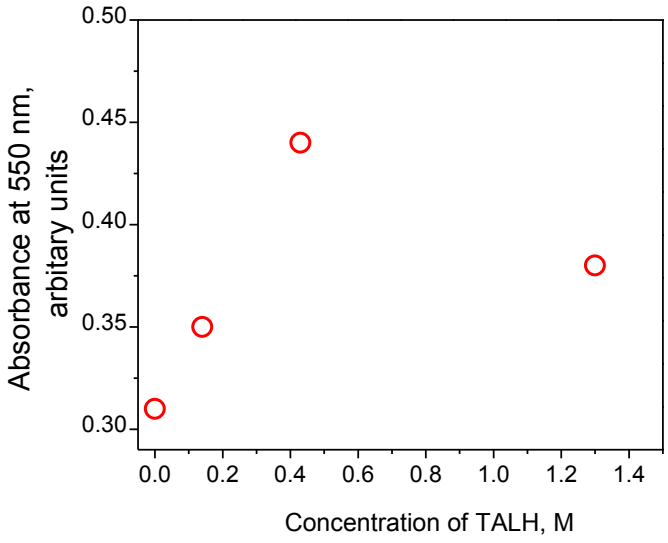

Figure 4.1.7. Scanning electron images of titanium dioxide films fabricated with formulations containing varying amount of TALH (a) 0 M TALH (b) 0.14 M TALH (c)

0.43 M TALH (d) 1.30 M TALH. (e) Absorbance of N-719 dye on the titanium dioxide films fabricated with varying TALH concentrations.

4.2 Electron Dynamics in Nanowires and Nanoparticle/Nanowire Hybrid architectures

The electrolyte used in the dye-sensitized solar cell plays an important role is determining the electron dynamics in the semiconductor films. The electron transport and recombination kinetics are with the conventional iodide redox couple and alternate one electron redox couples are studied with different photoanode architectures of titania and tin oxide. The results from these studies give important information crucial for designing photoanode architectures especially with one electron redox couples.

4.2.1 Studies with iodide/triiodide redox couple

The electron recombination kinetics with iodide/triiodide redox couple are slow (on the order of several milliseconds). This permits a comparison of electron lifetimes in different nanoparticle and nanowire based architectures without any surface modifications. Figure 4.2.1.1 shows the electron lifetimes in tin oxide based architectures in DSCs using the iodide redox couple. Tin oxide nanowires show the highest electron lifetimes which are two orders or magnitude higher than that of tin oxide nanoparticles.

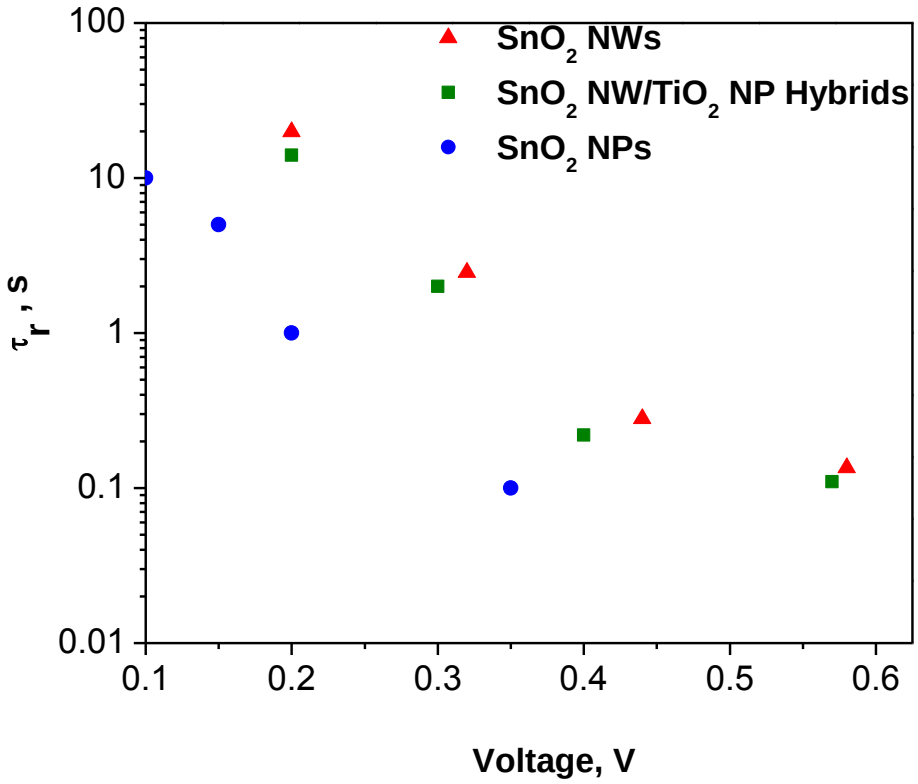

Figure 4.2.1.1. Electron lifetimes in tin oxide NWs, tin oxide NPs and tin oxide NW/titania NP Hybrids.

However, dye adsorption measurements showed that the loading of the dye is much higher on titania NPs when compared with tin oxide NWs due to the low surface area of SnO_2 NWs. To circumvent this problem tin oxide NW are coated with titania NPs by electrophoretic deposition to form hybrid architectures. The hybrid architectures possess electron transport and recombination properties close to that titania NWs and improve the dye loading. To further improve the dye loading, it would be advantageous to use single crystalline titania NWs if they possess enhanced transport and recombination properties.

Single crystalline titania NWs are synthesized by a solvo-plasma process as described in Chapter 3. Electron transport, recombination of commercially available P25

titania NPs, titania NWs (rutile phase) and hybrid architectures of titania NPs/titania NWs are illustrated in Figure 4.2.1.2. It can be seen that hybrid architectures and NWs of titania posses much higher electron lifetimes while the transport time scales in the nanoparticles, nanowires and nanoparticle/nanowire hybrids of titania are all similar, in spite of the titania NWs being single crystalline. This can be explained by understanding the location of transport limiting traps also plays significant role in determining the transport properties. In the case of tin oxide nanowires, the majority of the transport limiting traps are located very close to the conduction band edge at 0.071 eV below the conduction band edge,[121] while in titania nanoparticles majority of the traps are located at 0.24 eV below the conduction band edge.[122] The steeper trap state location in titania nanoparticles results in longer time scales for the release of the trapped electrons and hence slower electron transport in titania nanowires.

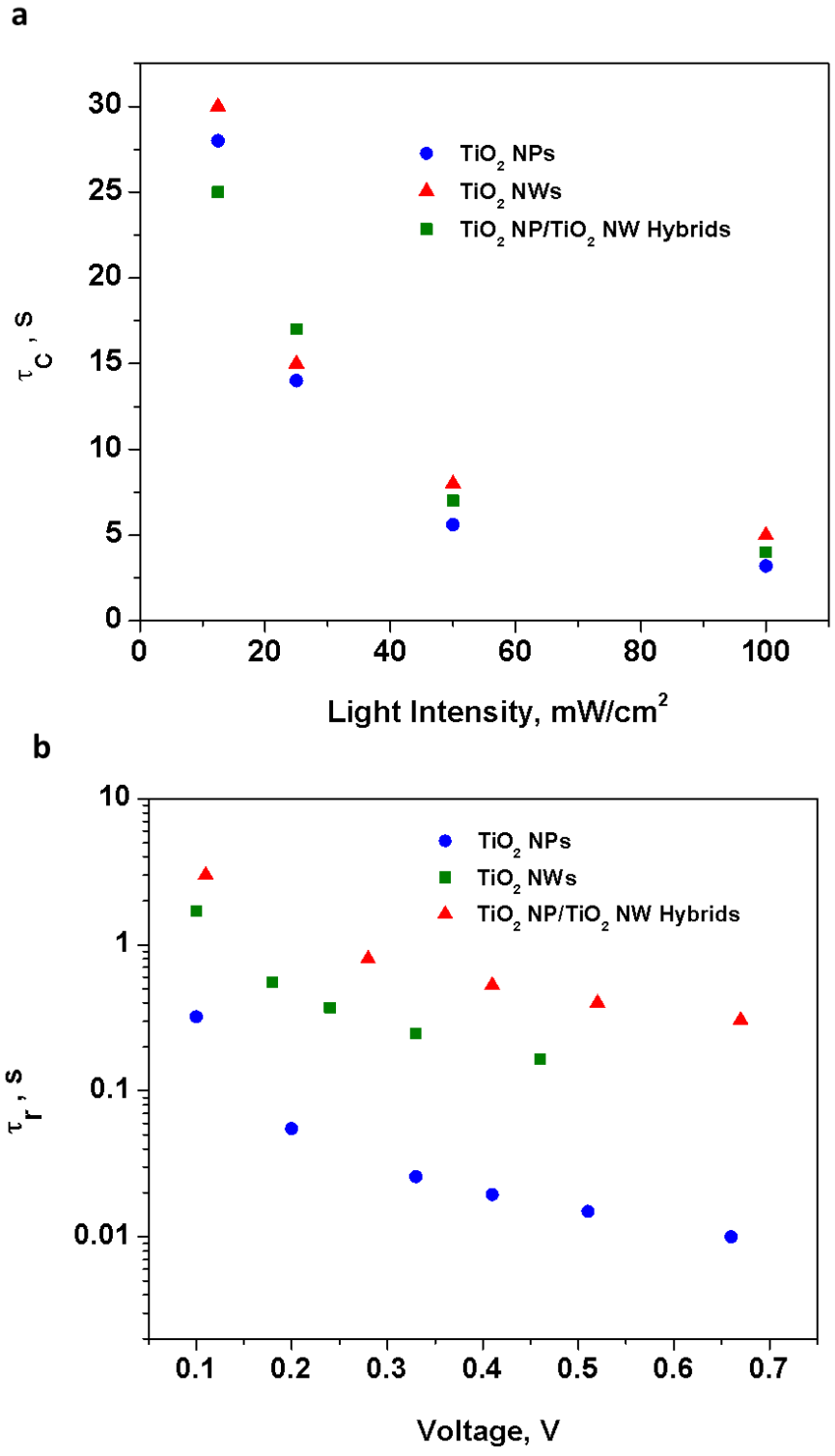

Figure 4.2.1.2. (a) Electron transport and (b) recombination time scales in DSC with titania NW and NP based architectures using iodide redox couple.

4.2.2 Studies with alternate redox couples

As discussed in the prior section the tin oxide nanowire/ titania nanoparticle hybrid architectures were found to have the highest electron lifetimes among the different electrode architectures employing iodide redox couple. The role of surface traps and their passivation is not very critical for iodide redox couple because of the slow recombination kinetics. However, with one-electron redox couples with very fast recombination kinetics the surface passivation becomes very important and trends in the electron recombination after surface passivation need not necessarily follow the same trend as observed with iodide redox couple. To investigate the effects of surface passivation when employing alternate redox electrolytes, the electron lifetimes with tin oxide nanowires/titania nanoparticle hybrids and titania nanoparticles were measured in DSCs employing two different redox couples namely ferrocene/ferrrocenium and TEMPO/$TEMPO^{+}$ were studied. The electrodes were passivated with one cycle of Al_2O_3 by atomic layer deposition. Interestingly, the electron lifetimes in titania nanoparticles were found to be higher than electron lifetimes in tin oxide nanowire/titania nanoparticle hybrid architectures (Figure 4.2.1.3). The trends in the electron transport time scales were found to be similar to those seen with iodide redox couple (Figure 4.2.1.4)

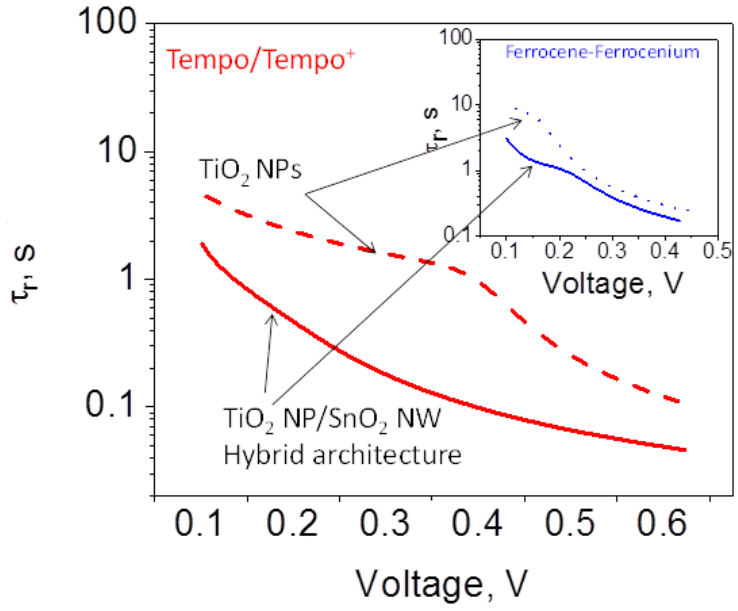

Figure 4.2.1.3. Electron lifetimes in tin oxide NW/titania nanoparticle architectures and titania nanoparticles in DSCs fabricated with alternate one-electron redox couples.

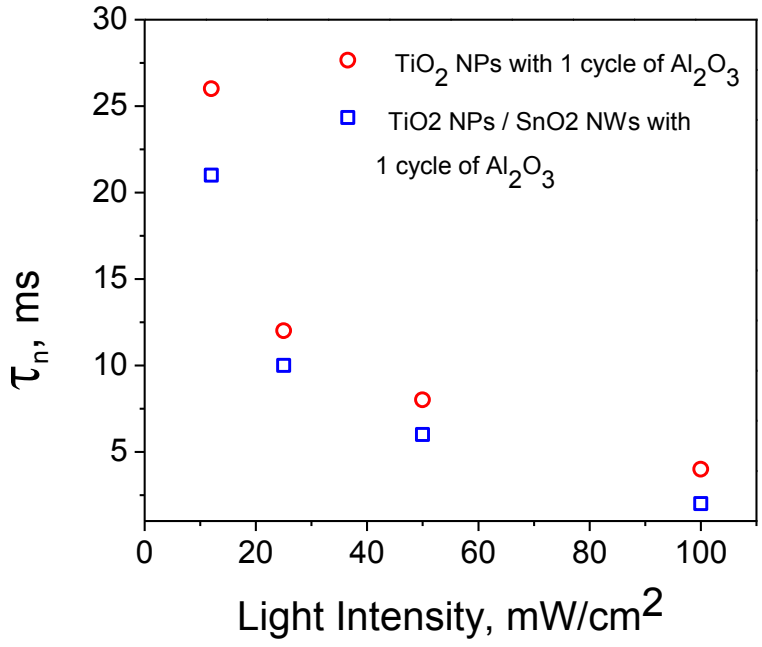

Figure 4.2.1.4. Electron transport times scales in tin oxide NW/titania nanoparticle architectures in DSCs fabricated with alternate one-electron redox couples.

These results suggest that passivation of surface traps can lead to dramatic changes in the trends of electron lifetimes after surface passivation. In addition factors such as the surface area, surface chemistry and band edge alignments of the core and shell materials also affect the electron lifetimes. The electron lifetimes in different nanoparticle, nanowires, nanowires/nanoparticle hybrids of tin oxide and titania are measured with DSCs employing TEMPO redox couple (Figure 4.2.1.5).

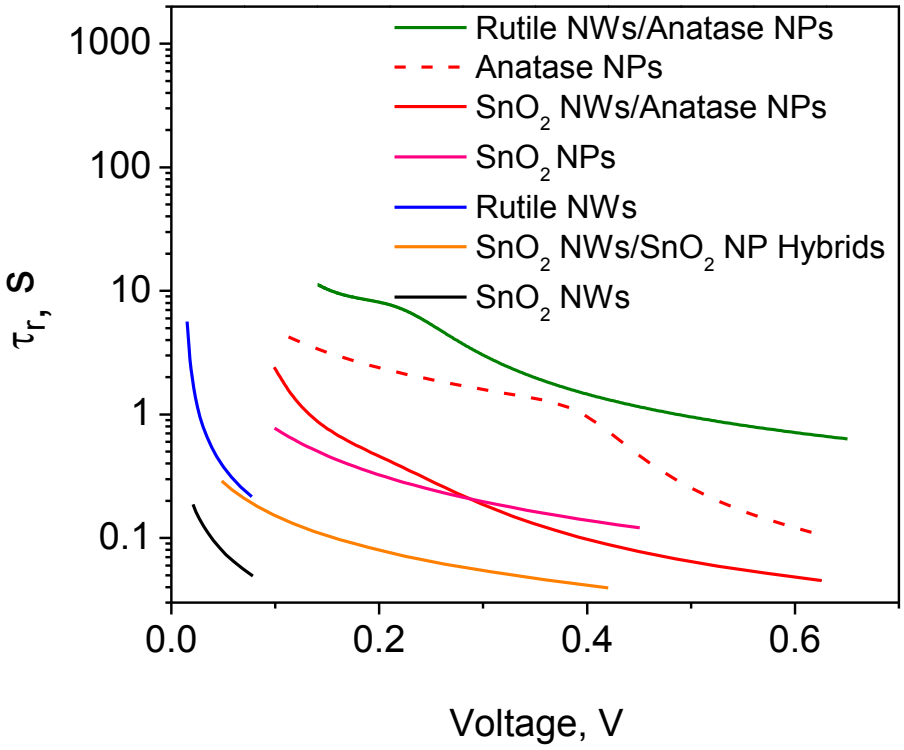

Figure 4.2.1.5 Electron lifetimes in different electrode architectures passivated with Al_2O_3in DSCs using TEMPO redox couple.

The trends observed in Figure 4.2.1.5 for surface passivated electrodes indicate that electron lifetimes in nanoparticles are always higher than those in nanowires. Further, higher electron lifetimes are observed in titania nanoparticles and architectures having titania nanoparticles at the surface. These results indicate the surface area and the number

of surface sites available for adsorption of Al_2O_3 are critical in determining the electron lifetimes in the electrodes. Further, the high affinity and surface sites available on titania surface when compared with the tin oxide surface could be the reason for higher electron lifetimes in titania based architectures when compared to tin oxide based architectures. The higher electron lifetimes in hybrid architectures can be explained by the band edge offsets between the core and shell material that retard the back electron transfer as shown in Figure 4.2.1.6.

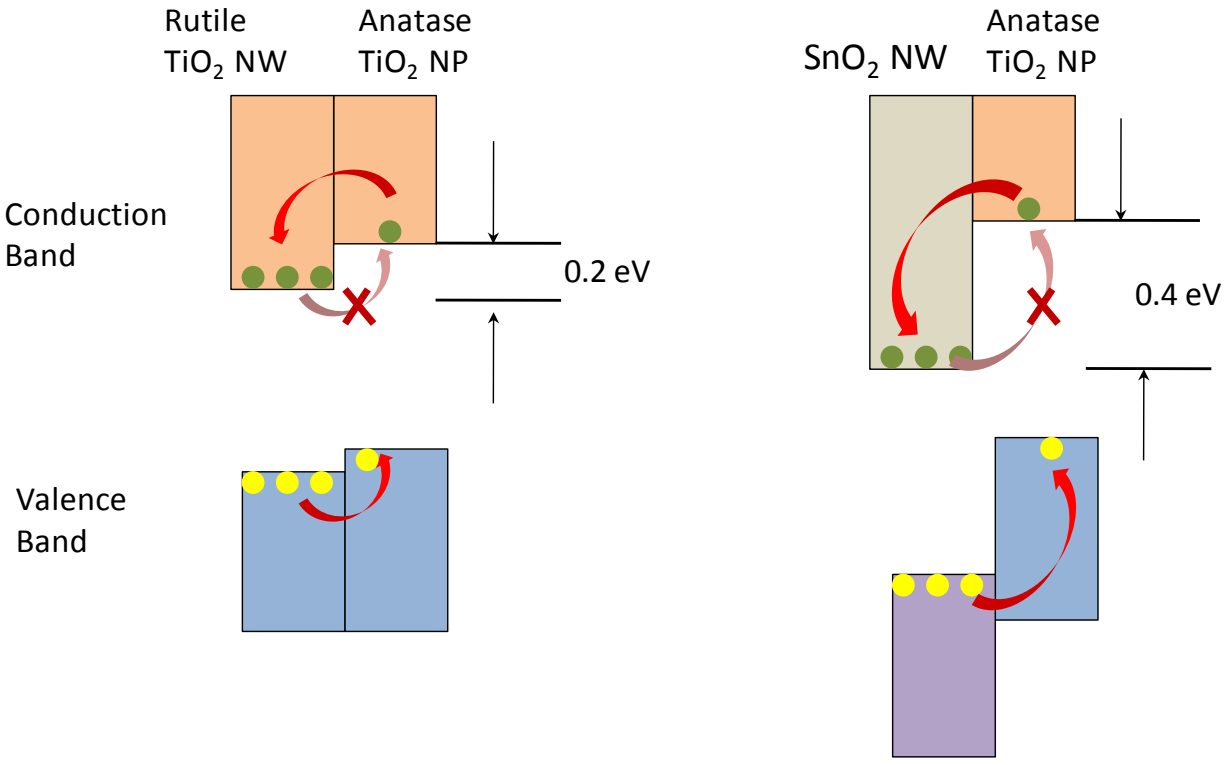

Figure 4.2.1.6 Band edge offsets between the core and shell of the hybrid architectures prepared in this work, prevent back electron transfer from the core back to the shell.

4.3 MacroscaleEffects: Influence of electrode dimensions on electron transport and recombination:

As discussed in the previous sections, the nanoscale morphology and crystallinity have significant effects on the electron transport and recombination. Several fundamental studies exploring the effect of cell geometry of a DSC focused on the photovoltaic performance as a function of the photoanode film thickness.[8,18-20] Current densities will increase along with the film thickness due to higher dye loading leading to more photogenerated carriers. As the film thickness is increased beyond the diffusion length, the open-circuit voltage and short-circuit current begin to drop as a result of high recombination rates and slow electron transport. Further, it is important to answer the question – Do the macroscale dimensions of the electrode affect the electron transport or recombination? especially when the lateral dimensions of the electrode are small. Even more, the fundamental reasons that give rise to these variations in the electron dynamics need to be understood. Simulations by Lund et al. showed a spatial distribution of tri-iodide along the lateral dimension of the DSC, but the physical origin of these edge effects was not discussed.[32] Understanding these edge effects is important in the design of new DSC geometries.

To understand these macroscale effects, the variations in short-circuit current density (J_{sc}), open-circuit voltage (V_{oc}), efficiency (η) and fill factor (FF) were investigated for DSCs of different photoanode areas ranging from 1 cm^2 to 0.01 cm^2. Transient photocurrent decay and transient photovoltage decay were also employed to determine the transport and recombination characteristics fundamental to the observed changes to the J_{sc} and η. Several photoanode architectures including nanoparticles, nanowires and

nanoparticle/nanowire hybrids were fabricated to examine how the recombination kinetics within the photoanode changes with area for these architectures. A scanning laser spot technique was used to map the spatial distribution of photovoltage to understand how the edge effects arise in DSCs.

The performance of DSCs made using P25 titania nanoparticles (J_{sc}, V_{oc}, FF and % η as a function of photoanode is shown in Figure 4.3.1. The results indicate that the short-circuit current density does not stay constant as cell area is reduced (Figure 4.3.1 a). Below a certain photoanode area (< 0.1 cm^2), the J_{sc} of the cells increases exponentially from a constant 5 mA/cm^2 for an area greater than 0.1 cm^2 to 12 mA/cm^2 for a 0.01 cm^2 area.

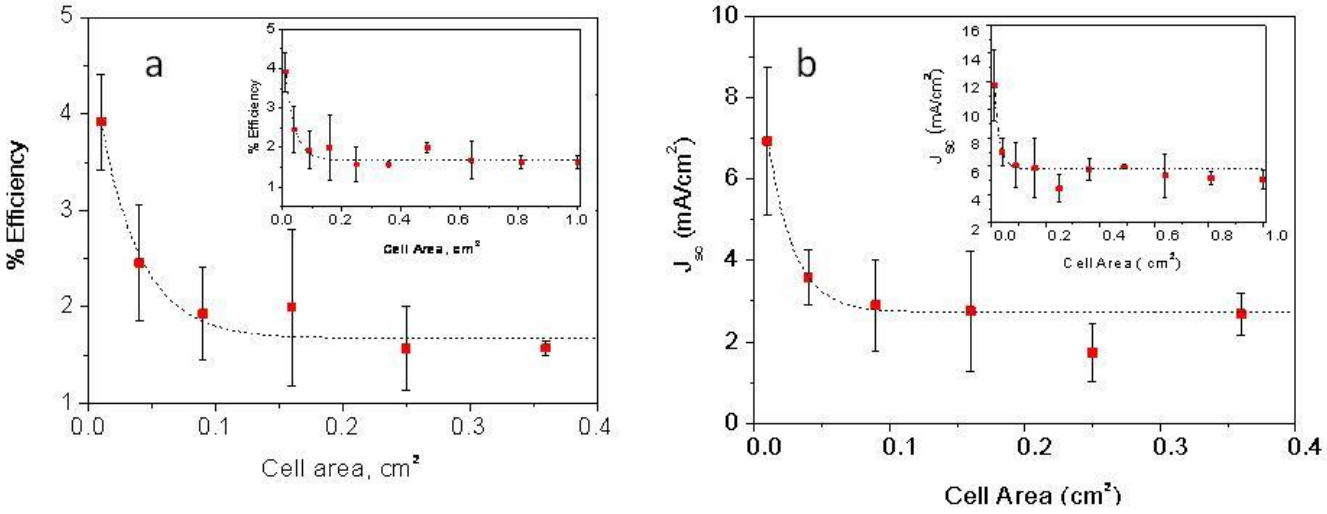

Figure 4.3.1. (a) Short-circuit current density and (b) Efficiency of DSCs fabricated using P25 titania nanoparticles as a function of photoanode area at 1 sun illumination (100 mW/cm^2). Inset shows the change in short-circuit current density vs. area for larger cell areas.

However, there is no significant change in the V_{oc} of the cells, which remained at 680 mV as the photoanode area is varied. Similarly, the FF of the cell undergoes a minor change from 0.45 for a 1 cm^2 cell to 0.52 for a 0.01 cm^2 cell and this small change in fill factor cannot completely account for the substantial variation in J_{sc} values (Figure 4.3.2).

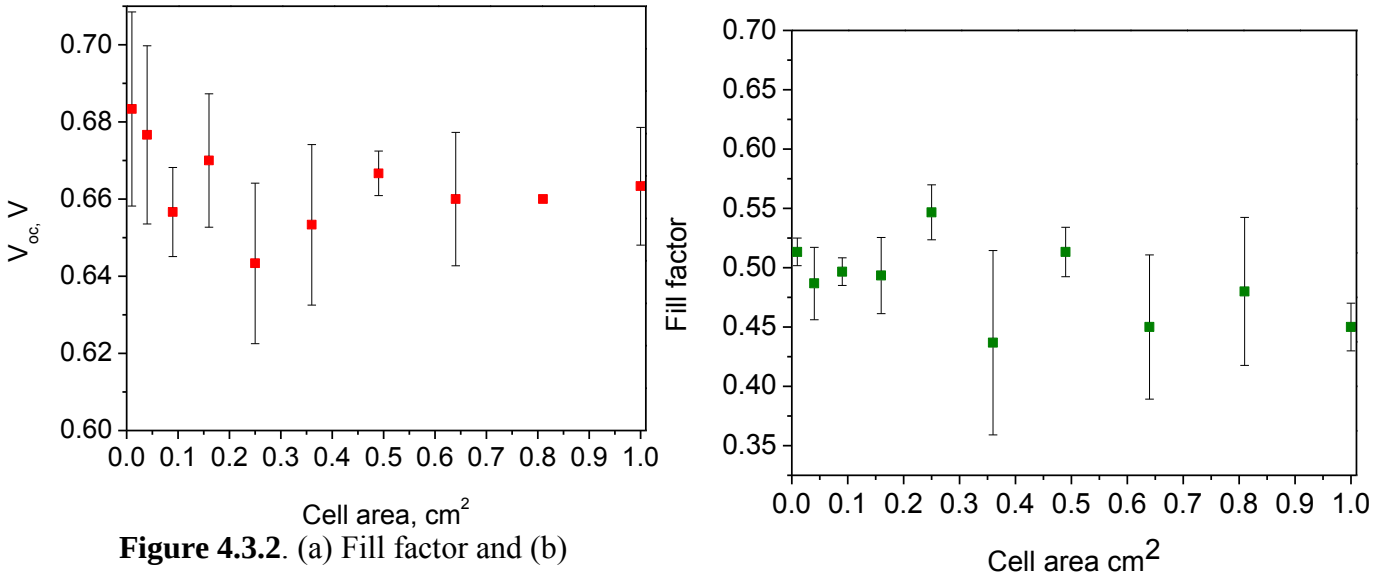

Figure 4.3.2. (a) Fill factor and (b) open-circuit voltage for DSCs of different areas constructed from titania nanoparticles.

The electron transport and recombination time scales were studied as a function of the photoanode area of the DSC using transient short-circuit current decay and transient open-circuit voltage decay respectively. The electron transport time constant (τ_n), the average time an electron takes to diffuse through photoanode film, remained constant (~8 ms) as the photoanode area varied (Figure 4.3.3 a). A different trend in the electron lifetime (τ_r), the average time a generated electron spends in the photoanode before recombining, was observed as the cell area was reduced (Figure 4.3.3 b). The electron lifetimes increase exponentially as the area is reduced below 0.1 cm^2. These results suggest that the increase

in J_{sc} is due to a reduction in the recombination of generated electrons, with a higher number of electrons making it to the conducting electrode for small area cells.

Figure 4.3.3.(a) Transport time constants at 1 sun illumination and (b) recombination

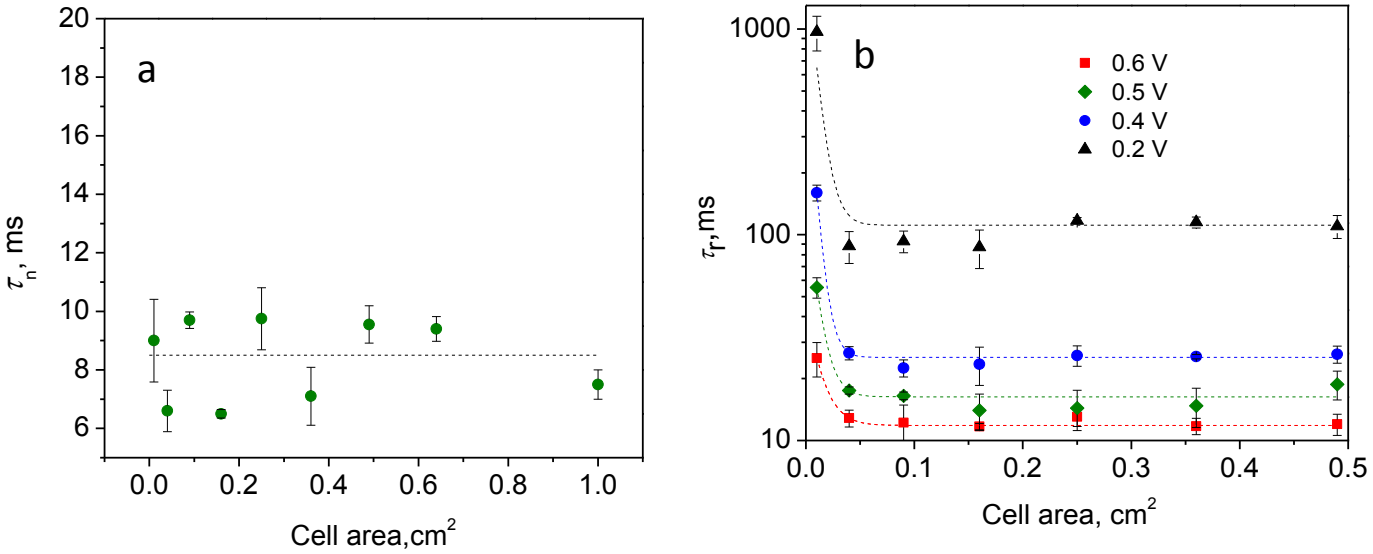

time scales for cells fabricated from P25 titania nanoparticles as a function of cell area. The error bars represent the standard deviation from the measurements on three cells.

These results clearly indicate that the recombination kinetics within the photoanode are affecting the photovoltaic characteristics of DSCs as the area is reduced. Recombination characteristics are material dependent and it has been earlier shown that tin oxide nanowires exhibit slower recombination rates; therefore, have been included in this study. Specifically, Gubbala *et al.* have shown that the recombination time scales in tin oxide nanowires are two orders of magnitude higher when compared to DSCs fabricated from tin oxide or titania nanoparticles (NP).[13,25] Photoanodes from tin-oxide nanowires (NW) and tin oxide nanowire/titania nanoparticle composites are used to investigate DSC

performance as a function of the photoanode area. As before, the J_{sc} and η of the devices increases as the area is reduced below 0.1 cm^2. (Figure 4.3.4)

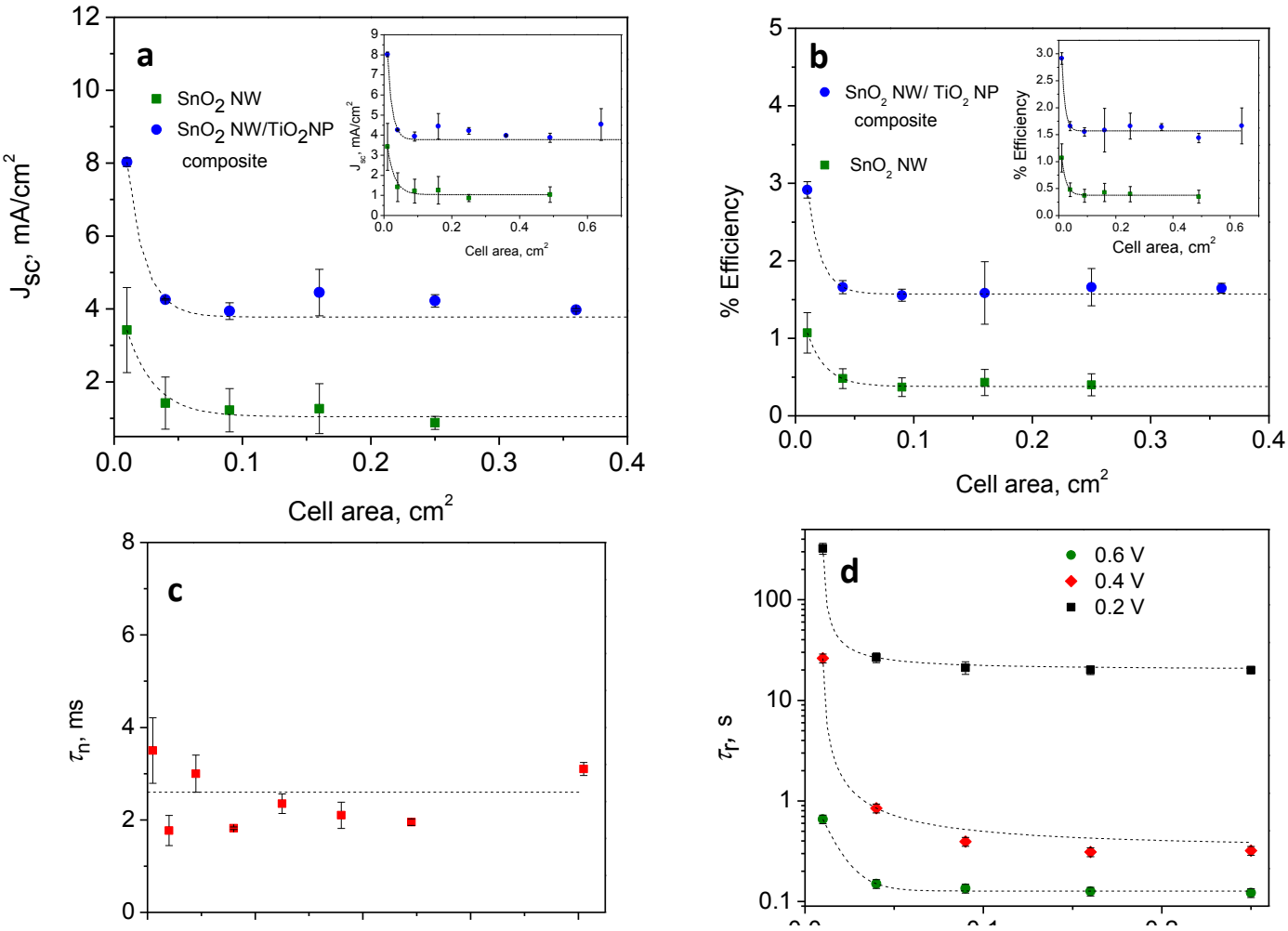

Figure 4.3.4. (a) Short-circuit current density and (b) % efficiency of DSCs fabricated using tin oxide NW and tin oxide NW/titania NP composites as a function of photoanode area at 1 sun illumination, (c) Transport time constants at 1 sun illumination and (d) recombination time constants for cells fabricated from tin oxide nanowires as a function of

cell area. The error bars represent the standard deviation from the measurements on three different cells.

The V_{oc} remains constant with a variation in area (~ 600 mV for SnO_2 NW and 660 mV for SnO_2 NW/TiO_2 NP composite). The transport time constants for tin oxide NW DSC is relatively unaffected by a change in the cell area (Figure 4.3.4c). On the other hand, the recombination time constant increases with a reduction in the cell area below 0.1 cm^2, similar to the trend observed in DSCs fabricated with titania NPs (Figure 4.3.4d). The percentage increase in the short-circuit current density and efficiency (with a reduction in area from 1 cm^2 to 0.01 cm^2) for tin oxide NW based photoanodes was found to be similar to photoanodes made from titania NPs even though tin oxide NWs exhibit very low recombination rates.

These results suggest an underlying fundamental effect causing the electron lifetimes to increase as the cell area is reduced below 0.1 cm^2. Electron lifetimes are a function of cell voltage and the spatial variation in cell voltage could give rise to a distribution of electron lifetimes spatially along the lateral dimension of the photoanode. The open-circuit voltage decay technique measures the average electron lifetime of the distribution, which is found to increase as the cell area is reduced. Salavador et al. obtained a photopotential profile of a titania photoanode immersed in catechol and salicylic acid and found a non-uniform distribution across the lateral dimension of the film with a minimum at the edge rising to a maximum at the center.[29] The magnitude of photopotential is proportional to photocurrent[30] and hence the photocurrent would follow a similar profile as that of the photopotential, resulting in the electron concentration being low at the edges and high at the center of the photoanode area. Scott and co-workers employed a similar

technique and showed that there was spatial variation of photocurrent in DSCs with currents at the center of the cell being higher than the edges.[31] Lund and co-workers performed numerical simulations to described edge effects in DSC and showed that there is lateral inhomogeneity in current distribution and tri-iodide concentration.[32] However, the physical origin of the edge effect was not explained in their study.

To understand edge effects, the scanning laser spot technique is employed to study the spatial variations in photocurrent and photovoltage. Analysis of the photopotential distribution across the lateral dimension of the photoanode shows that as the photoanode area is reduced below 0.1 cm^2, the photovoltage profile becomes narrower, with a lower photovoltage at the edges and maximum photovoltage at the center of the cell (Figure 4.3.5), although the average voltage value remained constant.

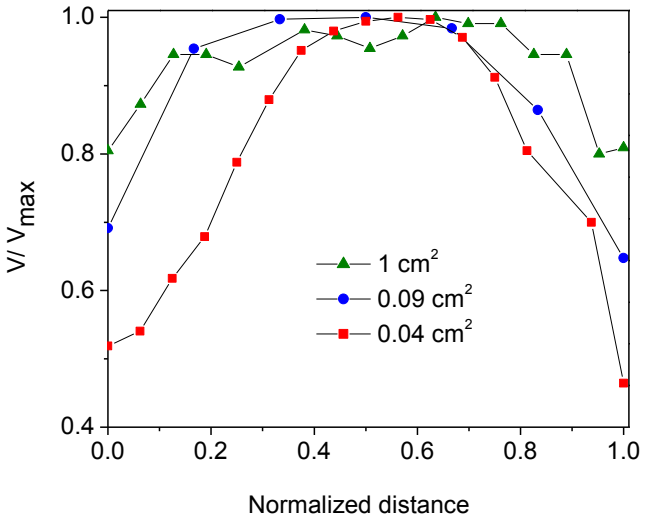

Figure 4.3.5 Normalized photovoltage profiles along the lateral dimension of different area P25 nanoparticle based DSCs obtained using the scanning laser spot technique.

The photovoltage distribution is very non-uniform with a maximum value at the center and minimum value at edges, even for cells with an area of 1 cm^2. Interestingly, the photopotential profile is still very non-uniform for cells with area of 1 cm^2. The recombination time scale is a function of photovoltage and can be determined spatially across the area using the experimental data. The voltages, $V_{expt}(x)$, observed in the scanning laser spot technique were low compared to the results obtained in Figures due to the low intensity of the laser light source used. Voltage distribution at higher V_{oc} (high light intensity), $V_{int}(x)$, can be determined using the following interpolation:

$$V_{int}(x) = \left(\frac{V_{expt}(x)}{V_{avg}}\right) \cdot V_{oc} \qquad (1)$$

where the average voltage V_{avg} is determined by calculating the area under the curve of the measured voltage profile.

Table 4.3.1. Comparison of calculated and experimental electron lifetimes at 0.5 V and 0.7 V for DSCs fabricated from titania (P25) nanoparticles.

area [cm^2]	**V_{avg}**	**$\tau_{r,calc}$ [ms] at 0.5 V**	**$\tau_{r,expt}$[ms] at 0.5 V**	**$\tau_{r,calc}$[ms] at 0.7 V**	**$\tau_{r,expt}$[ms] at 0.7 V**
1	0.34	25.3	20.8	15.6	11.1
0.09	0.32	26.4	23.5	16.8	10.3
0.04	0.32	29.5	25.1	18.5	13

Table 2 shows the values of the calculated and observed average time constants of cells of different areas for the solar cells fabricated from titania nanoparticles.

The observed recombination time scales match well with the calculated values, further suggesting that the non-homogeneity in voltage distribution strongly influence the recombination time scales as the area is reduced and thereby contribute to an increase in the average electron lifetime. As the electron lifetime is a function of photovoltage, [25]the region near the edges (corresponding to 600-700 microns length) of photoanode, that constitutes a significant portion of smaller photoanodes, operates at a lower photovoltage and will have slow recombination kinetics than the center. This would result in increased average electron lifetimes for smaller photoanodes. The increased electron lifetimes lead to a reduction in the recombination current density and as a result, the net current density, the difference between electron injection and recombination current densities, is increased.[30]Consequently, an increase in the J_{sc} and η are associated with the increased electron lifetimes, although the average cell voltage remains the same.

The non-uniformity in the voltage across the lateral dimension of a DSC would affect how the power conversion efficiency and electron lifetimes are reported as these would vary as a function area. The efficiency is directly related to short-circuit current density as follows.

$$\eta\eta = \frac{J_{sc} \cdot V_{oc} \cdot FF}{P_{in}} \qquad (2)$$

An increase in the J_{sc} results in an increase in η as there is negligible change in V_{oc} and FF as the photoanode area is varied.

Similarly, the diffusion length scale, which is the average distance the electron travels in the photoanode film before it recombines, is affected by the non-uniform voltage distribution, and is related to the electron lifetime according to the equation

$$L = \sqrt{D_n \cdot \tau_r} \qquad (3)$$

Where D_n is the electron diffusion coefficient and τ_r is the electron lifetime. An increase in the electron lifetime would increase the average length scale when the diffusion coefficient or the transport time scale is constant. So, the increase in diffusion length creates an opportunity to optimize the thickness for increased photogeneration balancing the recombination currents, leading to further increase in J_{sc}. Therefore, while testing a new material for use in DSCs, an increase in cell performance due to the new material can only be claimed if the spatial variation in voltage is less predominant.

To verify if highly efficient DSCs also show an area dependent efficiency, photoanodes with a layered structure comprising of a compact TiO_2 nanoparticle layer formed by $TiCl_4$ treatment, followed by an active layer (particle diameter ~ 15 nm) and scattering layer (particle diameter ~ 200 nm) were fabricated. Unlike the P25 nanoparticle or tin oxide nanowire photoanodes, no significant variations in the efficiency with a change in area were observed (Figure 4.3.6).

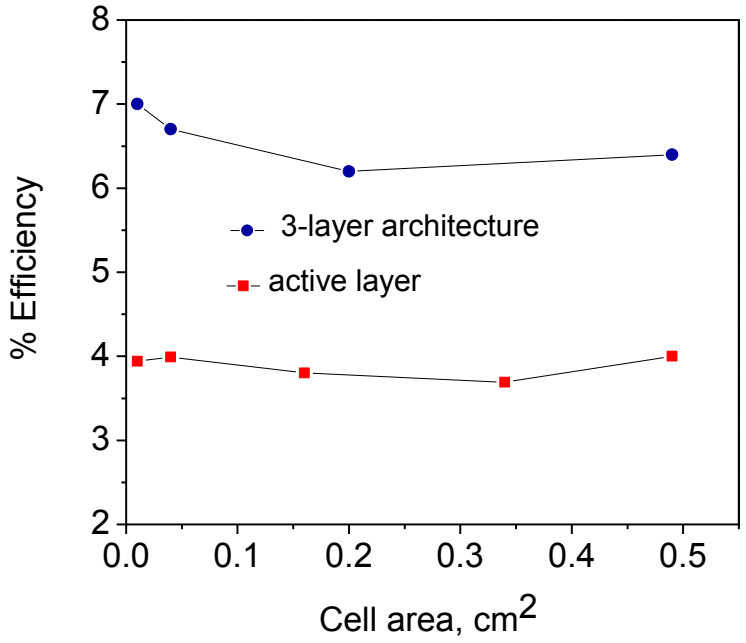

Figure 4.3.6 Efficiency vs. area for DSC fabricated with commercially available anatase nanoparticles with only an active layer and with 3-layer configuration. The 3-layer architecture comprises of a compact layer formed by $TiCl_4$ treatment, an active layer made from commercially available 15 nm anatase nanoparticles (Dyesol). The scattering layer comprised of anatase titania nanoparticles (Dyesol) of 200 nm in diameter.

A similar trend was noticed when the compact layer formed by $TiCl_4$ treatment or the scattering layer was excluded during the photoanode fabrication. Further, there was no significant spatial variation in the photopotential across the lateral dimension of the photoanodes of different areas and this would explain why no variation in the efficiency with area is observed for these cells (Figure 4.3.7).

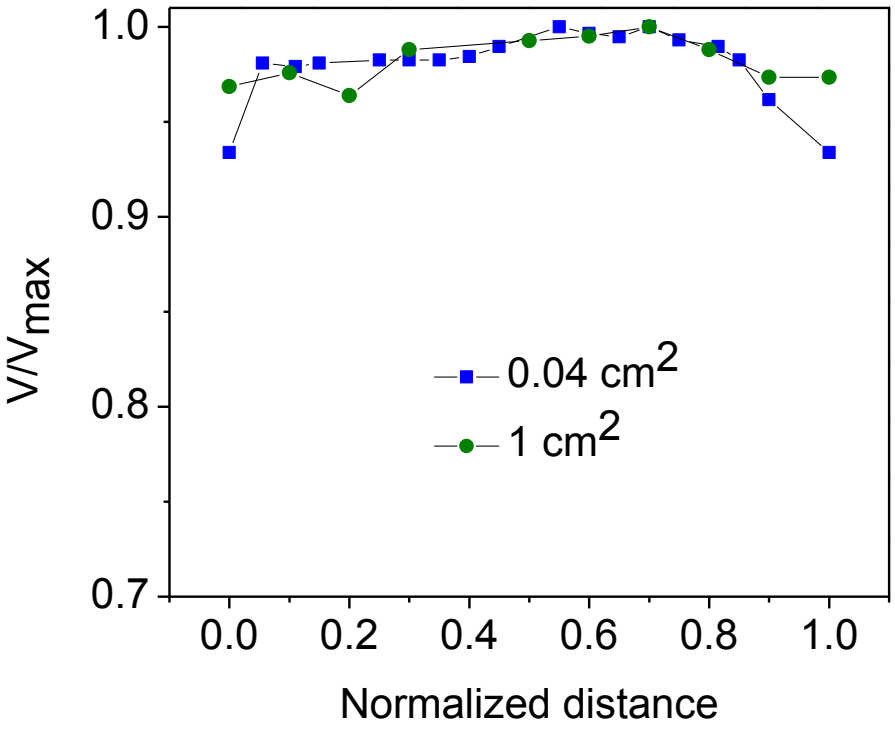

Figure 4.3.7. Normalized photovoltage profile along the lateral dimension of the cell for DSCs of different areas fabricated using only active layer of anatase titania nanoparticles.

A markedly higher dye absorption was clearly observed for photoanodes fabricated for the anatase titania nanoparticles when compared with the P25 nanoparticles. A possible explanation for the difference in photopotential profiles for the P25 and anatase nanoparticle electrodes could be that the dye binds more strongly to the anatase titania nanoparticle electrodes.

Gratzel et al. discussed the different modes of dye anchoring on to a metal oxide surface such as covalent attachment, electrostatic interactions, hydrogen bonding, hydrophobic interactions and physisorption.[33] Typically, the carboxylic acid group of the dye is known to form a chemical link to surface groups on titanium dioxide nanoparticles. Previous studies have also shown that besides particle size, the surface of TiO_2 and

preferential adsorption of dye on certain crystal planes can influence the overall adsorption or desorption of the dye on titania.[34-36] To test the hypothesis of preferential dye desorption at the edges of the P25 photoanodes, the photopotenital profiles for 0.04 cm^2 area device were obtained using a DSC fabricated with P25 nanoparticles sensitized with the N-719 dye and then infiltrated with a quasi-solid state electrolyte (Figure 4.3.8).

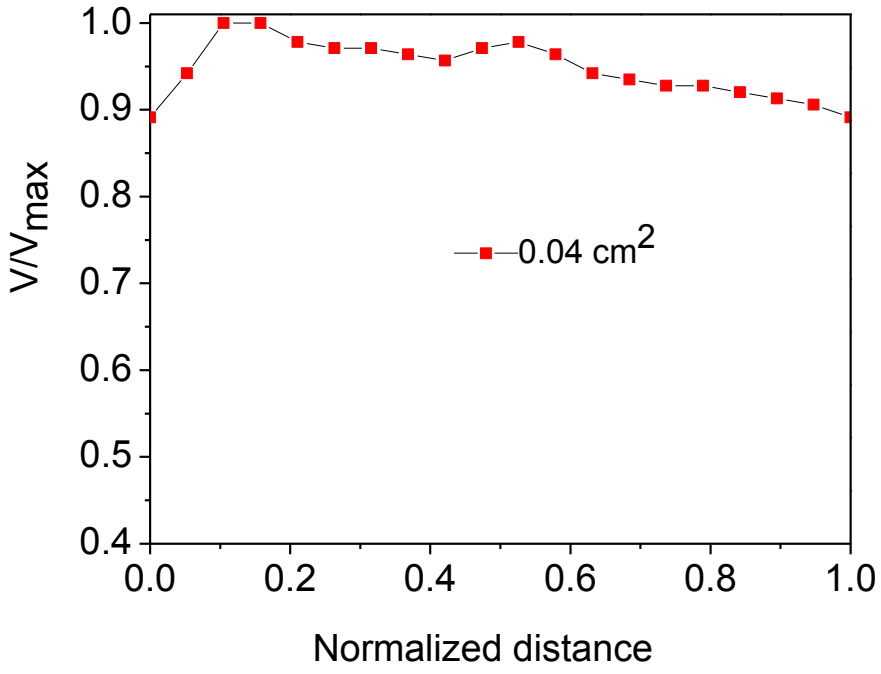

Figure 4.3.8 Normalized photovoltage profile for a 0.04 cm^2 DSC fabricated from P25 nanoparticles and filled with a quasi-solid state electrolyte.

Interestingly, no significant variation in the photopotential was observed in this case. These results show that preferential dye leaching into the liquid electrolyte from the edges of the photoanode has a significant effect when cells of small areas are prepared for metal oxide systems that do not show strong dye absorption. In the case of anatase nanoparticles strong binding of the dye to the nanoparticle surface could result in minimal

desorption of the dye from the edges and hence no variation in the photopotential profiles is observed. Non-uniformity in photopotential distribution can exist for cells with larger cell areas (~ 1 cm^2) for nanoparticle or nanowire electrodes that show low dye absorption and this can affect the recombination rate and the overall cell efficiency. Photopotential distribution along the lateral dimensions of the cell can be used as diagnostic tool to decide if edge effects are predominant for a DSC of a given area. Furthermore, studying the causes of lateral inhomegenity and edge effects would be of considerable importance for designing large DSSCs panels, especially when considering the design of current collectors at the edges. These edge effects should be considered when recombination, transport properties and efficiencies of new systems are reported.

4.4 Summary

In this chapter, fundamental studies involving measurement of electron transport times and electron recombination times in nanoparticle, nanowires and nanoparticle-nanowire hybrid architectures were performed. Especially, the trends in electron transport and recombination time scales with the conventional iodide redox couple having slow recombination kinetics and alternate redox couples having much faster redox couples are compared and the reasons for the observed differences are explained. Further, the macroscale effects arising for the change in the lateral dimensions of the electrode are investigated.

CHAPTER 5

HYBRID NANOWIRE-NANOPARTICLE ARCHITECTURES FOR DYE-SENSITIZED SOLAR CELLS

5.1 Introduction

Rapid improvements in the efficiency and durability of dye-sensitized solar cells (DSCs) are being made by looking at alternatives to the conventional DSC components – the iodide-triiodide redox electrolyte, the ruthenium based N-719 dye and the titania nanoparticle electrode. There has been a significant effort in improving the electrode materials for faster electron transport, designing dye molecules to improve the optical absorption and investigating new redox chemistries for improving the voltage.[123],[124] In particular, replacing the iodide redox electrolyte is of prime importance because of its highly corrosive nature, huge driving force required for dye regeneration and resulting loss in open-circuit voltage, loss of I_2 due to its high vapor pressure and competition for visible light absorption between the triiodide and the dye. Hence, there has been renewed interest in studying iodide-free redox electrolytes for DSCs that overcome all the shortcomings of the iodide electrolyte.[15, 16, 21, 26, 37, 124-129]

Among the different electrolytes being studied, one-electron redox electrolytes have garnered significant interest as they have a more positive redox potential, lower barrier for dye regeneration than I^-/I_3^- couple and can therefore yield higher open circuit voltages. The large scale availability and low cost of these electrolytes also makes them an attractive choice of electrolytes in DSCs. Despite these numerous advantages, the

major challenge with this class of electrolytes is to design electrode materials to slow down the fast electron recombination kinetics with the electrolyte. To circumvent these challenges, approaches for improving the DSC performance with one-electron redox couples have been focused on surface modification of semiconductors with barrier layers and on designing new dyes.

While most of the efforts to improve the performance of DSCs with alternate redox electrolytes have been heavily focused on designing new dyes little attention has been paid to designing semiconductor architectures for improved electron collection. Our previous studies have shown that one can manipulate the transport and recombination characteristics by using tin oxide nanowire based architectures with an iodide redox electrolyte.[130]The question remains if using such nanowire based architectures with modified electron transport and semiconductor-electrolyte interface properties would yield any performance improvement of DSCs using alternate redox couples. To address this question, the performance of DSCs fabricated with different nanowire based architectures with one-electron redox electrolytes is investigated in this work.

In addition to the semiconductor properties, the dye also plays a dominant role in determining the performance of alternate redox electrolytes. To separate the influence of the dye from the semiconductor electrode on the performance gains, here, we studied the photovoltaic characteristics of tin oxide nanowire based architectures sensitized with the conventional N-719 dye. Particularly, the fundamental questions about the effects of surface traps and their passivation when different electrode architectures are addressed. The performance of the following two iodide-free, one-redox couples has been investigated in this study- (a) ferrocene/ferrocenium (b) TEMPO (2, 2, 6, 6-

Tetramethyl-1-piperidinyl oxy radical).The photovoltaic characteristics and electron dynamics with different material architectures involving nanoparticles, nanowires, nanoparticle-nanowire hybrids are investigated to gain fundamental insights into the underlying factors governing the performance.

5.2. Experimental

The titania nanoparticle films are prepared using a paste (18 NRT paste from Dyesol, Australia). For preparing the nanowire pastes Terpineol (Sigma Aldrich) is used as the solvent, and ethyl cellulose (Sigma Aldrich) is employed as a binder. The synthesis of tin oxide and the fabrication of tin oxide nanowire paste is described elsewhere[130].The synthesis of rutile titania nanowires is carried out by a solvo-plasma technique described in detail earlier.[100] In brief, the potassium chloride powder is uniformly spread onto a titanium foil and exposed to an atmospheric microwave plasma flame for 5 minutes to form potassium titanate nanowires. An air flow rate of 8 lpm and a plasma power of 900 W are used. The as-synthesized potassium titanate nanowires are washed with deionized water several times and dipped in 1 M HCl to make hydrogen titanate. The hydrogen titanate nanowires are exposed to a high power plasma (~ 1000 W, 8 lpm air) to form rutile titania nanowires. The rutile titania nanowires are scraped off the foil and a nanowire paste is prepared in a similar fashion as that of tin oxide nanowires.

Photoanodes are prepared by doctor blading the paste using an adhesive tape as the spacer (Scotch Magic^{TM} Tape, thickness = 50 μm). Subsequently, the spacer is removed and the electrodes are sintered at 500 °C for 1h. These electrodes are then cooled to 60

°C and are immersed in a 0.5 mM solution of N-719 dye (Dyesol, Australia) solution in ethanol for ~20 h. To fabricate hybrid architectures, the nanowire electrodes are immersed in colloidal solutions (2% by wt.) of the appropriate nanoparticles (tin oxide or titania), a bare FTO slide is used as a counter electrode and a potential of 5 V is applied for 15s. The tin oxide nanoparticle dispersions are made by dispersing nanopowder (Nano Arc tin oxide from Alpha Aesar) in ethanol using Triton X as the surfactant. Anatase titania colloidal solution is obtained from Optical Dynamics, Louisville, KY. The counter electrode for the cells is prepared by a brush deposition of a platinum counter electrode solution (Dyesol, Australia) on the FTO glass and heating the electrode to 420 °C for 20 min and subsequently cooling it down to room temperature. The cells are fabricated by sandwiching the photoanode and the counter electrode with a 25 microns thick Surlyn film (Dyesol, Australia) and followed by aging at 100 °C for 5 min.

The ferrocene electrolyte comprised of 0.05 M ferrocenium hexaflourophosphate, 0.1 M Ferrocenium, 0.01 M chenodeoxycholic acid and 0.5 M *tert*-butylpyridine in acetonitrile. The ferrocene redox couple is left to age in air for 24 h prior to use. The TEMPO electrolyte comprised of 1M TEMPO (2, 2, 6, 6-Tetramethyl-1-piperidinyl oxy radical), 0.5 M N-Butylbenzimidazole and 0.16 M $NOBF_4$in acetonitrile.

The redox electrolyte is infiltrated into the DSC using vacuum backfilling through the holes drilled into the counter electrode prior to the platinum coating. The DSCs are illuminated using a Xenon lamp of a 150 W solar simulator (New Port Model96000) equipped with an Air Mass 1.5 filter. All electrochemical measurements were performed using a potentiostat (EG&G-PAR 273A). The light intensity incident on the

cells is adjusted to 100 mW/cm^2 using a silicon power meter (ThorlabsS120UV). For the current decay measurements the light from the solar simulator (100 mW/cm^2)is used as the bias light and a light pulse from a diode laser (~550 nm) is used as the perturbation light. The time constant is determined by an exponential fit to the photocurrent decay[131]. The electron lifetimes are determined using the open-circuit voltage decay technique described by Bisquert and co-workers[132].

5.3. Results and Discussion

The performance of bare tin oxide nanowires and titania particles, without any barrier layers using the ferrocene-ferrocenium redox electrolyte is shown in Figure 5.1. The current-voltage (J-V) characteristics for DSCs made with tin oxide nanowires exhibit several orders of magnitude higher short- circuit current density (J_{sc}) of 1.8 mA/cm^2 than those fabricated with titania nanoparticles (few tens of μA/cm^2). The highest reported J_{sc} for un-modified electrodes sensitized with the N-719 dye is only 0.1 mA/cm^2 which is substantially lower than that obtained with tin oxide nanowires.

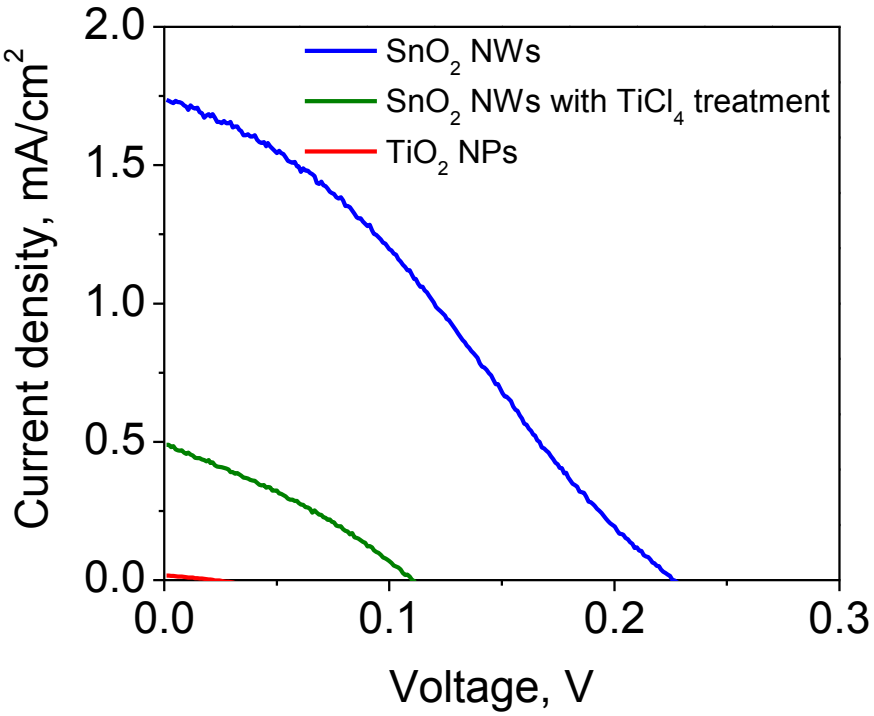

Figure 5.1. J-V characteristics of SnO_2NWs, TiO_2 NPs and $TiCl_4$ treated SnO_2 NWs using ferrocene redox couple at 1 Sun illumination.

In an effort to boost the J_{sc} a thin layer of titania was deposited onto the nanowires using a $TiCl_4$ treatment; however, this resulted in a lowered J_{sc}. This is in contrast to the increased performance when an iodide electrolyte was used.[130] The unpassivated surface traps on titania obtained from $TiCl_4$ treatment could be responsible for lowering the performance when using ferrocene-ferrocenium redox electrolyte. The enhanced performance with tin oxide nanowires can be explained by considering the surface properties, electron transport and recombination characteristics of tin oxide nanowires and titania nanoparticles. Prior attempts to improve the open-circuit voltages with tin oxide NPs and iodide redox electrolyte used submonolayers of alumina to passivate surface trap states.[31] In contrast, such high performance can be obtained from tin oxide nanowires and iodide redox electrolyte,

without any surface passivation, also indicating lower trap state density on tin oxide nanowire surface.[121] Analysis of the dark current at the same potential (Figure 5.2) shows that tin oxide NW DSCs exhibit lower dark currents with the ferrocene-ferrocenium redox couple compared to titania nanoparticles, indicating lower recombination rates with tin oxide nanowires. Thus, the lowered surface trap site density coupled with fast charge transport properties of tin oxide nanowires allowed for efficient electron collection and higher short-circuit current densities to be attained.

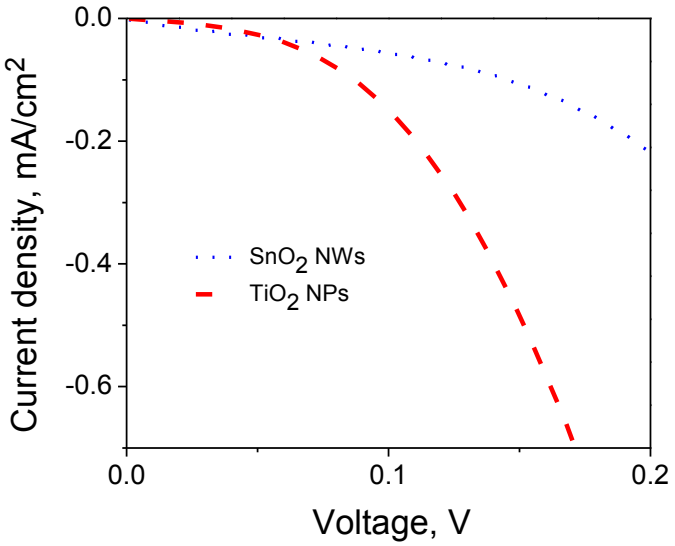

Figure 5.2. Dark J-V curves of DSCs tin oxide nanowires, titania nanoparticles and ferrocene-ferrocenium redox couple.

The open-circuit voltage (V_{oc}) for the tin oxide nanowire DSCs employing the ferrocene-ferrocene redox couple was about 250 mV, but was orders of magnitude higher than that of titania NP DSCs which only exhibited a few tens of mV. In comparison, Hanmann and co-workers reported that titania nanoparticles passivated with a one cycle ALD of Al_2O_3, showed an V_{oc} of 500 mV and a J_{sc} of 1 mA/cm^2.[128] These results clearly demonstrate the excellent suitability of tin oxide nanowires in

DSCs employing redox couples with fast recombination kinetics. As shown in Figure 5.5, the conduction band edge of tin oxide is located 400 mV lower than the conduction band edge of titania, resulting in a lower Fermi level in tin oxide. Hence, a lower V_{oc} is theoretically expected with tin oxide when compared with titania. Further, low dye adsorption onto nanowires compared with nanoparticles could lower the Fermi level of tin oxide nanowires and result in a lower V_{oc} than titania nanoparticles.

The higher electron diffusion coefficient (D) along with higher electron lifetimes (τ) for tin oxide nanowires results in higher diffusion lengths (L) according to the relation $L = \sqrt{D \cdot \tau}$. Figure 5.3 shows the J-V characteristics of DSC fabricated with tin oxide NW films of different thickness using the ferrocene-ferrocenium redox couple. An increase in the J_{sc} is observed with increasing film thickness up to 15 microns indicating higher diffusion lengths in tin oxide nanowires. The films thicker than 15 microns had poor mechanical stability resulting in delamination. Current state-of-the-art DSCs using these redox electrolytes comprise of a few microns (1-2 μm) thick TiO_2 nanoparticle film sensitized with a high extinction coefficient dye.

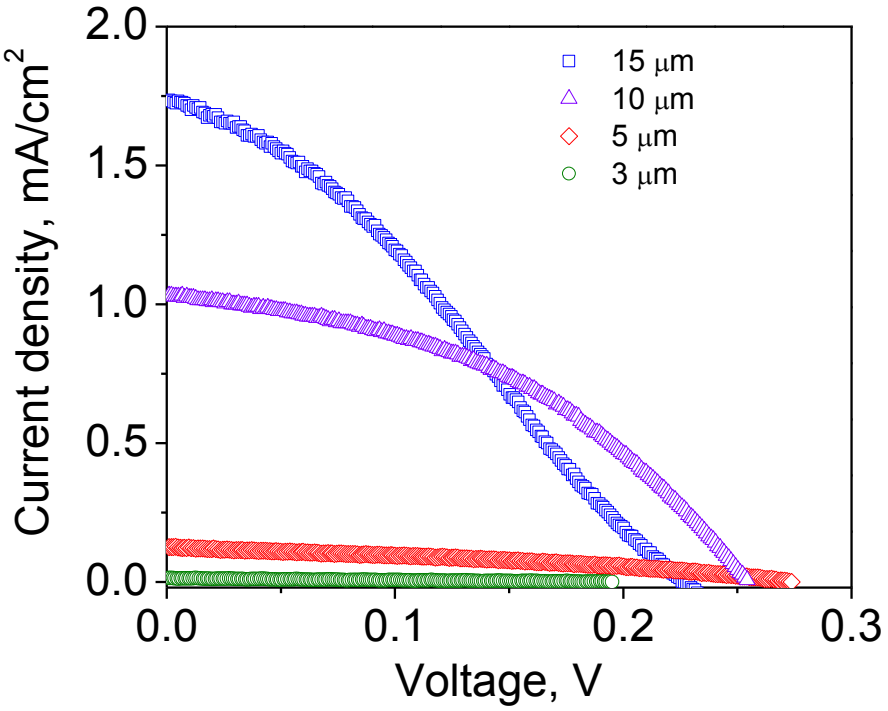

Figure 5.3. J–V curves of DSCs employing ferrocene redox couple with different film thickness of tin oxide NWs

The reduced titania film thickness compared to the conventional DSCs (10-15 μm) lowers the recombination losses and allows for efficient charge carrier collection. As a result of the reduced film thickness, the J_{sc} and hence the efficiencies that can be achieved with one electron redox couples such as ferrocene/ferrocenium and TEMPO have been twice as low as the best performing redox electrolytes. The efficiency with these redox couples is still not on par with the efficiency of DSCs employing the iodide redox electrolyte. Further improvement in efficiency is only possible by finding ways to increase J_{sc}. Increasing the film thickness to improve the electron concentration in films is not possible with the conventional titania nanoparticles due to the low electron diffusion length when kinetically fast redox couples are used. The use of tin oxide

nanowires which exhibit higher diffusion lengths could potentially overcome the bottle-neck in the achievement of higher J_{sc} with one-electron redox couples.

DSCs fabricated with unpassivated tin oxide nanowires and TEMPO redox couple exhibited very low performance. J-V characteristics with the TEMPO redox electrolyte also show a similar trend compared to the ferrocene redox electrolyte, where the tin oxide nanowires outperform titania nanoparticles (Figure 5.4). However, the J_{sc} and V_{oc} obtained were very low (few $\mu A/cm^2$ and few tens of mV) indicating much faster recombination kinetics of the TEMPO redox electrolyte when compared with that of ferrocene.

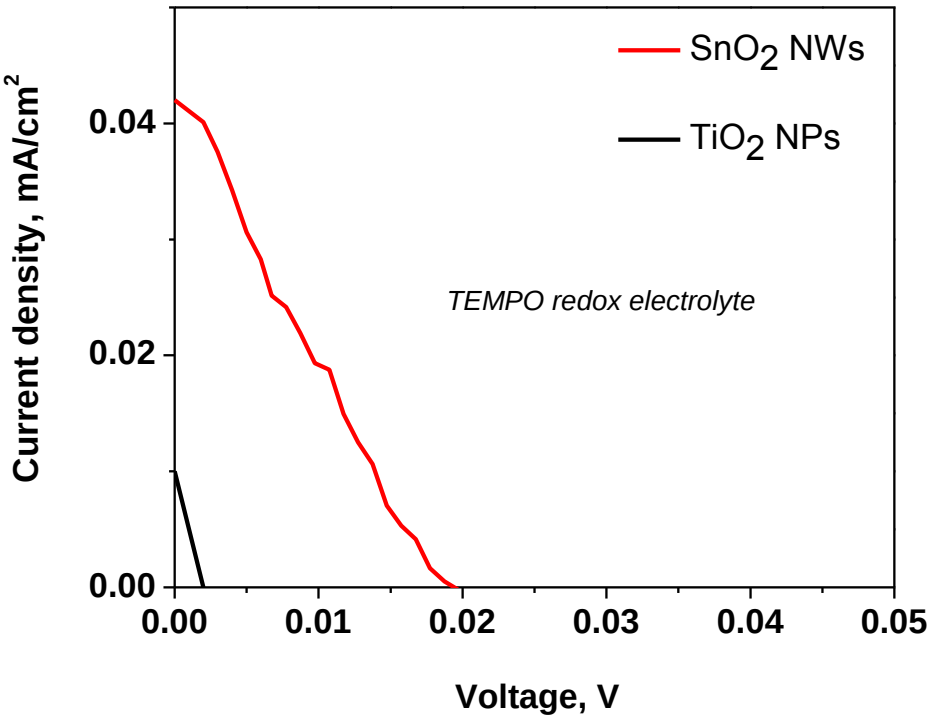

Figure 5.4. J-V curve comparing the performance of unpassivated SnO_2 NWs and TiO_2 NPs under 1 Sun illumination.

In order to increase dye adsorption and the open-circuit voltage with tin oxide nanowires based DSCs, anatase nanoparticles were coated onto tin oxide nanowires to form hybrid architectures. These hybrid architectures were subsequently coated with a single layer of alumina by atomic layer deposition to passivate the trap states on the titania surface. In previous studies, atomic layer deposition (ALD) was used primarily to produce titania shells.[133, 134] But, a major shortcoming of this approach is that the amorphous titania shells formed from atomic layer deposition tend to exhibit a high resistance of 1-10 GΩs with poor charge transport properties leading to reduced current densities.[133] Similarly, tin oxide nanowires coated with a shell of titania by ALD and subsequently passivated with a submonolayer of alumina did not result in any performance improvement over titania nanoparticles due to the high resistivity of the titania layer. Here, we used an electrophoretic deposition technique to coat the tin oxide nanowires with anatase TiO_2 nanoparticles (~ 10 nm diameter). The upward shift in the quasi-Fermi level of titania coated tin oxide nanowires after equilibration and increased dye loading is expected to yield open-circuit voltages higher than tin oxide nanowires alone. The band edge locations of tin oxide, titania and the different redox couples used in this work are shown in Figure 5.5.

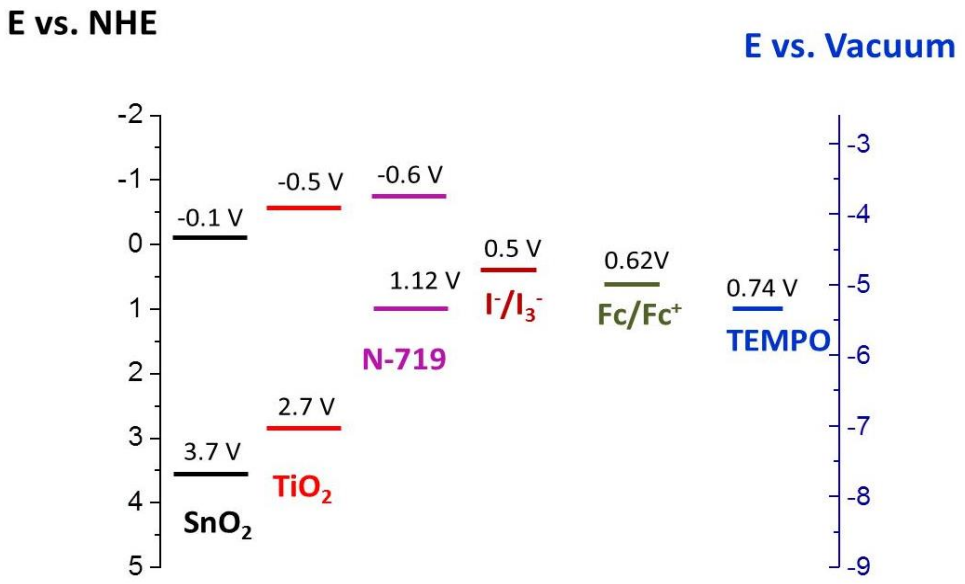

Figure 5.5 Band edge location of tin oxide, titania, conventionally used N-719 Ru based dye, ferrocene and TEMPO redox electrolytes.

Figure 5.6a depicts the schematic showing the titania nanoparticles coated tin oxide nanowire arrays for the electrode structure used in this work. The scanning electron microscopy images of the hybrid architectures (Figure 5.6b, 5.6c) illustrate that the

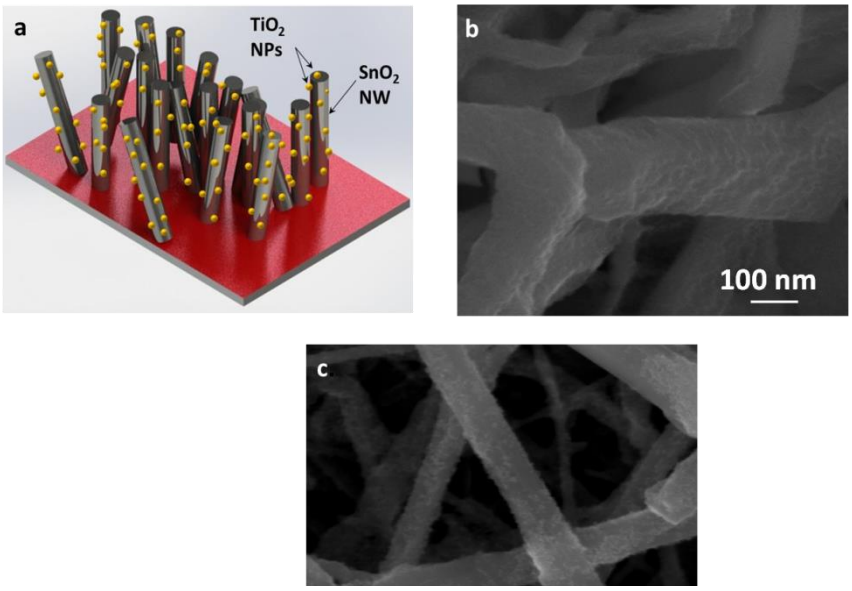

Figure 5.6. (a) Schematic showing the structure of SnO_2 NW/TiO_2 NP Hybrid architecture (b) SEM image of SnO_2 NWs/TiO_2 NP Hybrid architecture (c) SEM image of TiO_2 NW/TiO_2 NP Hybrid architectures

anatase nanoparticles are uniformly coated on the nanowires.

Figure 5.7 shows transmission electron microscopy (TEM) images of titania nanoparticle-tin oxide nanowire hybrid architectures. The TEM images reveal that crystalline titania nanoparticles are uniformly coated onto the tin oxide nanowires.

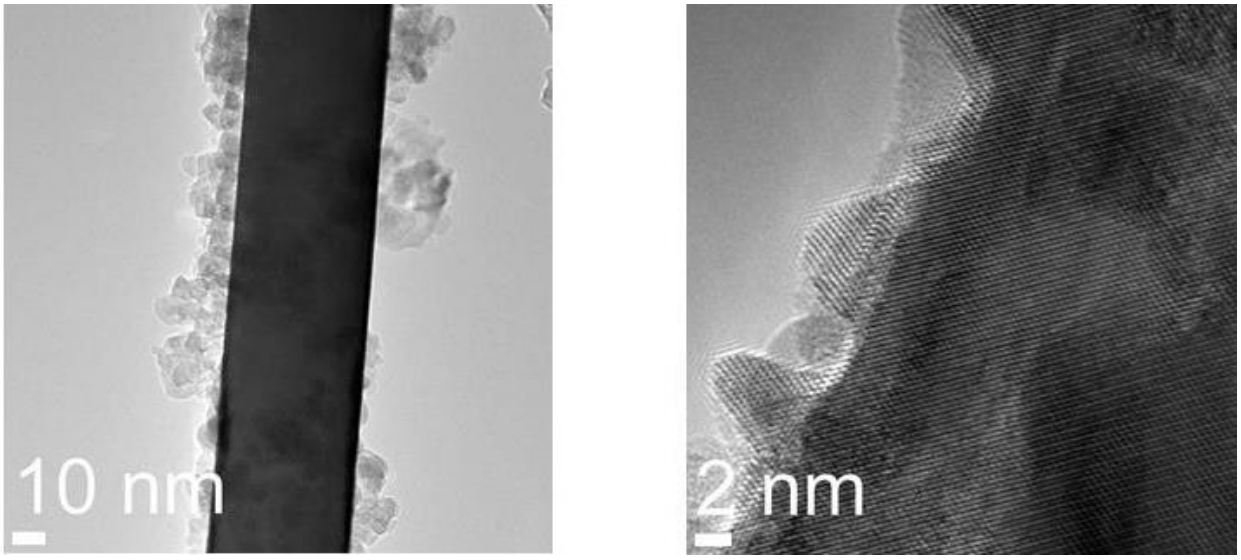

Figure 5.7. Transmission electron microscopy images of TiO_2 nanoparticle-SnO_2 nanowire hybrid architectures.

The J-V characteristics of alumina coated titania nanoparticles and alumina coated titania nanoparticle-tin oxide nanowire hybrid architecture are compared in Figure 5.8.

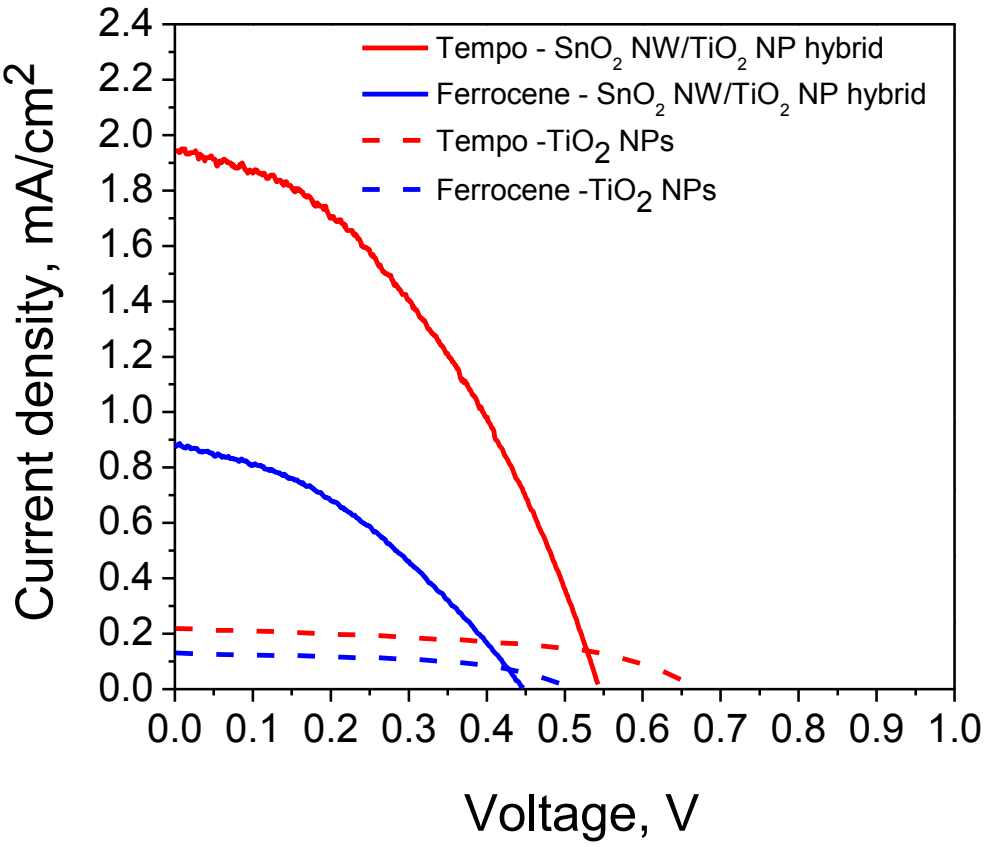

Figure 5.8 Current- voltage characteristics of the TiO_2 NP/SnO_2 NW hybrid architecture and TiO_2 NP based DSCs with ferrocene and the tempo redox electrolytes

DSCs fabricated with hybrid architectures show about ten times higher J_{sc} than the conventional DSCs employing titania nanoparticle films of the same thickness (~ 10 μm). The V_{oc} observed with the hybrid architectures are slightly lower than those observed with titania nanoparticles alone. This is due to the lowering of the quasi-Fermi level after equilibration of the Fermi level of titania and tin oxide. Interestingly, tin oxide nanowire-titania nanoparticle hybrids show a significant improvement in J_{sc}, regardless of slightly lowered electron lifetimes. These results highlight that faster electron transport and low density of surface trap states are key factors in achieving

higher current densities when using alternate redox couples with faster recombination kinetics.

DSCs based on different architectures such as nanoparticles, nanowires, and nanowire-nanoparticle hybrids of tin oxide and titania are J-V characteristics of all these are compared in Figure 5.9 to understand the role of different factors on improving the photovoltaic performance. All these electrodes were coated with 1 cycle of alumina prior to dye adsorption to passivate surface traps on the semiconductor. Among these, rutile titania nanowire-anatase nanoparticle hybrids exhibit the highest V_{oc} of 730 mV (for TEMPO redox electrolyte) due to high electron lifetimes.

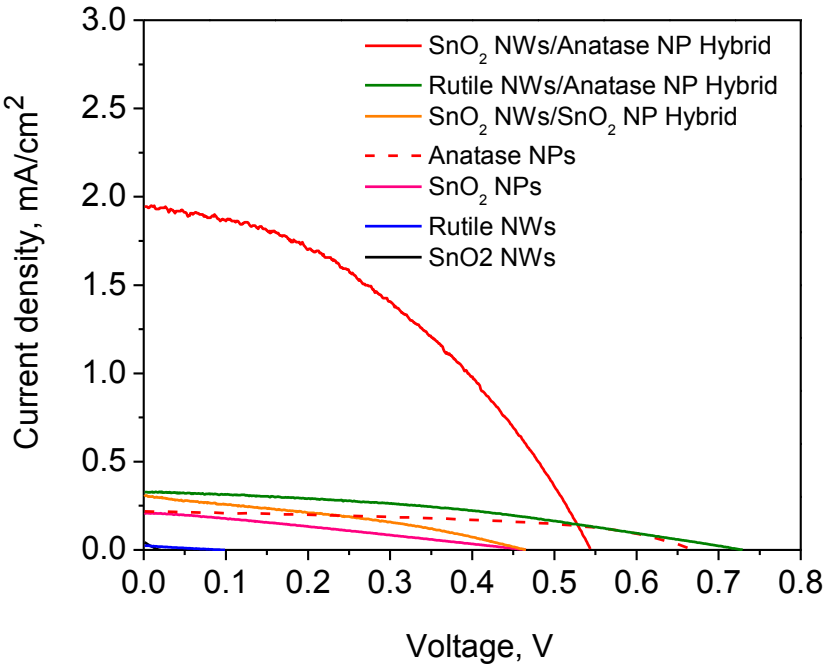

Figure 5.9. J-V curves for different architectures coated with 1 cycle of Al_2O_3 when using TEMPO redox electrolyte.

On the other hand, the tin oxide nanowire- anatase nanoparticle hybrids exhibit the highest J_{sc} due to the fast electron transport in tin oxide nanowires and good dye adsorption and fast electron injection into titania nanoparticles. The electron transport in titania nanowires is similar to that of titania nanoparticles and this limits high current densities from being achieved. The presence of higher number of Ti^{+3} trap states has been shown to be responsible for the slow charge transport in 1-D titania nanostructures.[100] Therefore, having single crystalline nanowires of titania does not necessarily improve electron transport.[35] This explains why the short-circuit current densities obtained with titania nanowire based architectures are not as high as in tin oxide nanowires. Further, the band edge alignment of tin oxide and titania allow enhanced electron collection in case of tin oxide nanowire coated with titania. The conduction band edge of titania is about 200 meV higher than rutile titania.[135] This band offset contributes to improved charge collection and slightly higher current densities of titania nanoparticle-nanowire hybrids when compared with titania nanoparticles. It is interesting to note that the hybrid architectures fabricated with nanowires exhibit high short-circuit current densities even though they possess lower surface area for dye adsorption than nanoparticles (Figure 5.10).

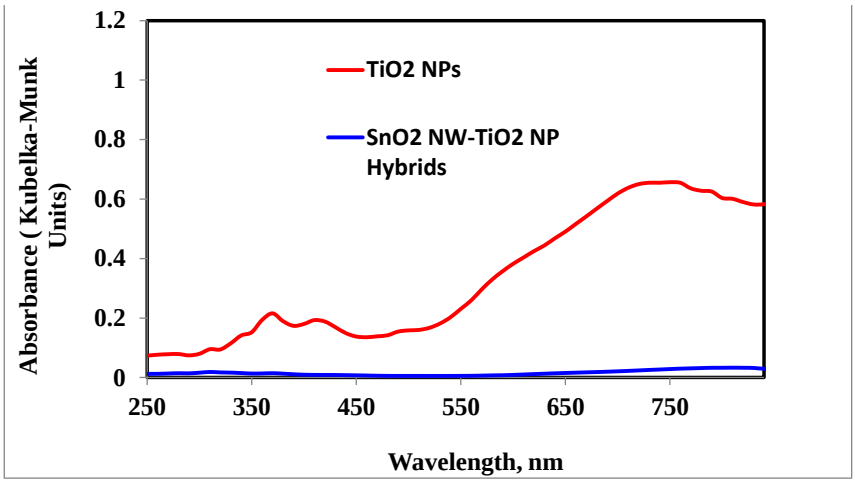

b

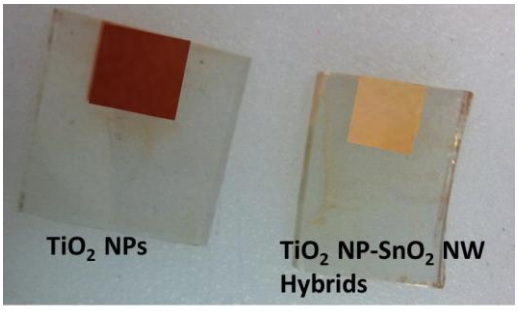

Figure 5.10. (a) Comparison of absorbance spectrum of the N-719 sensitized TiO_2 NPs and TiO_2 NP-SnO_2 NW Hybrids (b) picture showing TiO_2 NPs and TiO_2 NP-SnO_2 NW Hybrids after sensitization with N-719 dye.

In addition to improving dye adsorption, another key aspect for enhancing the performance is to select a sensitizer that can be efficiently regenerated by the redox couple. Figure 5.11 shows the power conversion efficiencies vs. the thermodynamic driving force for the commercial Ru based dyes and new organic dyes for different redox couples summarized in Figure 2.2 of Chapter 2. For the organic dyes, a driving force of about 0.3 eV is the optimized driving force (-Δ G) for achieving high efficiencies and is consistent with literature reports.[136] Analysis of literature data on commercial Ru based dyes shows that they need a much higher driving about 0.6 eV for efficient dye regeneration when

compared with organic dyes indicating that inefficient dye regeneration is a shortcoming of using N-719 dye with alternate redox electrolytes. According to Marcus theory, electron transfer rate is maximum at $-\Delta G=\lambda$, where λ is the reorganization energy. Hence, the driving force corresponding to the maximum efficiency could be taken as a measure of the reorganization energy.[137] These reported values of λ are consistent with the $-\Delta G$ corresponding to maximum efficiency in Figure 5.11

For an N-719 dye with an absorption onset of 780 nm (1.6 eV), the maximum theoretical efficiency would been estimated to be around 18 % for a 0.3 eV loss-in potential and around 11 % for 0.6 eV loss-in potential. The design of a sensitizer with a lower band gap and a lower loss-in potential is crucial for improving the DSC efficiency.

The insights gained from this work can also be extended to solid state electrolytes. For instance the recombination time scale for spiro-OMeTAD has been shown to be at least two orders of magnitude greater than liquid electrolytes.[138] The hybrid architectures of tin oxide nanowires, with high electron diffusion lengths, would be of high importance to gain performance improvements for such solid state electrolytes. Future work is also focused on using new sensitizers in conjunction with the hybrid architectures developed in this work to obtain higher efficiencies.

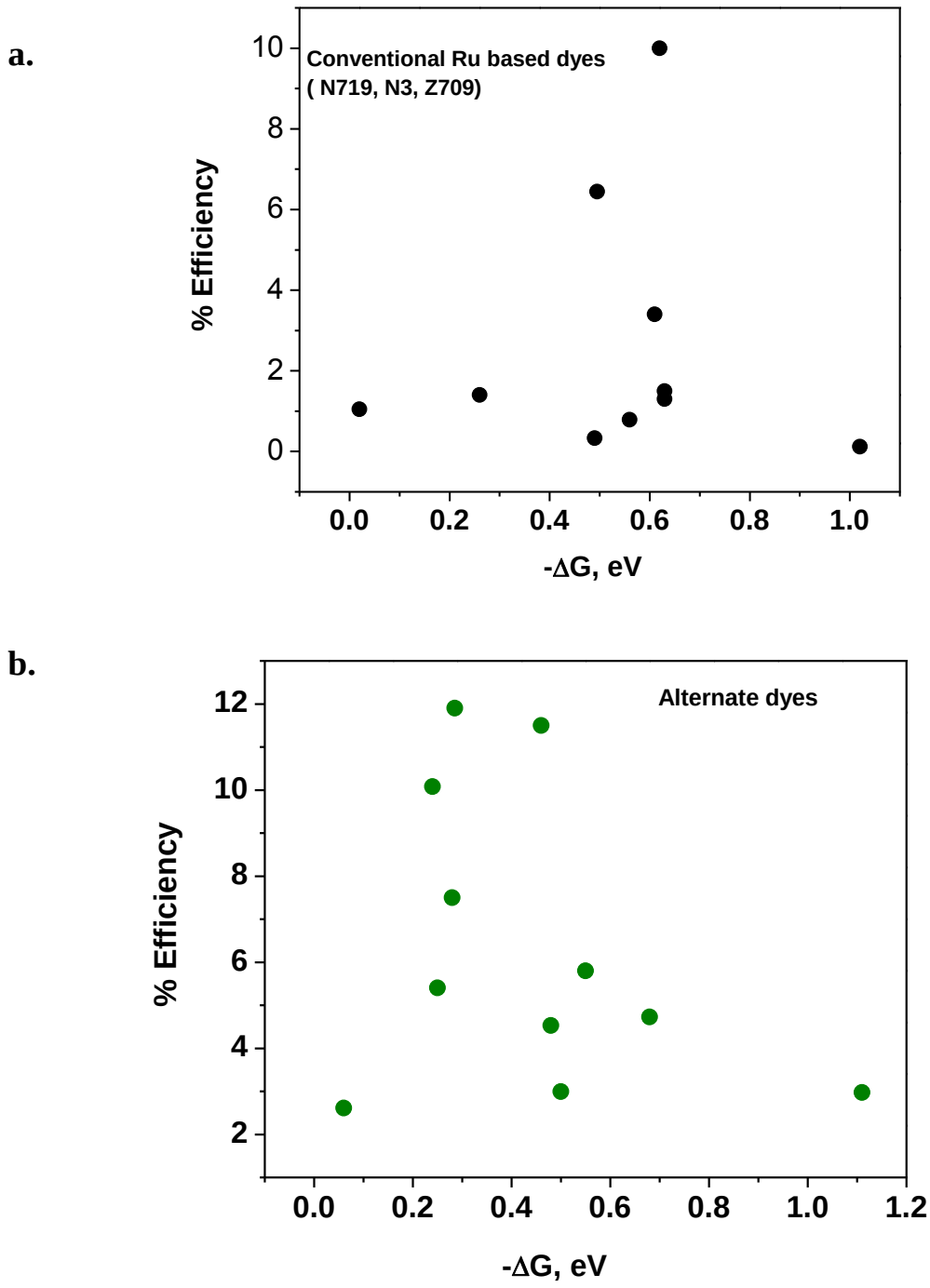

Figure 5.11. Power conversion efficiency vs. thermodynamic driving force for dye-regeneration for (a) conventional Ru based dye and (b) alternate dyes (organic) plotted from literature.

5.4 Summary

The photoanodes fabricated with tin oxide NWs and tin oxide nanowires- anatase titania nanoparticle hybrids are promising for attaining high performance with alternate redox couples. Improved electron transport properties of tin oxide nanowire based architectures enabled significantly higher current densities with various iodide free redox couples. Alumina deposition by atomic layer deposition provided better passivation of surface trap states on titania surface than the tin oxide surface. Hybrid architectures of anatase titania NPs coated on rutile titania NWs showed the highest electron lifetimes due to better surface passivation by alumina. However, these hybrid architectures show short-circuit current densities similar to nanoparticle based architectures due to poor electron transport properties of single crystal titania nanowires. In comparison with new organic dyes, commercially available Ru based dyes require a huge driving force for efficient dye regeneration and result in lowered performance. The use of thick tin oxide nanowire electrodes in conjunction with a sensitizer that can be regenerated efficiently is identified as the route to obtain higher performance with alternate redox electrolytes. Lowering the reorganization energy of the sensitizer plays a dominant role in lowering the potential losses associated with dye regeneration and attaining higher power conversion efficiency.

CHAPTER 6

MOSITURE RESISTANT ELECTRODE ARCHITECTURES FOR METHYL AMMONIUM LEAD IODIDE PEROVSKITE SOLAR CELLS

6.1 Introduction

In this chapter, a novel approach for protecting methyl ammonium lead iodide perovskite crystals against moisture has been developed. An ideal protective coating encapsulating the perovskite should not only be impermeable to moisture and oxygen, but also exhibit good hole and electron transport properties. Studies on lead free organic-inorganic halide perovskites such methyl ammonium tin iodide also reported that these materials are both oxygen and moisture sensitive.[139] Hence, oxygen impermeability is also a critical factor that needs to be considered when designing a protective coating for the perovskites. Composites comprising of layered silicates or clays dispersed in a polymeric matrix have been extensively investigated as barrier materials for oxygen and water. The moisture resistance in these composites arises because of the increase in tortuosity of the path of the molecule diffusing through the coating.[140, 141] By rationale design of the components of the composite, a moisture and oxygen resistant yet highly conductive coating can be developed. When a polymeric composite is used as a protective coating, it is essential to have higher thickness to increase the tortuosity in the path of gas and water molecules. Hence, it becomes important to choose components that have high electron and hole conductivity besides having good barrier properties to gases and water, so that the thickness of the coating does not impact the photovoltaic performance. Defect free multilayer graphene has been demonstrated to be impermeable to moisture and many

gases due to small inter layer spacing.[142] Further, submicron thick films of highly reduced graphene oxide have demonstrated two orders of magnitude higher moisture impermeability when compared to aluminized polyethylene terephthalate used as an industrial standard.[142] The excellent gas and moisture barrier properties of graphene combined with its high electrical conductivity makes it a suitable dispersive material in the composite. The use of graphene with a conductive polymer having excellent hole transport properties can act as a good protective coating for the perovskite. The concept is schematically illustrated in Figure 6.1.

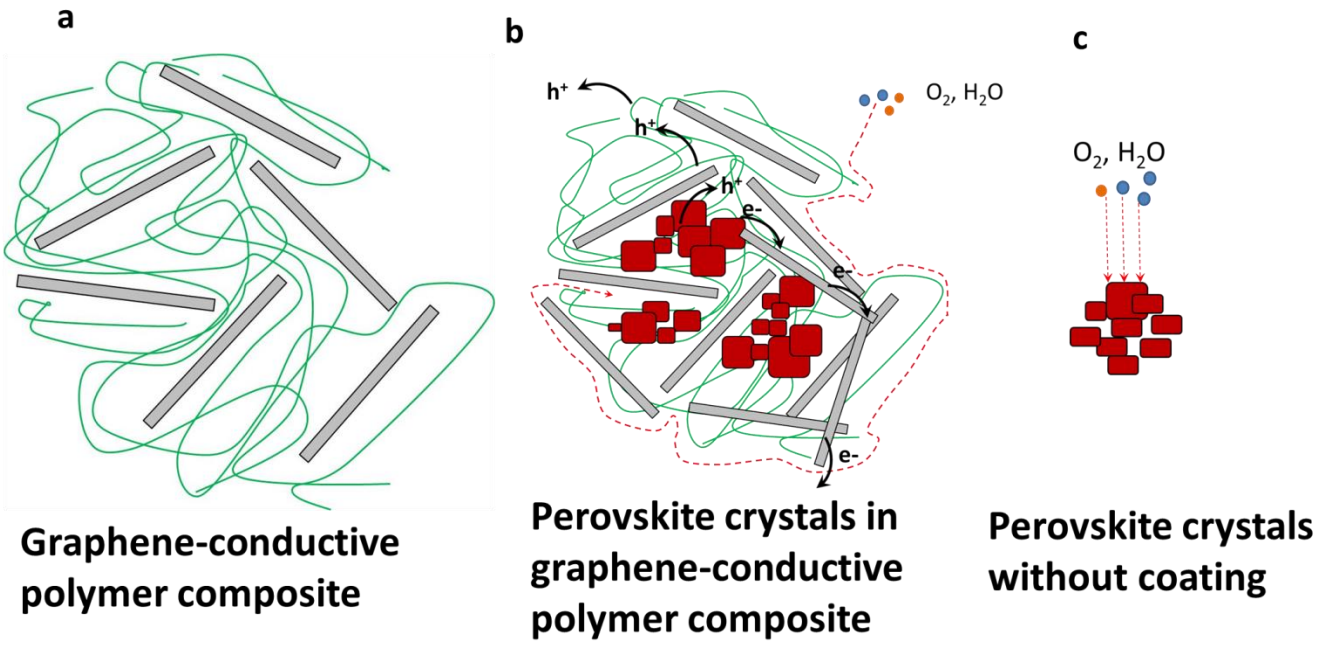

Figure 6.1.Schematic illustrating the role of graphene/conductive polymer composite as a multifunctional coating that protects the perovskite crystals from moisture while stilling allowing efficient electron and hole transport through encapsulated layer - (a) shows the graphene-conductive polymer composite (b) illustrates the tortuous path of oxygen and water molecules to reach the perovskite encapsulated in the graphene/conductive polymer composite, and efficient electron transport through graphene and hole transport through

hole conductive polymer (c) short transport path of water and air molecules towards unprotected perovskite crystals.

Graphene/polymer composites are being investigated for wide range applications. In particular, graphene/polyaniline (PANI) composites have been widely researched for supercapacitors,[143] sensing platforms,[144] fuel cells,[145, 146] and solar cells,[147] due to their improved conductivity (10 Scm^{-1}) and specific capacitance (531 F g^{-1}) as compared to 2 S cm^{-1} and 216 F g^{-1} of pure PANI.[148, 149] In addition, PANI has been used widely used a hole transport material in DSCs.[77, 150] In this work, graphene/ PANI composites are used as a protective coating in perovskite solar cells utilizing copper iodide (CuI) as a hole transport material (HTM). The high electrical conductivity of the graphene/ PANI composites can enable the use of a thick coating creating a moisture resistant seal around the perovskite while maintaining the photovoltaic performance.

6.2 Experimental

Substrate preparation. Fluorine doped tin oxide (FTO) coated substrates (Hartford glass, USA) are etched using zinc metal powder and 2 M hydrochloric acid. The etched substrates are cleaned by ultra-sonication in an alkaline, aqueous washing solution, rinsed with deionized water, and ethanol and subjected to oxygen plasma (PLAMAX 150S) treatment for 15 min.

$CH_3NH_3PbI_3$ synthesis and device fabrication To deposit the TiO_2 compact layer, titanium diisopropoxide bis-acetylacetonate (TAA) is dissolved in 1-butanaol and 0.15 M and 0.3 M solutions of TAA are prepared. The 0.15 M and 0.3 M (three times) TAA solutions are spin coated on the FTO substrates at 4000 rpm for 30s followed by heating

the substrates at 500 °C for 30 min. After cooling to room temperature, the substrates are immersed in a 40 mM aqueous solution of $TiCl_4$ for 30 min at 70 °C, rinsed with deionized water and heated at 500 °C for 30 min. The mesoporous TiO_2 layer is deposited by spin coating a commercial TiO_2 paste (Dyesol-18NRT, Dyesol) diluted in ethanol (1:3.5, weight ratio) at 5000 rpm for 30 s. After drying at 125 °C, the TiO_2 films are gradually heated to 500 °C for 30 min and cooled to room temperature and $TiCl_4$ treatment is performed on the substrates. The sequential deposition procedure developed by Gratzel and coworkers is used for the perovskite deposition.[107] The perovskite deposition discussed as follows is performed in an argon glove box, with humidity less than 1%. A 1.3 M solution of PbI_2 in anhydrous *N*,*N*-dimethyl formamide (DMF) is prepared, and was maintained at 70 °C. The mesoporous TiO_2 films are infiltrated with PbI_2 by spin coating the PbI_2 solution at 6500 rpm for 5 s and dried at 70 °C for 30 min. After cooling to room temperature, the film is coated with PbI_2 by the above procedure and the electrode is dried at 70 °C for 30 min. The films are dipped in a solution of CH_3NH_3I in 2-propanol (10 mg/ml) for 60 s, rinsed with 2-propanol and dried at 70 °C for 30 min to form the perovskite.

Protective coating deposition. The protective coating deposition is performed outside the glove box and is detailed as follows. Solutions of graphene and PANI in 2-propanol are alternatively spin coated to form the composite coating. The procedure is repeated several times to build up the thickness of the composite layers. For instance, a 2x coating denotes that the alternate deposition of graphene and PANI was performed twice in an alternate fashion. Graphene flakes (Cheap tubes, USA) dissolved in 2-proponal (1:10, weight ratio) and the samples are dried for 80 °C for 10 min after spin coated at 2000 rpm for 10s. Then

PANI (Aldrich) is dissolved in 2-propanol (2:5, weight ratio) and spin coated at 2000 rpm for 10s followed by drying at 80 °C for 10 min.

Device fabrication. The copper iodide (CuI) used as the hole transport material is deposited by a doctor blade technique.[108] The CuI solution is prepared by dissolving 0.1 M of CuI in dipropylsulfide (Sigma Aldrich). Following the deposition, the substrates dried at 70-80 °C for 20 min after the doctor blading. The device fabrication is carried out under controlled atmospheric conditions and a humidity of <0.2%. Gold is deposited on separate glass plate by RF sputtering at 80 mTorr and 18 mV conditions for 4 min. The sputtered electrodes are mechanically pressed onto the copper iodide coated electrode to sandwich the two electrodes.

Humidity testing. The humidity measurements are done at 99% relative humidity in glove box using a hygrometer (Omega HH314A). The high humidity has been reached by heating the distilled water at constant temperature (~54 °C).

Characterization. XRD patterns of the perovskite samples are obtained with a Bruker D8 diffractometer (with Cu-Kα radiation). The morphological properties of the material are investigated using a scanning electron microscope (FEI NOVA nano-SEM 600). Transmission electron microscopy is performed using a Tecnai F20 FEI TEM equipped with a Gatan 2002 GIF system. The perovskite solar cells are illuminated using a xenon lamp of 150W solar simulator (New port model 96000) equipped with an Air Mass 1.5 filler. All electrochemical measurements are performed using a potentiostat (EG&G-PAR 273A). The light intensity incident on the cells is adjusted to 100 mW cm^{-2} using a silicon power meter (Thorlabs S120UV).

6.3 Results and Discussion

The degradation products of methyl ammonium lead iodide perovskite samples after moisture exposure, with and without the graphene/PANI coatings, are analyzed using X-ray Diffraction (XRD). Figure 6.2a and 6.2b show the time evolution of the XRD patterns of the unprotected perovskite samples exposed to air having 99 % relative humidity.

Figure 6.2. (a), (b) Time evolution of the XRD pattern of unprotected $CH_3NH_3PbI_3$ perovskite sample and different time degradation of $CH_3NH_3PbI_3$ at 99% relative humidity (c) Time evolution of the XRD pattern of Graphene/PANI coated $CH_3NH_3PbI_3$ at 99 % relative humidity. XRD pattern of lead iodide and methyl ammonium iodide are also shown for comparison.

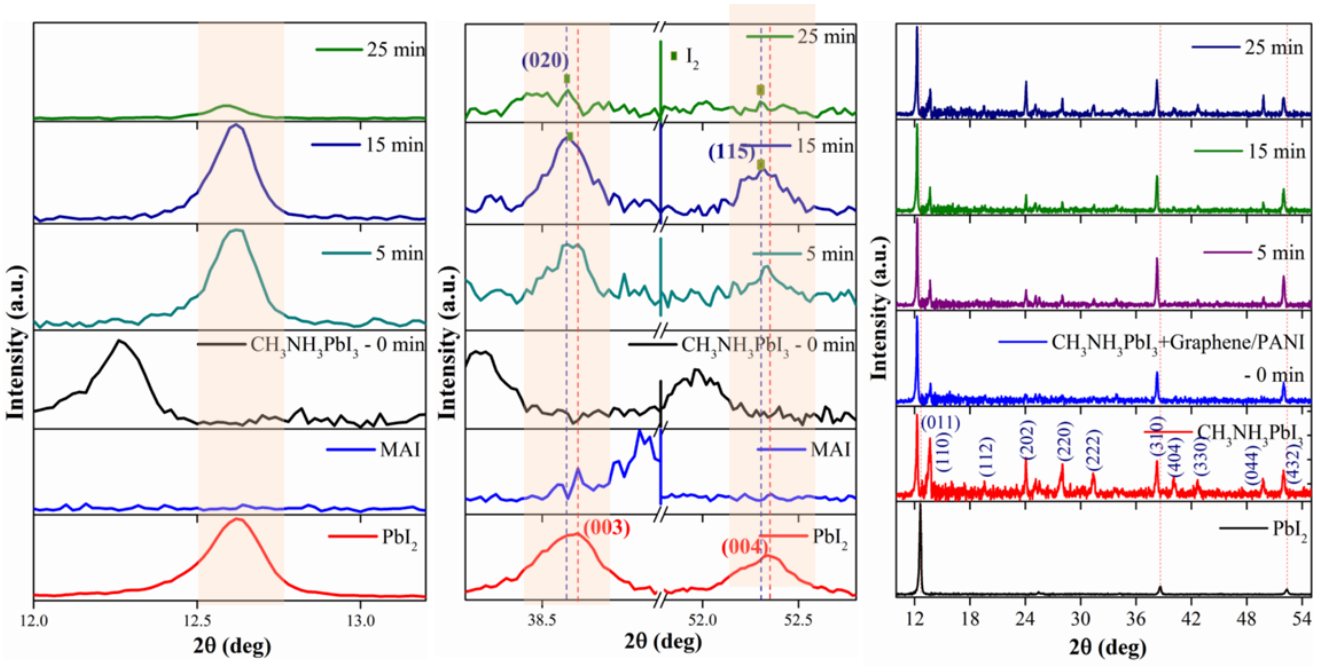

The grain size of the methyl ammonium lead iodide perovskite is 27 nm as calculated from Scherrer formula. All the XRD peaks are indexed to a tetragonal perovskite structure having lattice constants of a=b=8.867 Å and c=12.797 Å and is in agreement with earlier reports. [45, 52, 151, 152] The peak positions of methyl ammonium iodide and lead iodide are also shown for comparison. The intensity of the perovskite peaks decreased with increasing exposure times and the intensity of the lead iodide and iodine were found to start increasing. The peaks at 12.66° and 52.34°can be indexed to (001) and (004) planes of hexagonal lead iodide (JCPDS # 801000). The peak at 38.61°can be assigned to the (020) plane of orthorhombic iodine (JCPDS# 792440). These peaks are not observed in the perovskite samples coated with the graphene/PANI composite (Figure 6.2b), suggesting that composite coating effectively protects the perovskite from degradation against moisture.

The XRD results corroborate the acid-base reaction mechanism proposed for perovskite degradation in the presence of moisture.[55] This mechanism is modeled by the following equation and suggests that in the presence of large quantities of water, the perovskite degrades into the original lead iodide and methyl ammonium iodide.

$$n[(CH_3NH_3^+)PbI_3] \xrightarrow{H_2O} [(CH_3NH_3^+)_{n-1}(CH_3NH_2)_n PbI_3][H_3O] \xrightarrow{H_2O} PbI_2 + HI + CH_3NH_2 + H_2O$$

After moisture exposure, the unprotected perovskite samples turned yellow color while the graphene/PANI perovskite still exhibit the characteristic black color of the perovskite (Figure6.3). The presence of graphene in the composite protective layer acts as an impermeable seal to moisture, preventing this degradation reaction.

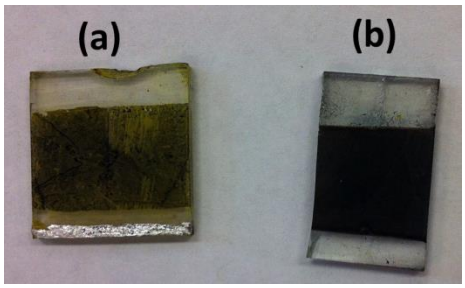

Figure 6.3. Images depicting (a) unprotected perovskite sample and (b) graphene/PANI composite coated perovskite sample, after exposure to air at 99 % humidity for 2h.

To investigate the morphology of graphene/PANI composite on the perovskite crystals, cross-section scanning electron microscopy (SEM) images (Figure 6.4) on the perovskite electrodes and transmission electron microscopy (TEM) images (Figure 6.6) of perovskite crystals were obtained. Cross-section images revealed that the composite coating was infiltrated into the perovskite/TiO_2 region of the solar cells and further formed a thick overlayer at the top. In this work, copper iodide is employed as a hole transport material because of the low cost (two orders of magnitude lower cost than spiro-OMeTAD) and high commercial availability of CuI when compared with spiro-OMeTAD used in the best performing cells reported in literature.[107] In addition, to simplify the fabrication process, gold was sputtered on glass slide and is sandwiched with perovskite electrodes coated with the copper iodide ,as opposed to the conventional route of thermally evaporating gold.

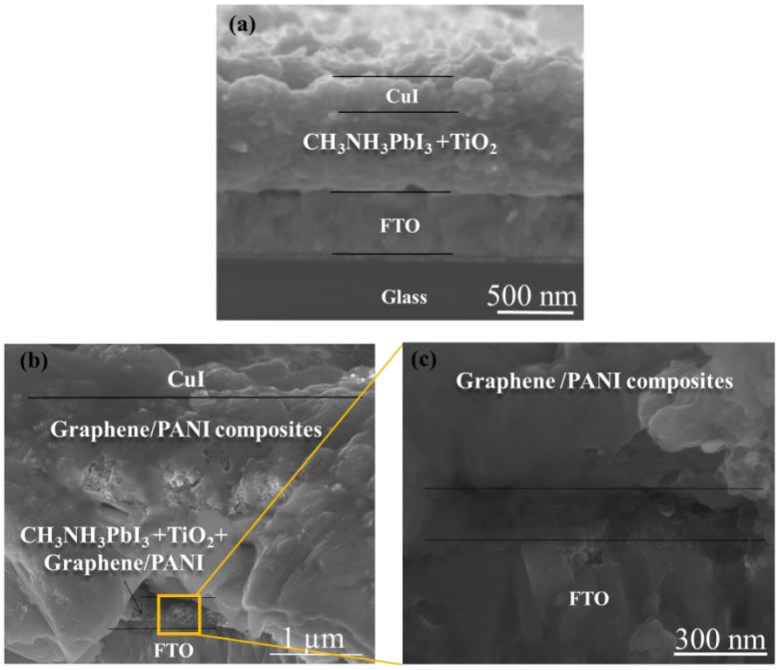

Figure 6.4. Cross-sectional scanning electron microscopy image of the (a) $CH_3NH_3PbI_3$ solar cell without any protective solar cells, (b) /Graphene/PANI protected $CH_3NH_3PbI_3$solar cell and (c) magnified image of FTO and TiO_2 with Graphene/PANI composite region showing infiltration of the composite into the perovskite.

A schematic of the device architecture is shown in Figure 6.5a. Figure 6.5b depicts the band edge positions of the different materials used in this work. Graphene present in the composite aids in the electronic transport, while PANI assists in the hole transport to copper iodide.

(a)

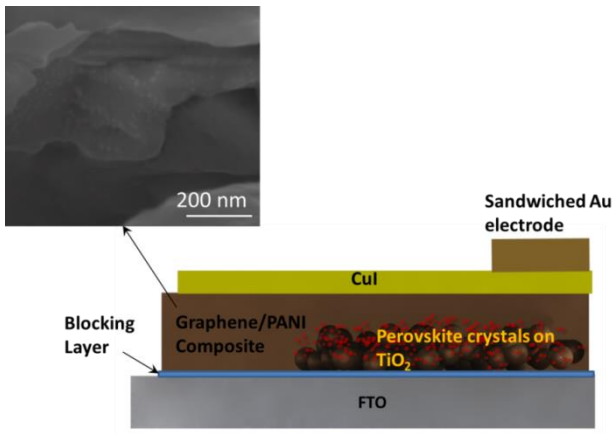

(b)

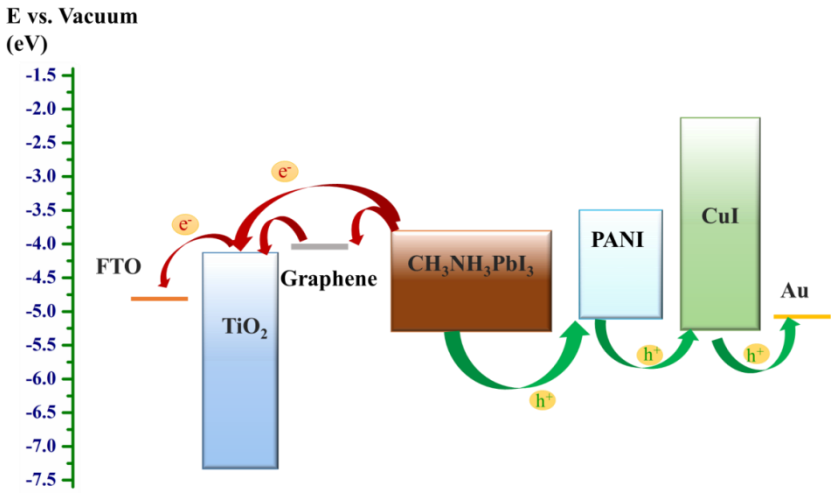

Figure 6.5. (a) Schematic of the electrode architecture of the moisture perovskite solar cells prepared in this work (b) Energy level diagram showing band edge locations of different materials used in the perovskite cells.

To validate if the graphene/PANI composite conformally coated the perovskite crystals, TEM analysis with elemental mapping has been performed. Figure 6.6a depicts the TEM image of an unprotected perovskite crystal. Figure 6.6b shows the TEM image of a graphene/PANI composite coated perovskite crystal and the image clearly indicates that the composite forms a thick conformal layer on the perovskite crystals.

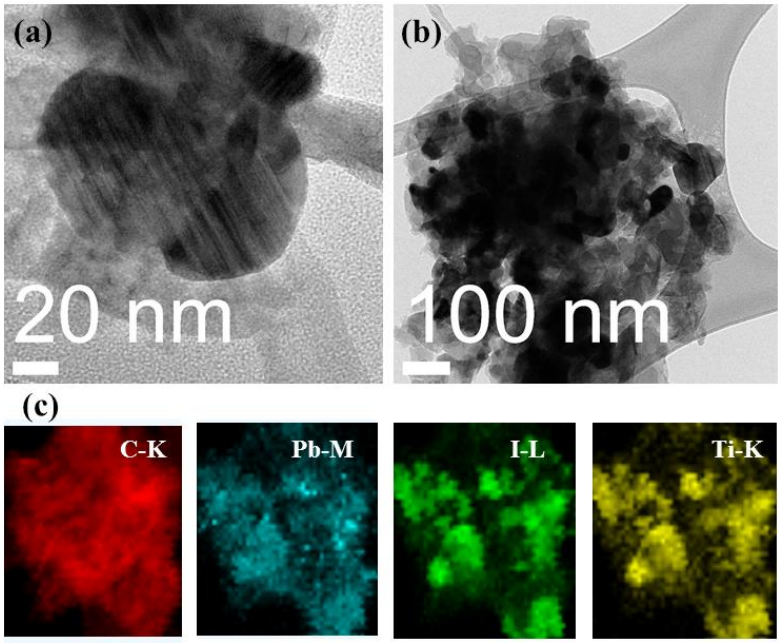

Figure 6.6. TEM image of (a) unprotected $CH_3NH_3PbI_3$crystal and (b) $CH_3NH_3PbI_3$ encapsulated Graphene/PANI composite (c) EDS color map of the encapsulated $CH_3NH_3PbI_3$ in Figure 6.6 (b) indicating complete coverage of the perovskite crystal with the Graphene/PANI composite.

Comparing the C-K and Pb-M, I-K, Ti-K elemental maps obtained from energy dispersive X-ray spectroscopy in the TEM (Figure 6.6 c), it can be concluded that the graphene/PANI composites uniformly encapsulate the perovskite crystals.

Current density–voltage (*J*–*V*) curves were obtained after exposing the perovskite cell to high humidity (99% relative humidity) for different times. The unprotected perovskite cells showed a rapid decline in the short-circuit current density and open circuit-voltage (Figure 6.7a) with time. After one hour of exposure to moisture, no photovoltaic behavior is seen from the cells. Figure 6.7 b to 6.7 d shows the J-V curves of perovskite solar cells encapsulated with graphene-PANI composite, with different thickness of the overlayers. Increasing the overlayer thickness improves the stability of the cells to moisture (Figure 6.7c & 6.7 d). The perovskite cell with the thickest overlayer (~4 μm) coating formed by spin coating the PANI and graphene solution 4 times (4x) hardly showed any variation in the photovoltaic performance with time when continuously exposed to high humidity. Increasing the thickness of the composite, increases the tortuosity in the path that water molecules have to travel before they can reach the perovskite crystals. This explains why thicker overlayers of the composite coatings show improved stability in high humidity conditions. The best performing cell with a protective coating showed a photocurrent of 14 mA/cm^2 and an open-circuit voltage of 450 mV.

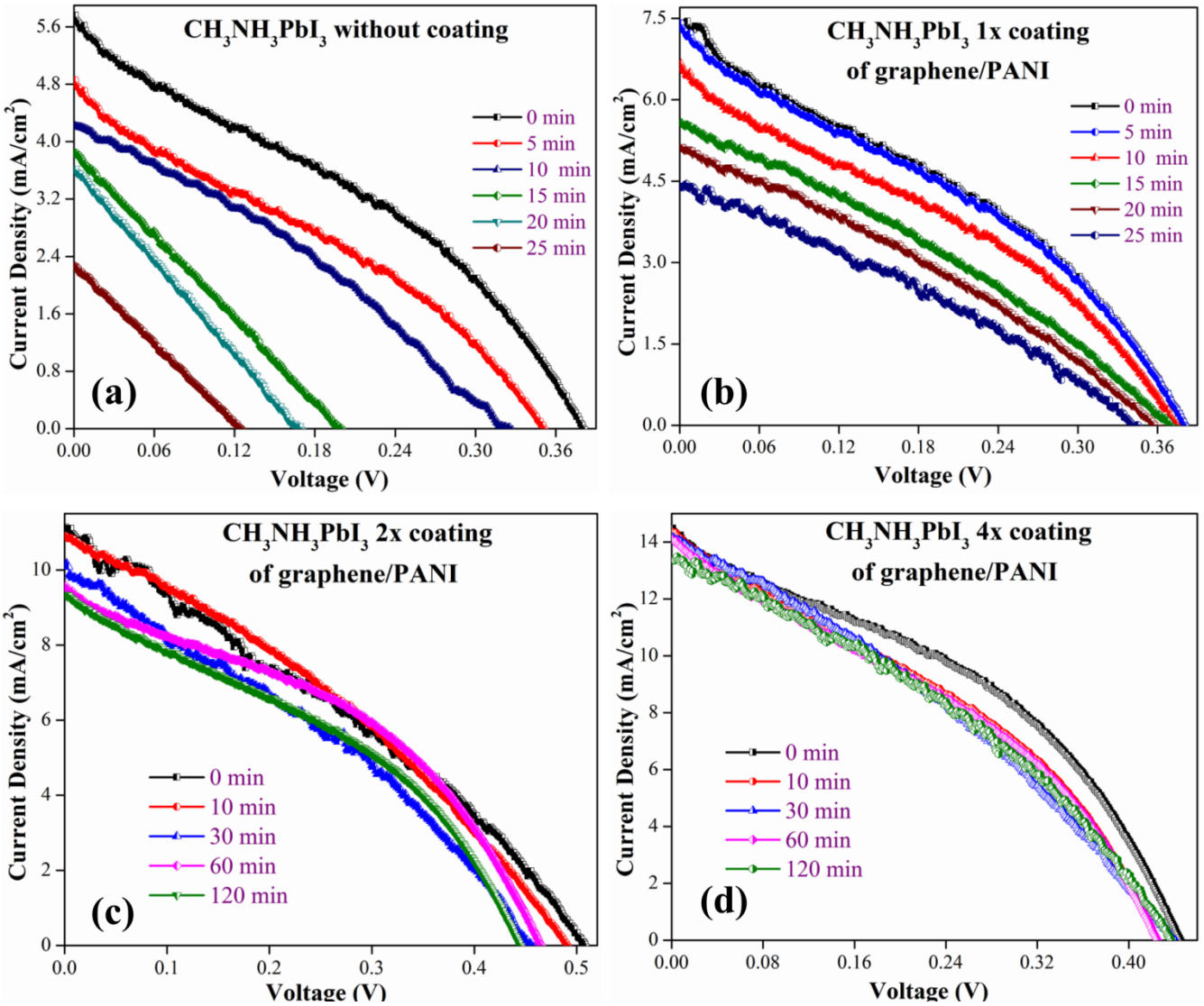

Figure 6.7. Time evolution of the current density–voltage characteristics measured at 1 Sun and AM 1.5 condition as a function of time for(a) unprotected $CH_3NH_3PbI_3$ solar cell (b),(c),(d) Graphene/PANI composite protected perovskite cells with different thickness of composite overlayer. The cells were exposed to air at 99 % relative humidity throughout the duration of the testing.

The low open-circuit voltage observed when compared to the best performing cell in literature fabricated with spiro-OMeTAD is due to the high recombination losses with CuI.[153] The performance of the device can be further optimized by a hole transport material that exhibits lower recombination losses than copper iodide. Devices fabricated without CuI, utilizing graphene/polyaniline itself as the hole transport material showed higher open-circuit voltage of 0.8 V, but lower short-circuit current density of 2.6 mA/cm^2 due to low conductivity of polyaniline when compared with copper iodide (Figure 6.8).

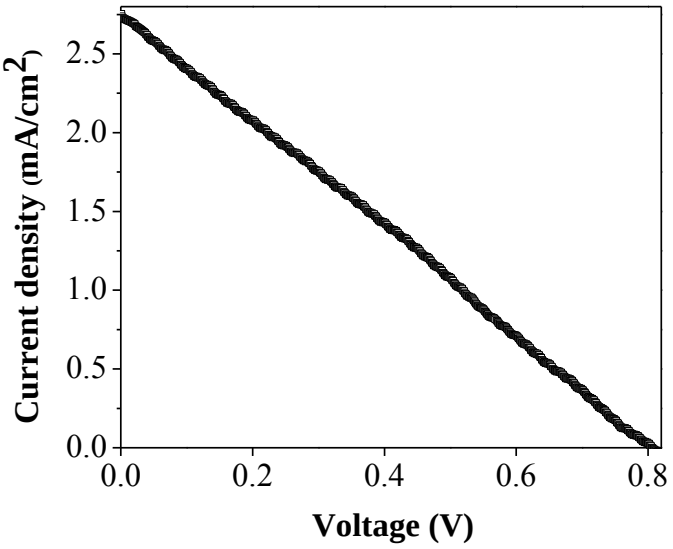

Figure 6.8. J-V curve of the perovskite solar cell using the graphene-PANI composite coating as the hole transport material. The counter electrode is a gold sputtered glass slide that is sandwiched against the perovskite electrode.

Further optimization, involving the use of more conductive polymeric materials than PANI can also boost the efficiency of the devices. A variation in photocurrents is observed in samples with different overlayer thickness, this could be due to the graphene/PANI composite acting as a buffer layer and preventing the direct contact of TiO_2

and the hole transport material. Lack of sufficient control over the crystal size during the perovskite growth is also another factor that can contribute to variation of photocurrents and hence claims with regards to increase in photocurrents with graphene/PANI encapsulating cannot be made.[154] Nevertheless, the results in Figure 6.7 show that graphene/PANI composite can provide a leak tight seal to perovskite against moisture. The loss in the power conversion efficiency is due to a slight decrease in the fill factor, which may be arising from the copper iodide losing its conductivity as it is not protected from moisture.

6.4 Summary

In summary, graphene/PANI composite has been found to act as a multifunctional coating enabling a good charge carrier transport and creating an impermeable seal to moisture. The composite prevents degradation of the perovskite from moisture as shown by the constant short circuit current density over an extended period of time. The protective coating effectively prevents the deterioration of the perovskite into the lead iodide and iodine. The high moisture impermeability could allow the processing of perovskite cells under atmospheric conditions once they are encapsulated with graphene/PANI composite. The use of composite protective coating developed in this work could also be extended to other lead free organic-inorganic metal halide perovskite that are both oxygen and moisture sensitive. The sandwich approach followed in this work could create opportunities for roll to roll or laminated perovskite cells, which could offer significant reduction in the processing costs of perovskite solar cells.

CHAPTER 7

LITHIUM INTERCALATION INTO NANOWIRE BASED MATERIALS

7.1 Introduction

In this chapter, the challenges associated with a layered lithium rich metal oxide, Li_2MnO_3, such as poor surface stability and poor capacity retention are addressed by using a single crystalline nanowire architecture. Furthermore, the large scale synthesis of manganese oxides NWs, which is a precursor for making Li_2MnO_3 NWs, is also a challenge and has been addressed in this work by using a scalable solvo-plasma technique. Several reports on 1-D nanomaterials of manganese oxides have utilized hydrothermal [155, 156], solvothermal [79] and template based methods [157] that are tough to scale up due to the long reaction times scales [158, 159] and the use of expensive precursors. For example, the commonly used hydrothermal method for synthesizing 1D nanostructures of manganese oxide requires at least 12 h of autoclaving.[79],[80] Our research group has recently reported a scalable approach, called solvo-plasma process, for making titanium dioxide NWs. The solvo-plasma process involves the exposure of inexpensive precursors such as metal oxide powders and alkali metal salts to an atmospheric microwave plasma.[100] The short reaction times scales (about a few seconds to 5 minutes) in the solvo-plasma and inexpensive precursors provide a scalable approach for the synthesis of manganese oxide nanowires. Further, detailed structural characterization was performed to understand the mechanism of phase transformation in Li_2MnO_3 NWs.

7.2 Experimental

Micron sized MnO_2 powder (Alfa Aesar) and KCl (Sigma Aldrich) were mixed together with water in a mortar and pestle to make a paste. A thick layer (~ 100 microns) of this paste is deposited on a stainless steel substrate. The substrate is then dried on a hot plate at 70 °C to evaporate the water and is cooled to room temperature and subsequently exposed to an atmospheric plasma flame for 5 minutes. The details of experimental setup of the atmospheric microwave plasma reactor are described in a prior publication.[100] An air flow rate of 8 lpm and a plasma power of 750 W were used. The thick film was scraped from the substrate while leaving a small part of it still attached to the substrate, in order to prevent contamination from stainless steel foil. The resulting nanowire powder is washed with deionized water several times to remove the unreacted salt, and then immersed in 1 M HCl for 2 hours. The cleaned NW powder is then heated to 200 °C to form manganese oxide. For synthesis of lithium manganese oxide NWs, the manganese oxide NWs and lithium hydroxide (1:1 ratio) were mixed in ethanol to form a homogeneous mixture and then heated in an oven for 12 h at 480 °C. The large-scale synthesis of Li_2MnO_3 NWs is schematically illustrated in Figure 7.1.

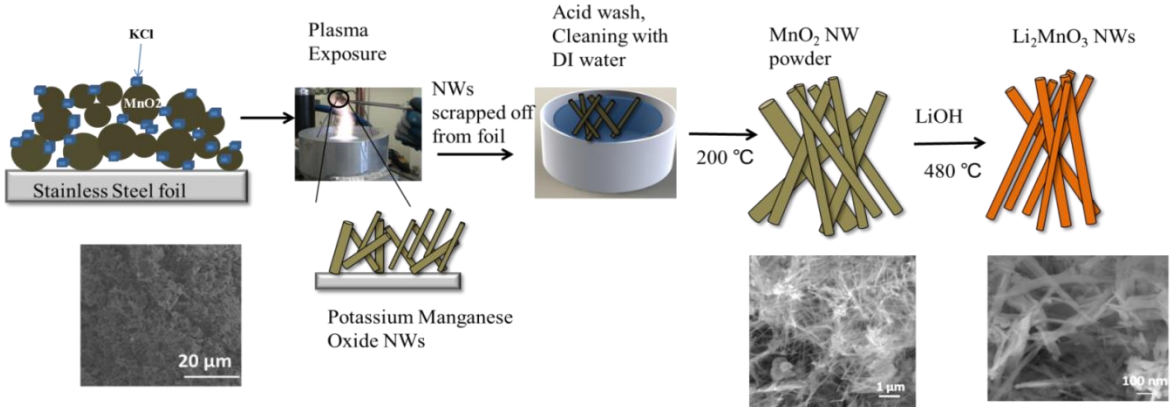

Figure 7.1. Schematic of the solvo-plasma process for synthesizing MnO_2 NWs followed by solid-state alloying to prepare Li_2MnO_3 NWs.

The battery testing was carried out using a coin cell configuration using an Arbin battery tester. The electrochemical characterization is performed using a CR2013 coin-type cell assembled in a dry argon-filled glove box. The cathode is prepared by mixing 10 mg of active electrode with 3mg of teflonized acetylene black (TAB-2) as a conducting binder. The mixture is then pressed onto stainless steel mesh. The average thickness of cathode is 18-20 µm and lithium foil is used as a counter electrode separated by a porous propylene film (ADVANTEC GB-100R). The cathode is dried at 150°C for 5 h under vacuum. The electrolyte used is a 1M solution of $LiPF_6$ in EC: DMC mixture (1:2). The charge-discharge measurements are carried out using a battery tester (16-channel Arbin Instrument, USA) in a voltage window of 2 V to 4.5 V. Cyclic voltammetry is performed using eDaQ e-corder and potentiostat. A loading of 5 mg/cm^{2}of active material is used for all our electrodes tested in this work.

Scanning electron microscopy (SEM) is performed with a NOVA FEI scanning electron microscopy. XRD patterns are obtained with a Bruker D8 discover X-ray

diffractometer. Cu K_{alpha} (1.549 °A) radiation is used for obtaining the XRD patterns. Transmission electron microscopy (TEM) is performed using a Tecnai F20 FEI TEM equipped with a Gatan 2002 GIF system.

7.3 Results and Discussion

The Li_2MnO_3 NWs have an average diameter of 50 nm and lengths close to a 1 μm(Figure 7.2 a). The as-synthesized Li_2MnO_3 NWs are found to be single crystalline and have a d-spacing of 0.32 nm (Figure 7.2 b), which matches the d-spacing of 0.317 nm of the (022) plane of Li_2MnO_3 NWs.

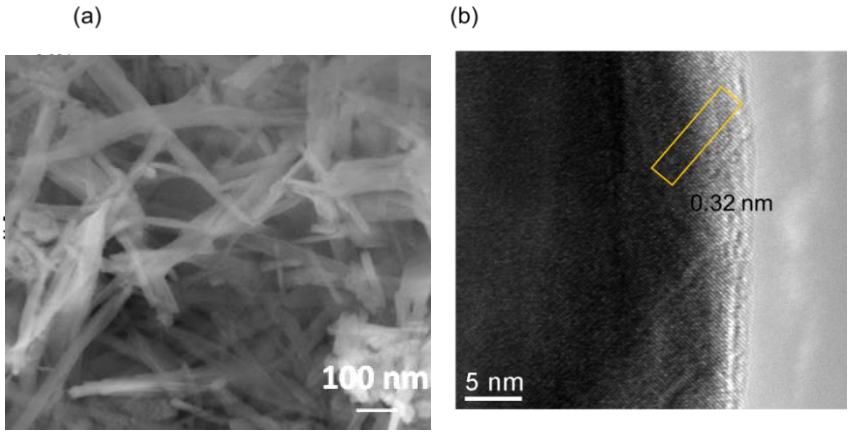

Figure 7.2 (a) SEM image of the as synthesized Li_2MnO_3 NWs and (b) TEM image of the as-synthesized Li_2MnO_3 NW.

Prior to testing the Li_2MnO_3 NWs, the performance of the MnO_2 NWs as cathodes in Li ion batteries has been evaluated. The electrochemical performance testing of MnO_2 NWs shows severe capacity loss with cycling (Figure 7.3). This can be attributed to slow kinetics of Li intercalation and deintercalation as indicated by the wide peak separation between the Li ion insertion and removal peaks in the CV (Figure 7.4b).

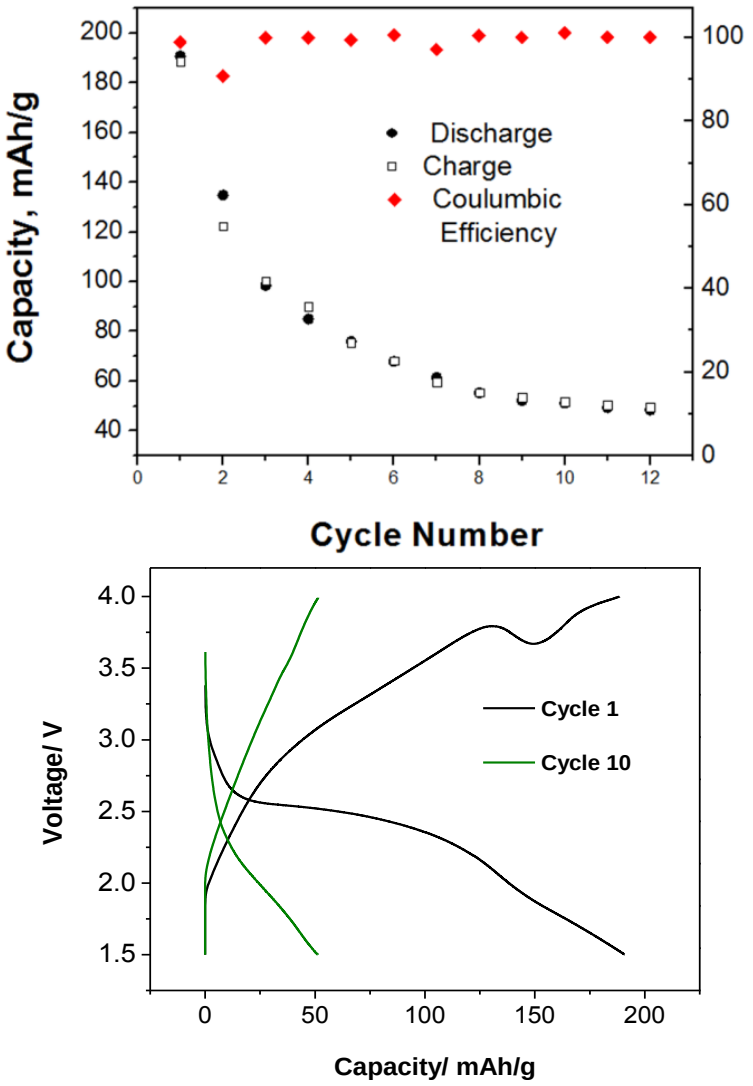

Figure 7.3. (a) Charge and discharge capacities, columbic efficiency of manganese oxide NWs for the first 12 cycles at 0.2 C rate (b) Charge and discharge voltage profiles for the cycles 1 and 10.

The observed capacity loss with cycling cannot be attributed to the loss of structural integrity of the nanowire sample, as SEM images of the MnO_2 NWs after cycling revealed that the NWs retained their morphology (Figure 7.4 a)

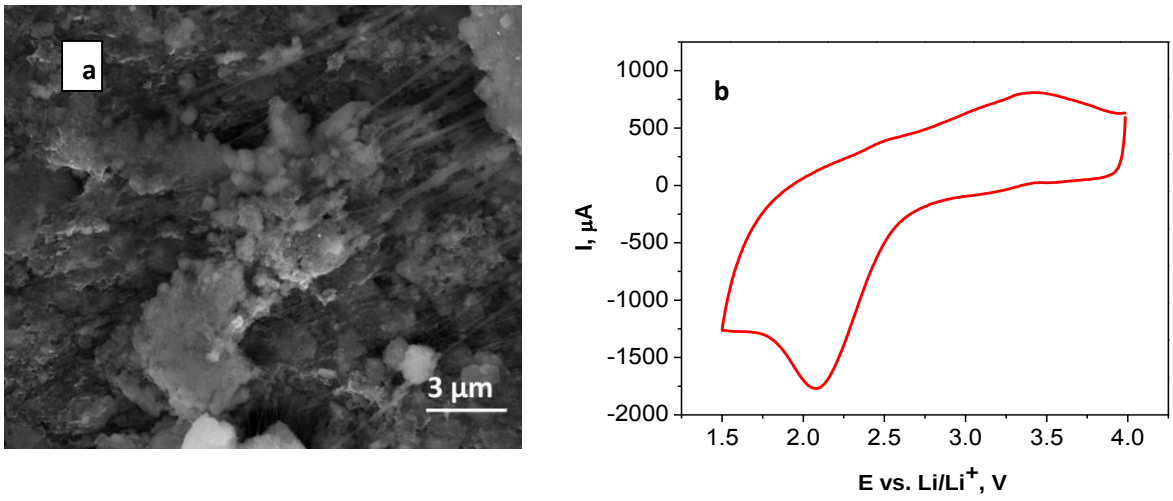

Figure 7.4. (a) Scanning electron microscopy image shows that the morphology of the MnO_2 NW is still retained after 10 cycles, (b) cyclic voltammogram of the MnO_2 NWs.

In contrast, when compared to MnO_2 NWs, the Li_2MnO_3 NWs showed faster Li intercalation and deintercalation kinetics as indicated from closer separation of the Li insertion and extraction peaks in the cyclic voltammogram of Li_2MnO_3 NWs (Figure 7.5)

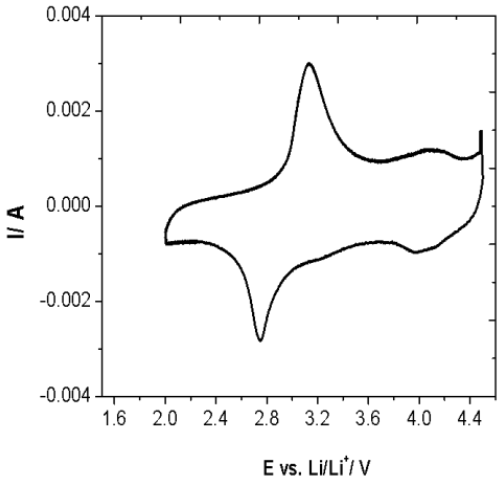

Figure 7.5. Cyclic voltammogram of Li_2MnO_3NWs at a scan rate of 1 mV/s.

The cathodic peaks at 4.05 V and 2.7 V correspond to Li intercalation while the anodic peaks at 3.1 V and 4.1 V correspond to Li de-intercalation respectively. The redox peaks close to 3 V can be attributed to the phase transformation of the layered structure to a spinel structure.[77, 160] Although the oxidation state of Mn in Li_2MnO_3 is expected to +4 in theory, recent reports indicated the presence of both +4 and +3 states of Mn in Li_2MnO_3 prepared at low temperatures (< 800 ℃). Our prior work showed that oxygen vacancies are typically present in metal oxide nanowires.[161] The +3 oxidation of Mn could also be caused by the oxygen vacancies present in Li_2MnO_3 NWs. Hence, the peaks observed in the CV (Figure 7.5) at 4.05 V and 4.1 V can be attributed to the Mn^{+3}/Mn^{+4} redox reaction in Li_2MnO_3.[160, 162]

The electrochemical performance and cycling stability of the Li_2MnO_3 NWs was evaluated by determining the charge-discharge characteristics using a coin cell configuration. Figure 7.6 shows charge and discharge voltage profile for Li_2MnO_3 NWs. It should also be noted that our coin cell testing has been done at relatively high cell loading of 5 mg/cm^2 of active material. The cycling was carried out in the 2 V to 4.5 V range.

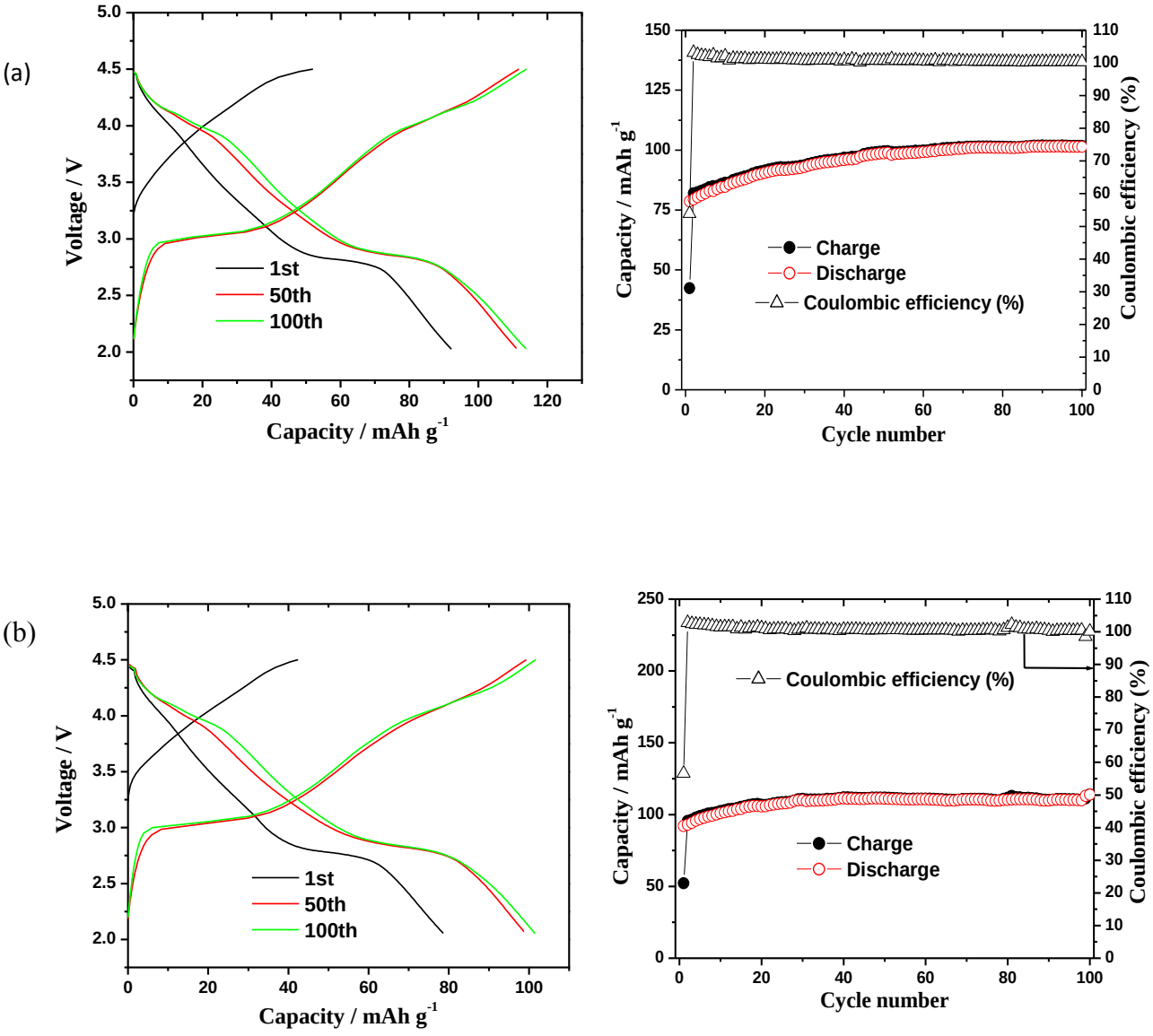

Figure 7.6. Charge-discharge capacity curves and cycleability of Li_2MnO_3NWs at (a) 1C-rate and (b) at 5 C-rate respectively.

The pseudo plateau region observed at 4.1 V is due to the lithium extraction from $LiMn_2O_4$ spinel phase. This plateau is not clearly seen in the first charge-discharge cycle, but becomes more dominant in the subsequent charge/discharge cycles indicating that $LiMn_2O_4$ is formed in the first few cycles of lithiation and delithiation. The diagonal shape of the voltage profile between 4 V and 3 V is similar to that of Li_xMnO_2 phase and the

plateau region at 3 V has been attributed to lithium insertion/extraction in the octahedral sites of the spinel $Li_{1+x}Mn_2O_4$ phase[163]. Li_2MnO_3 NWs showed a low initial capacity of ~80 mAh g^{-1} at 1C and ~90 mAh g^{-1} at 5C respectively. This observed capacity is much lower than the theoretical capacity of Li_2MnO_3, which is 280 mAh g^{-1}. The lower capacity has been attributed to the electrochemically inactive properties of Li_2MnO_3 when cycling at a voltage less than 4.5V. [164, 165]

In order to understand the different structural transformations occurring in the Li_2MnO_3 NWs, two different electrodes are cycled to 3.5 V and 2 V and characterized using both XRD (Figure 7.7) and HRTEM (Figure 7.8). The XRD pattern of the as-synthesized Li_2MnO_3 NWs is shown in Figure 7.7a, and matches with the standard XRD pattern for Li_2MnO_3 (PDF # 00-018-0737). None of the peaks in the XRD pattern (Figure 7.7a) match with the $LiMn_2O_4$ phase. Further, the absence of any plateau at 4 V region in first charge cycle of Figure 7.6, shows that there is negligible amount of $LiMn_2O_4$ in the as-synthesized sample. The XRD of the sample discharged to 3.5 V showed Li_2MnO_3 as the dominant phase, in addition to $LiMn_2O_4$, $Li_{0.78}Mn_{0.85}O_2$ and $LiMn_3O_4$. The sample is further discharged to 2 V and Li2MnO3 is still observed as the dominant phase and the formation of tetragonal $Li_2Mn_2O_4$ is also seen. The phase transition from cubic $LiMn_2O_4$ to tetragonal $Li_2Mn_2O_4$ has been previously reported in as a result of Jahn-Teller distortion effect.[79, 166]

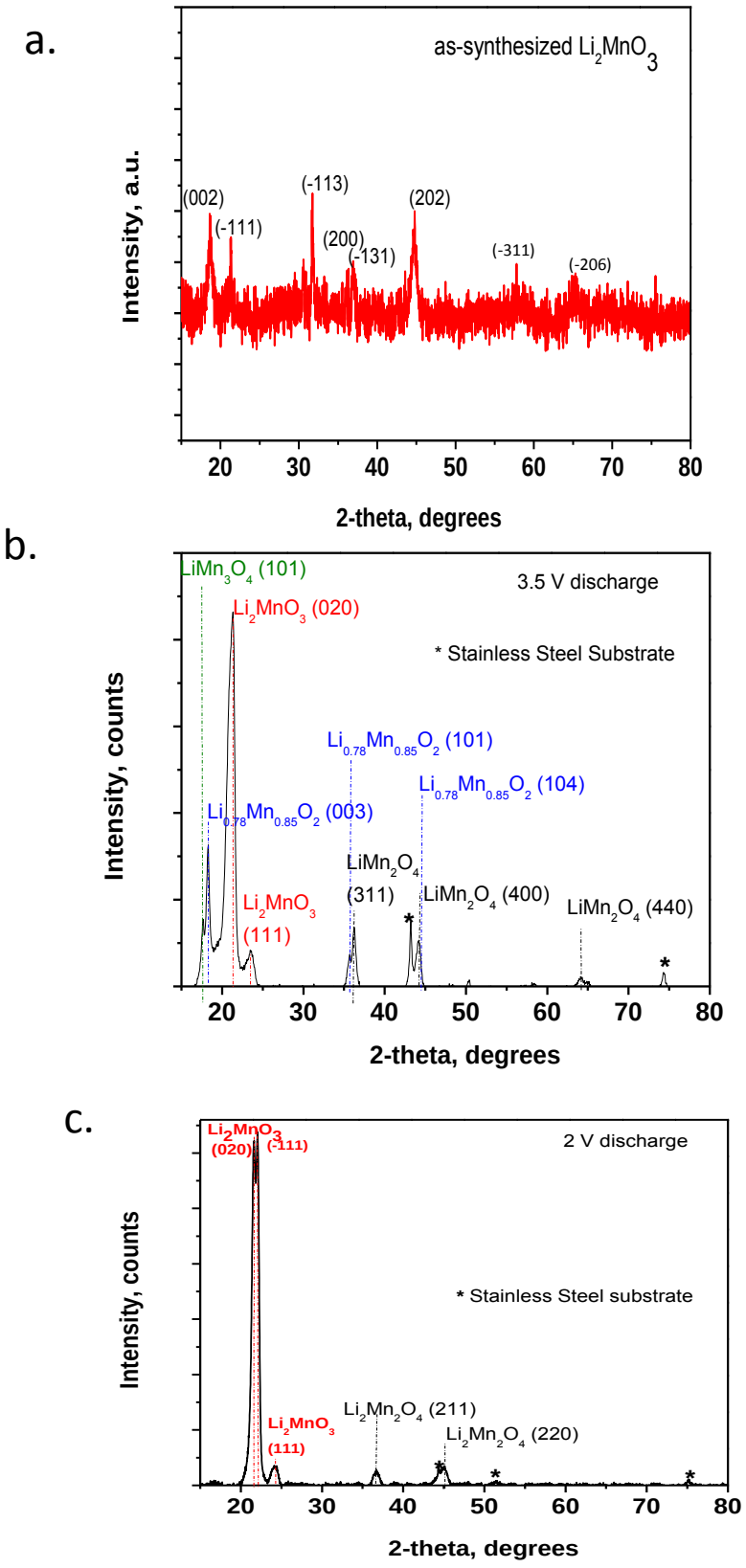

Figure 7.7. XRD of (a) as-synthesized Li_2MnO_3 nanowires (b) Li_2MnO_3 NWs discharged to 3.5 V and (c) Li_2MnO_3 NWs discharged to 2 V.

To investigate the spatial location of the different phases within the nanowire, HRTEM analysis was performed on the samples. Figure 7.8 shows HRTEM images of sample discharged to 3.5 V and 2 V respectively. The d-spacing of 0.36 nm (Figure 7.8 c) corresponds to the (111) plane of Li_2MnO_3. Analysis of XRD spectra (Figure 7.7) and d-spacing of 0.47 nm observed in HRTEM images (Figures 7.8 and 7.9) indicates the presence $LiMn_2O_4$ spinel present on the shell of the nanowires. Large d-spacings of 0.92 nm were also observed in a few Li_2MnO_3 NWs discharged to 2 V. The d-spacing is in close agreement with the layered structure compound with composition $(Li_2O)_{0.12} . MnO_2$. The formation of $(Li_2O)_{0.12} . MnO_2$ indicates the extraction of lithium and oxygen from the core of the NWs. These results suggest core-shell architecture of layered Li_2MnO_3 covered with a shell of polycrystalline $LiMn_2O_4$.

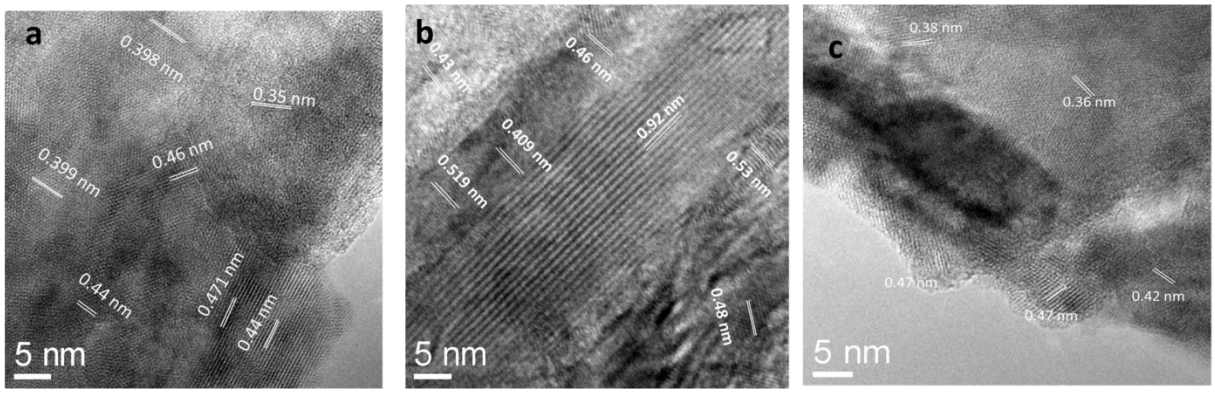

Figure 7.8. (a) & (b) HRTEM images of Li_2MnO_3 NWs discharged to 2 V and (c) HRTEM image of Li_2MnO_3 NW discharged to 3.5 V.

Figure 7.9 shows HRTEM images of Li_2MnO_3 NWs discharged to 2V. Figure 7.9 a shows a Li_2MnO_3 core- $LiMn_2O_4$ shell nanowire.

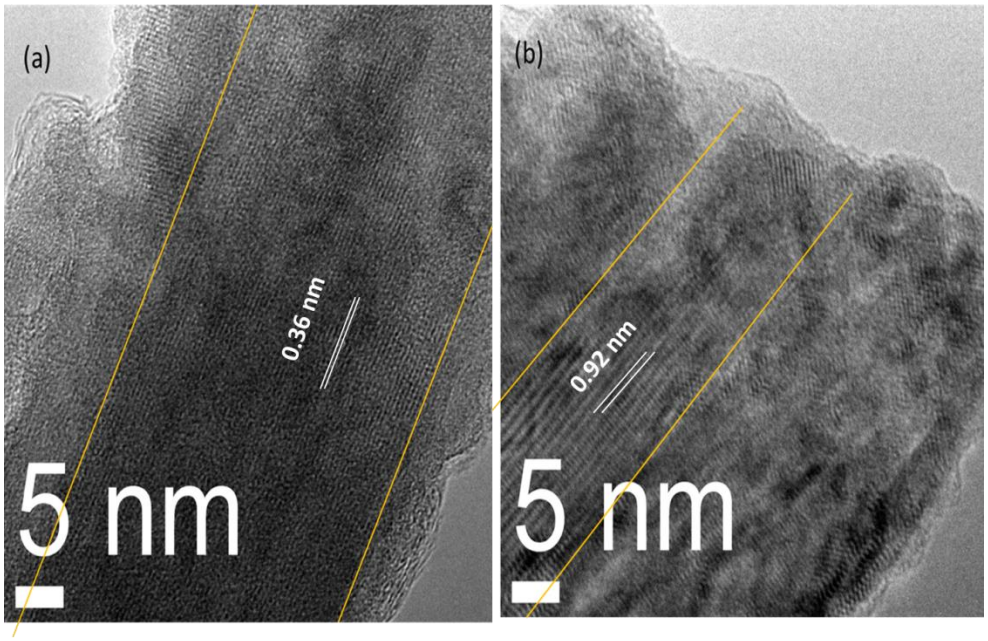

Figure 7.9. HRTEM images showing a polycrystalline shell along Li_2MnO_3 NWs discharged to 2 V.

Basing on the average thickness of the shell layer and the densities of core (density of Li_2MnO_3 is 3.896 g/cc [PDF # 01-027-3120]) and shell materials (density of $LiMn_2O_4$ is 4.233 g/cc [PDF # 01-070-3120]), the weight % of $LiMn_2O_4$ is estimated to be 70.1 % when the core is still in the form of Li_2MnO_3. Details of the calculation are listed in Appendix 1. When the core is depleted of lithium and oxygen, i.e., in the form of $(Li_2O)_x.MnO_2$, the weight % of the $LiMn_2O_4$ shell is calculated to be around 92.6 % . The density of $(Li_2O)_x.MnO_2$, where x is small, is approximated to the density of $(Li_2O)_{0.12}.MnO_2$ which 4.221 g/cc [PDF # 01-074-8725]). The high volume fraction of the spinel shell accounts for observed high weight % spinel in the nanowires. The presence of layered single crystalline core with a 15-30 nm diameter, as observed from the HRTEM images, allows for fast charge transport in the electrodes. After 40 cycles, the capacity of battery starts to stabilize to a constant value (Figure 7.6 b). Hence, the $LiMn_2O_4$ shell thickness at

this point calculated as 14 nm (for an NW of diameter 56 nm) could be the regarded as the minimum shell thickness required for stable capacity retention. The weight % of spinel and layered phases based on TEM analysis are based on the shell thickness on a limited number of nanowires. To estimate an average value, the observed first cycle discharge capacity was used (See Table S1 in Appendix 1).[163] Basing on these calculations after 100 cycles the average weight % of $LiMn_2O_4$ is calculated as 85 %. Details of the calculation are listed in Appendix 1.

The phase of the shell and core of the NWs was also corroborated from selected area diffraction (SAED) analysis performed on the nanowires. Figure 7.10 shows the SAED patterns of the Li_2MnO_3 NW sample discharged to 3.5 V (Figure 7.10 a) and 2 V (Figure 7.10 b). The SAED patterns were analyzed by the rotational average method. The peaks positions for different lithium manganese oxide compounds are also indicated for comparison. The analysis shows that the sample discharged to 3.5 V has $LiMn_2O_4$ and Li_2MnO_3 as the phases present in the sample. The sample discharged 2 V showed $Li_2Mn_2O_4$, Li_2MnO_3 and few peaks also matched with $(Li_2O)_{0.12}MnO_2$. The SAED phase analyses are in agreement with the observations from lattice spacing measurement and XRD.

Formations of spinel phases on layered Li rich compounds such as Li_2MnO_3 have been observed to enhance the cycling stability. For example, an AlF_3 coating on Li_2MnO_3 has been reported to exhibit good capacity due to formation of spinel phase on surface of cathode along with Li leaching from the core.[93]

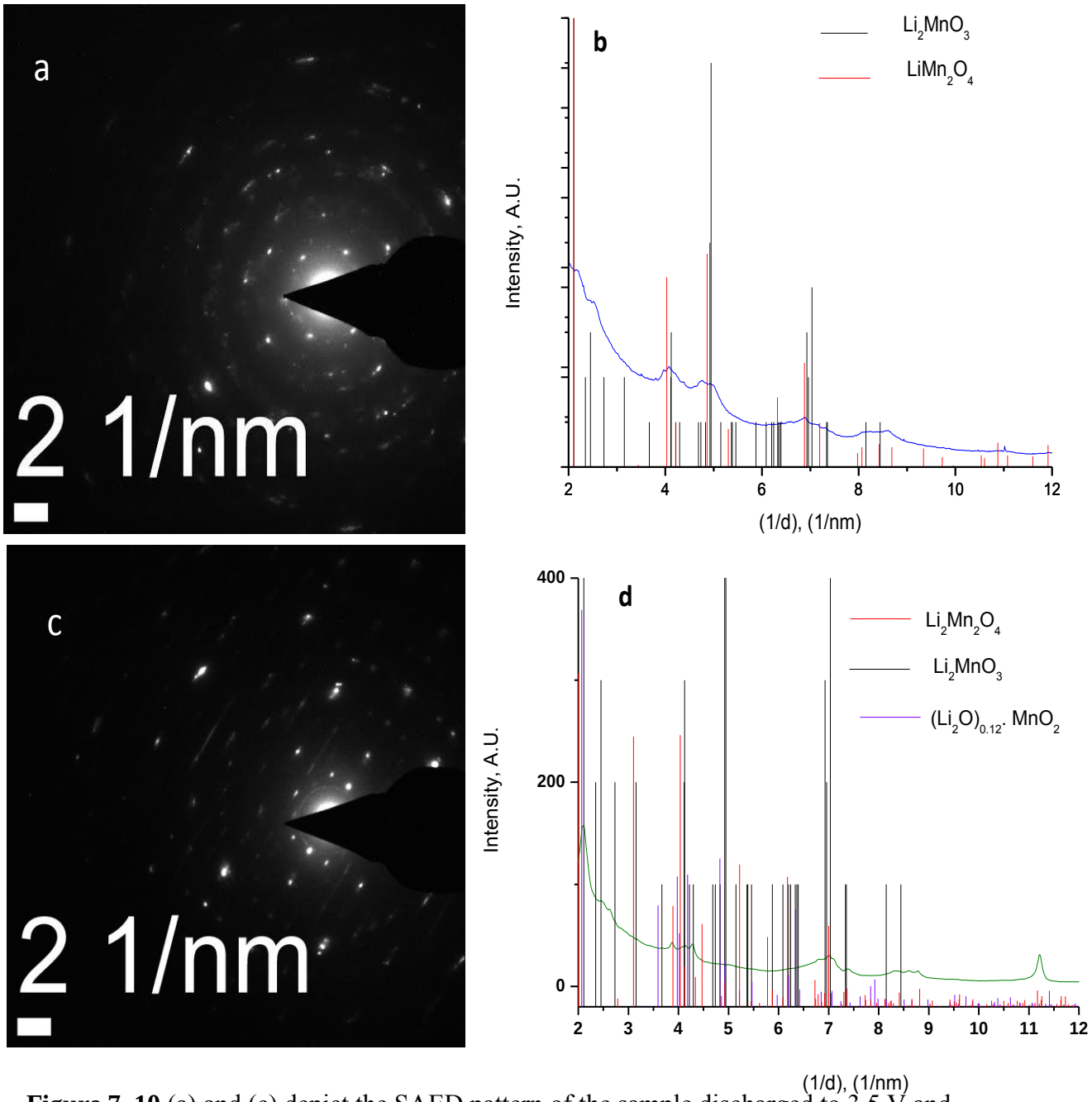

Figure 7. 10 (a) and (c) depict the SAED pattern of the sample discharged to 3.5 V and 2V respectively. (b) and (d) show the rotational average analysis of these SAED patterns respectively.

Chen et al. reported that a spinel $Li_{1+x}Mn_2O_4$ layer formed by a dip coating the $Li_{1.2}Mn_{0.6}Ni_{0.2}O_2$ microparticles enhanced the capacity retention by acting as a barrier for erosion of the layered material into the electrolyte while still permitting fast ion transport through the 3D Li ion transport channels in the spinel.[94],[95] It has been shown that Li delithiation causes a surface reconstruction of the layered lithium metal oxide, causing the transition metal atoms migrating to the lithium sites and formation of the spinel phase.[144, 167] Thus surface reconstruction has been shown to add a significant charge transport resistance with some initial capacity loss. However, it is interesting to note that the opposite effect is observed in our case, i.e., the capacity increases with the cycling and then stabilizes at a constant value. In the case of nanowires, the presence of a single crystal core of the nanowire could assist in the stress associated with phase transitions of the spinel phase at the surface without leading to capacity loss.

Figure 7.11 shows the proposed mechanism of surface reconstruction and phase transformation occur in Li_2MnO_3 NWs. During the first charge cycle, where Li deintercalation occurs, the Li ions along with oxygen anions diffuse outwards from the core of the NW. An indirect evidence for this the observation of wide d-spacing in our HRTEM images (Figures 7.8 and 7.9).

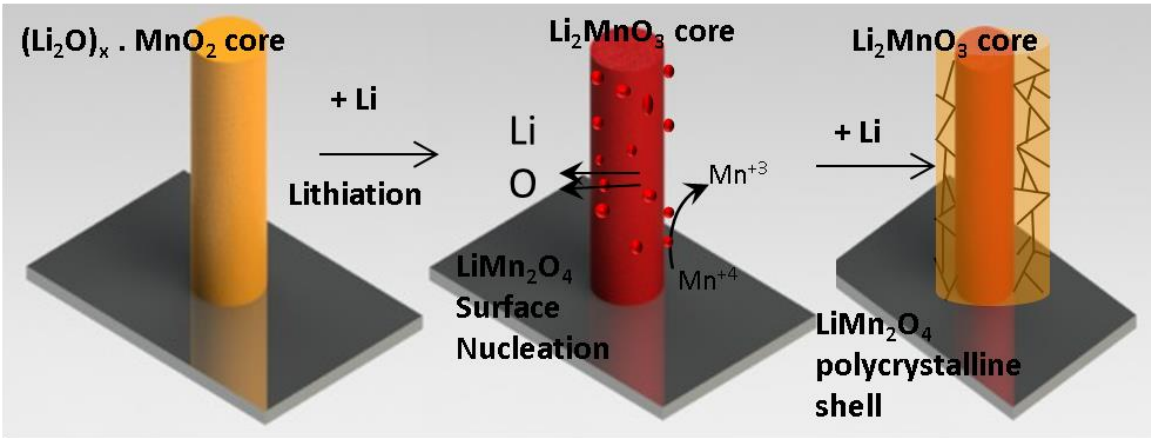

Figure 7.11. Schematic illustrating the formation of a $LiMn_2O_4$ shell on the Li_2MnO_3 NWs.

The oxygen anions then reduce the valence of Mn atoms from +4 to +3 and reduce Li^+ ions to Li atoms. The Li, Mn and O atoms reaching the surface of the nanowire react to nucleate and grow $LiMn_2O_4$ shell around the nanowire during the first discharge cycle. No peak or plateaus are observed in our first charge process upto 4.5 V indicating that oxygen atoms migrate to the surface rather than oxygen being evolved in the first cycle. In addition, there is clear evidence for oxygen evolution in when charge the cells upto 4.8 V (Figure 7.10). To validate this argument, the Li_2MnO_3 coin cells were are charged and discharged in the 2 V to 4.8 V voltage window. Figure 7.12 shows the charge-discharge for a Li_2MnO_3 NW sample that is cycled in the 2 V to 4.8 V window on sample that was previously used for C-rate testing in the 2 V to 4.5 V window. (Figure 7.6). When the sample is charged above 4.5 V, there is significant oxygen evolution and this could lead to formation of non-conformal spinel shell. The pseudo plateau at 4.5 is indicative of oxygen evolution from the electrode.

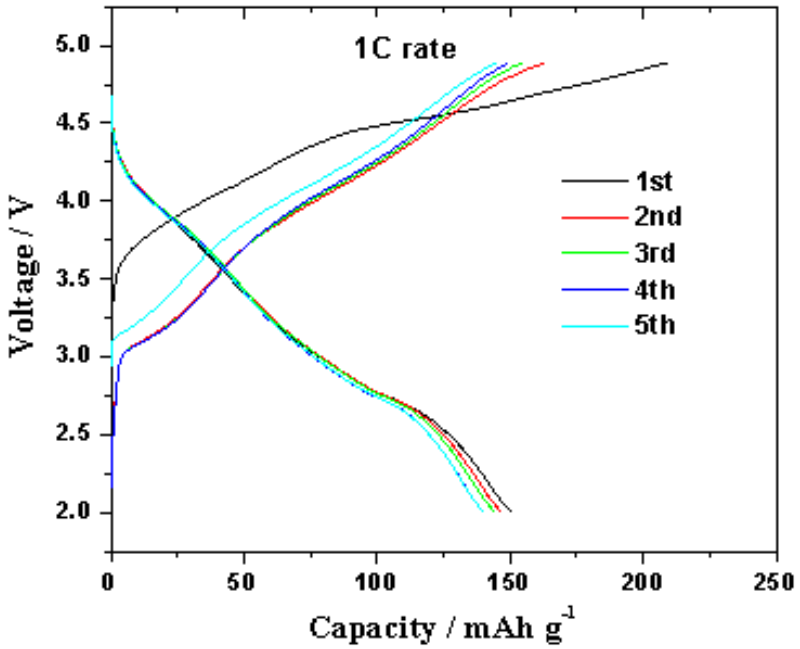

Figure 7.12. Charge-Discharge curves for Li_2MnO_3 NWs cycled in the 2 V to 4.8 V voltage window.

The proposed reaction mechanism is also supported by the findings of Chen and coworkers who used EELS spectroscopy and high resolution S-TEM to show that the oxidation state of Mn changes from +4 to +3 during the cycling and also showed the formation of spinel phase on the surface of layered lithium manganese oxide particles.[167] The nucleation and growth of spinel during the first cycle is responsible for the low coulombic efficiency in the first cycle as some of the charge is utilized for the transformation to the spinel phase besides carrying out the lithiation/delithiation reaction.

During lithiation or discharge, the delithiated core changes back to Li_2MnO_3, with $LiMn_2O_4$ nanocrystalline shell on the surface. Further lithiation (from 3.5 V to 2 V) changes the shell from cubic $LiMn_2O_4$ to tetragonal $Li_2Mn_2O_4$ due to Jahn-Teller distortion effect. $LiMn_2O_4$nanocrystalline shell stabilized the $Li_2MnO_3$from erosion effects of the electrolyte

and also contributes to a slight improvement in capacity with cycling. The single crystalline NW core allows for the phase transformation on the spinel shell to occur without any capacity fade. Further, the single crystal core, depleted of insulating Li_2O, exhibits high conductivity allowing fast electron transport. A possible explanation is that the in-plane conductivity along the planes observed in the depleted core could possibly be higher than that of layered compound, Li_2MnO_3.

The increased capacity with cycling could be attributed to the shell formation of $LiMn_2O_4$ phase, which has been reported to show much higher capacity at higher C rates(116 mAh/g at 1 C rate)[79] when compared to the capacity Li_2MnO_3 phase (75 mAh/g at 0.44 C)[77]. Prior reports have shown significant capacity loss associated with voltage plateau at 3 V due to the difficulty in reversing the tetragonal phase back to the cubic phase (caused by Jahn-Teller distortion) and significant strain on the lattice during this phase transformation.[168, 169] However no capacity fade associated with transition is observed in our system. This could be due to the facile stress relaxation of the extremely thin $LiMn_2O_4$ layer on a single crystal NW. The small transport length scales for Li ions, oxygen and manganese atoms along the diameter single crystal nanowires allow for the thick $LiMn_2O_4$ spinel shell (15-20 nm) formation on the surface resulting in high columbic efficiency and excellent capacity retention at high C rates. In case of polycrystalline nano/microparticles of Li_2MnO_3, the formation of $LiMn_2O_4$ is either very thin (< 2 nm)[144] or non-conformal[170, 171] leading to poor protection Li_2MnO_3 especially at high C rates. This makes single crystalline Li_2MnO_3 nanowires a unique platform for surface phase transformation to obtain thicker and more conformal shell of $LiMn_2O_4$. The experimental observations by Meng et al. also support our argument of oxygen migration

when the Li_2MnO_3 cells are charged only until 4.5 V.[144] An important requirement for Li ion battery cathode is the high capacity retention when the electrode is cycled at high C rates. To illustrate the high rate capability of the Li_2MnO_3 NWs, the charge discharge cycles at different C rates (for the electrode tested at 1C for 100 cycles) are performed. Figure 7.13 shows the cycling performance of Li_2MnO_3 NW cathode at different C-rates, the capacity drops from 135 mAh/g to 125 mAh/g, 120 mAh/g, 110 mAh/g as the C-rate increased from 1C to 5C, 10C and 20C respectively.

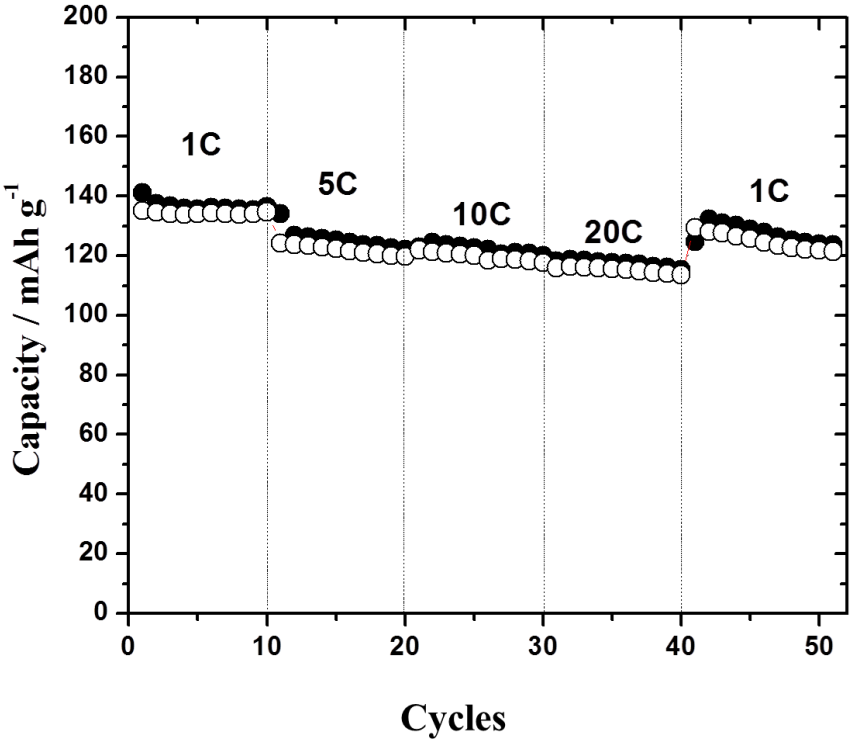

Figure 7.13.C-rate test of Li_2MnO_3 NWs at different current densities.

The capacity increased back to 135 mAh/g when cycled at 1C rate indicating good reversibility and high rate capacity of Li_2MnO_3 NWs. The fast kinetics of Li intercalation and de-intercalation in the Li_2MnO_3 NWs with a spinel phase protective coating are

responsible for the observed high rate capacity. Most importantly, the high scalability of the solvo-plasma method makes it possible to produce commercial scale quantities of manganese oxide nanowires for application towards Li ion batteries. Furthermore, Li_2MnO_3 NWs show potential for the use of thick electrodes because of their impressive capacity retention at high C-rates.

7.4 Summary

In summary, a scalable approach for synthesizing MnO_2 NWs is demonstrated using a solvo-plasma technique. Li_2MnO_3 NWs prepared by the solid state lithiation of the MnO_2 NWs, showed high capacity retention (95.8 %) even at 20 C-rate. The formation of a spinel phase $LiMn_2O_4$ on the shell of the nanowires resulted in a gradual capacity increase with cycling and allowed a stable capacity to be maintained at high C-rates and high columbic efficiency. The nanocrystalline $LiMn_2O_4$ shell undergoes Jahn-Teller distortion without significant capacity loss, due to facile stress relaxation. Single crystalline Li_2MnO_3 NWs provide a unique platform for facile surface phase transformation, due to small transport length scales in the radial direction, resulting in formation of thick and conformal $LiMn_2O_4$ protective shell on the Li_2MnO_3 NWs. The spinel shell results in excellent capacity retention even at very high C-rates.

CHAPTER 8
CONCLUSIONS

Electrode architectures for DSCs:

Electron transport in nanoparticle networks is limited by the poor interconnectivity between the nanoparticles. Increasing the interconnectivity between the particles, resulted in improved electron transport, higher electron lifetimes and improved photovoltaic performance. Fundamental studies of electron transport showed that the trap states play an important role in determining the transport times in titania based architectures and that single crystallinity in nanowires does not guarantee faster electron transport when compared with nanoparticles. Surface passivation of titania nanoparticle coated tin oxide nanowire hybrid architectures with a monolayer of alumina resulted in tenfold improvement in photovoltaic performance when compared with conventionally used alumina coated titania nanoparticles due to fast electron transport time scale in nanowire architectures.

Electrode architectures for perovskite solar cells:

Graphene-polyaniline composite coatings on perovskite crystals have been demonstrated to be highly moisture resistant even at very high relative humidity (99 %) due to the high tortuosity in diffusion paths for water molecules to reach the perovskite crystals. The high electronic conductivity of graphene and hole conductivity of polyaniline allow for the use of thick protective coatings with high tortuosity. XRD analysis on perovskite crystals exposed to moisture for different times corroborate the reaction mechanism proposed in

literature involving the degradation of methyl ammonium lead iodide to lead iodide and iodine.

Electrode architectures for cathodes of Li ion batteries:

Single crystalline nanowires of Li_2MnO_3 allow for the surface phase transformation of the layered Li_2MnO_3 to spinel $LiMn_2O_4$ due to their facile strain relaxation properties and short diffusion pathways for Li and O atoms to the surface of the nanowires. The formation of a thick and conformal spinel shell allows for stable capacity retention and high coloumbic efficiency to be achieved at high C rates. HRTEM and XRD investigation of the cycled electrodes show that the Li and O atoms diffuse from the core of the nanowires to their surface where they react with Mn atoms and result in formation of $LiMn_2O_4$ during the first discharge cycle. The design of architectures involving a spinel phase shell and a single crystalline layered structure core would allow for durable cathodes for Li ion batteries.

CHAPTER 9

RECOMMENDATIONS FOR FUTURE WORK

- Epitaxial growth of perovskite crystals on nanowire templates: The lack of proper control of perovskite crystal sizes grown on nanoparticles has been identified as the major reason for the inconsistency in performance among different perovskite cells prepared by the same method. Our preliminary TEM investigation also revealed defects such as stacking faults in the perovskite crystals deposited on nanoparticles. Epitaxial growth of perovskites on nanowires, with nanowire acting as epitaxial templates, can be used to address these issues. The knowledge gained from the fundamental studies on redox couples (Chapter 4) can be used for the rationale design of nanowire based electrodes for epitaxial growth of the perovskite crystals.
- Increasing perovskite crystal size by intense pulse light (IPL) sintering: Recombination at grain boundaries results in severe loss of open-circuit voltages of the perovskite cells. IPL has been widely investigated to sinter metal nanoparticles and increase their grain sizes. The technique comprises of a flash of intense light from a xenon arc lamp being incident on the sample. Light absorption followed by relaxation of the electrons from excited states results in dissipation of energy as heat, resulting in the increase in the temperature of the sample for a few milliseconds followed by the rapid cooling of the samples. The perovskite crystals could be sintered using IPL to increase the grain sizes and lower the recombination losses. IPL sintering of perovskite crystals deposited on nanowire based

architectures could also be of significant interest for scalable processing of perovskite solar cells

- The $LiMn_2O4$ shell and Li_2MnO_3 core architecture developed in this thesis could be extended further for improving the battery performance. The Li_2MnO_3 nanowires can be coated with a shell of spinel nanoparticles of nickel cobalt manganese oxide which can contribute to improved voltage of the Li ion battery. The single crystalline layered core would offer improved electrical conductivity and the shell would enable improved voltages and capacity to be achieved.
- In-situ TEM and in-situ XRD during the charging and discharging of Li_2MnO_3 nanowires could be offer more valuable mechanistic insights of spinel $LiMn_2O_4$ shell formation. Li_2MnO_3 is the building block of many layered lithium rich manganese oxide cathodes. Fundamental studies of spinel shell formation on single crystalline Li_2MnO_3 nanowires would provide valuable information for designing better Li rich layered cathode materials.

REFERENCES

1. Smalley, R.E., *Future global energy prosperity: the terawatt challenge.* Mrs Bulletin, 2005. **30**(06): p. 412-417.
2. Lewis, N.S. and D.G. Nocera, *Powering the planet: Chemical challenges in solar energy utilization.* Proceedings of the National Academy of Sciences, 2006. **103**(43): p. 15729-15735.
3. Thompson, A. *CO_2 Levels above 400 PPM Threshold for Third Month in a Row*. Scientific American 2014 [cited 2014 16 October 2014]; Available from: http://www.scientificamerican.com/article/co2-levels-above-400-ppm-threshold-for-third-month-in-a-row/.
4. Law, M., et al., *Nanowire dye-sensitized solar cells.* Nature materials, 2005. **4**(6): p. 455-459.
5. Nelson, J. and R.E. Chandler, *Random walk models of charge transfer and transport in dye sensitized systems.* Coordination Chemistry Reviews, 2004. **248**(13): p. 1181-1194.
6. *Transformational Thick Cathodes with Hierarchical Pore Structure for Enabling High-Energy Lithium Ion Cells at Lower Cost (submitted to DOE)*. [cited 2015 March 18]; Available from: http://ceet.unm.edu/future-directions/pending-proposals/transformational-thick-cathodes-with-hierarchical-pore-structure-for-enabling-high-energy-lithium-ion-cells-at-lower-cost.html.
7. Bard, A.J., *Photoelectrochemistry and heterogeneous photo-catalysis at semiconductors.* Journal of Photochemistry, 1979. **10**(1): p. 59-75.
8. Gerischer, H., *Electrochemical photo and solar cells principles and some experiments.* Journal of Electroanalytical Chemistry and Interfacial Electrochemistry, 1975. **58**(1): p. 263-274.
9. Fujishima, A., *Electrochemical photolysis of water at a semiconductor electrode.* nature, 1972. **238**: p. 37-38.
10. Manassen, J., et al., *Electrochemical, solid state, photochemical and technological aspects of photoelectrochemical energy converters.* 1976.
11. Gibbons, J.F., et al., *A 14% efficient nonaqueous semiconductor/liquid junction solar cell.* Applied Physics Letters, 1984. **45**(10): p. 1095-1097.
12. Wang, M., et al., *An organic redox electrolyte to rival triiodide/iodide in dye-sensitized solar cells.* Nature Chemistry, 2010. **2**(5): p. 385-389.
13. Yum, J.H., et al., *A cobalt complex redox shuttle for dye-sensitized solar cells with high open-circuit potentials.* Nature Communications, 2012. **3**: p. 631.
14. Yella, A., et al., *Porphyrin-sensitized solar cells with cobalt (II/III)–based redox electrolyte exceed 12 percent efficiency.* Science, 2011. **334**(6056): p. 629-634.
15. Daeneke, T., et al., *High-efficiency dye-sensitized solar cells with ferrocene-based electrolytes.* Nature Chemistry, 2011. **3**(3): p. 211-215.
16. Yanagida, S., Y. Yu, and K. Manseki, *Iodine/Iodide-Free Dye-Sensitized Solar Cells.* Accounts of Chemical Research, 2009. **42**(11): p. 1827-1838.
17. Feldt, S.M., et al., *Design of organic dyes and cobalt polypyridine redox mediators for high-efficiency dye-sensitized solar cells.* Journal of the American Chemical Society, 2010. **132**(46): p. 16714-16724.
18. Yella, A., et al., *Porphyrin-sensitized solar cells with cobalt (II/III)–based redox electrolyte exceed 12 percent efficiency.* Science, 2011. **334**(6056): p. 629-634.

19. Kim, H.-S., et al., *Lead iodide perovskite sensitized all-solid-state submicron thin film mesoscopic solar cell with efficiency exceeding 9%.* Scientific reports, 2012. **2**.
20. Wang, Z.-S., K. Sayama, and H. Sugihara, *Efficient eosin Y dye-sensitized solar cell containing Br-/Br3-electrolyte.* The Journal of Physical Chemistry B, 2005. **109**(47): p. 22449-22455.
21. Daeneke, T., et al., *Aqueous Dye-Sensitized Solar Cell Electrolytes Based on the Ferricyanide-Ferrocyanide Redox Couple.* Advanced Materials, 2012. **24**(9): p. 1222-1225.
22. Chen, C.-Y., et al., *Highly efficient light-harvesting ruthenium sensitizer for thin-film dye-sensitized solar cells.* Acs Nano, 2009. **3**(10): p. 3103-3109.
23. Wang, M., et al., *An organic redox electrolyte to rival triiodide/iodide in dye-sensitized solar cells.* Nature Chemistry, 2010. **2**(5): p. 385-389.
24. Li, T.C., et al., *Ni (III)/(IV) bis (dicarbollide) as a fast, noncorrosive redox shuttle for dye-sensitized solar cells.* Journal of the American Chemical Society, 2010. **132**(13): p. 4580-4582.
25. Hattori, S., et al., *Blue copper model complexes with distorted tetragonal geometry acting as effective electron-transfer mediators in dye-sensitized solar cells.* Journal of the American Chemical Society, 2005. **127**(26): p. 9648-9654.
26. Gregg, B.A., et al., *Interfacial recombination processes in dye-sensitized solar cells and methods to passivate the interfaces.* Journal of Physical Chemistry B, 2001. **105**(7): p. 1422-1429.
27. Ito, S., et al., *Fabrication of screen-printing pastes from TiO2 powders for dye-sensitised solar cells.* Progress in photovoltaics: research and applications, 2007. **15**(7): p. 603-612.
28. Huang, S., et al., *Charge recombination in dye-sensitized nanocrystalline TiO2 solar cells.* The Journal of Physical Chemistry B, 1997. **101**(14): p. 2576-2582.
29. Schlichthörl, G., et al., *Band edge movement and recombination kinetics in dye-sensitized nanocrystalline TiO2 solar cells: a study by intensity modulated photovoltage spectroscopy.* The Journal of Physical Chemistry B, 1997. **101**(41): p. 8141-8155.
30. Zhu, K., et al., *Influence of surface area on charge transport and recombination in dye-sensitized TiO2 solar cells.* The Journal of Physical Chemistry B, 2006. **110**(50): p. 25174-25180.
31. Prasittichai, C. and J.T. Hupp, *Surface modification of SnO2 photoelectrodes in dye-sensitized solar cells: significant improvements in photovoltage via Al2O3 atomic layer deposition.* The Journal of Physical Chemistry Letters, 2010. **1**(10): p. 1611-1615.
32. Hamann, T.W., O.K. Farha, and J.T. Hupp, *Outer-sphere redox couples as shuttles in dye-sensitized solar cells. Performance enhancement based on photoelectrode modification via atomic layer deposition.* The Journal of Physical Chemistry C, 2008. **112**(49): p. 19756-19764.
33. Gubbala, S., et al., *Band-Edge Engineered Hybrid Structures for Dye-Sensitized Solar Cells Based on SnO2 Nanowires.* Advanced Functional Materials, 2008. **18**(16): p. 2411-2418.
34. Gubbala, S., et al., *Surface properties of SnO2 nanowires for enhanced performance with dye-sensitized solar cells.* Energy Environ. Sci., 2009. **2**(12): p. 1302-1309.
35. Enache-Pommer, E., B. Liu, and E.S. Aydil, *Electron transport and recombination in dye-sensitized solar cells made from single-crystal rutile TiO2 nanowires.* Physical Chemistry Chemical Physics, 2009. **11**(42): p. 9648-9652.
36. Zhu, K., et al., *Enhanced charge-collection efficiencies and light scattering in dye-sensitized solar cells using oriented TiO2 nanotubes arrays.* Nano Letters, 2007. **7**(1): p. 69-74.

37. Zhang, Z., et al., *The 2,2,6,6-tetramethyl-1-piperidinyloxy radical: An efficient, iodine-free redox mediator for dye-sensitized solar cells.* Advanced Functional Materials, 2008. **18**(2): p. 341-346.
38. Mitzi, D.B., *Thin-film deposition of organic-inorganic hybrid materials.* Chemistry of Materials, 2001. **13**(10): p. 3283-3298.
39. Kojima, A., et al., *Organometal halide perovskites as visible-light sensitizers for photovoltaic cells.* Journal of the American Chemical Society, 2009. **131**(17): p. 6050-6051.
40. Cai, B., et al., *High performance hybrid solar cells sensitized by organolead halide perovskites.* Energy & Environmental Science, 2013. **6**(5): p. 1480-1485.
41. Park, N.-G., *Organometal perovskite light absorbers toward a 20% efficiency low-cost solid-state mesoscopic solar cell.* The Journal of Physical Chemistry Letters, 2013. **4**(15): p. 2423-2429.
42. Heo, J.H., et al., *Efficient inorganic-organic hybrid heterojunction solar cells containing perovskite compound and polymeric hole conductors.* Nature Photonics, 2013. **7**(6): p. 486-491.
43. Qin, P., et al., *Yttrium-substituted nanocrystalline TiO_2 photoanodes for perovskite based heterojunction solar cells.* Nanoscale, 2014. **6**(3): p. 1508-1514.
44. Cha, S.I., et al., *Dye-sensitized solar cells on glass paper: TCO-free highly bendable dye-sensitized solar cells inspired by the traditional Korean door structure.* Energy & Environmental Science, 2012. **5**(3): p. 6071-6075.
45. Dharani, S., et al., *High efficiency electrospun TiO_2 nanofiber based hybrid organic–inorganic perovskite solar cell.* Nanoscale, 2014. **6**(3): p. 1675-1679.
46. Kitazawa, N., et al., *Optical properties of $(C_6H_5C_2H_4NH_3)_2PbI_{4-x}Br_x$ (x= 0–4) mixed-crystal doped PMMA films.* Journal of materials science, 2004. **39**(2): p. 749-751.
47. Liang, K., D.B. Mitzi, and M.T. Prikas, *Synthesis and characterization of organic-inorganic perovskite thin films prepared using a versatile two-step dipping technique.* Chemistry of materials, 1998. **10**(1): p. 403-411.
48. Pradeesh, K., J.J. Baumberg, and G.V. Prakash, *Exciton switching and Peierls transitions in hybrid inorganic-organic self-assembled quantum wells.* Applied Physics Letters, 2009. **95**(17): p. 173305-173305-3.
49. Xia, Y. and G.M. Whitesides, *Soft lithography.* Annual review of materials science, 1998. **28**(1): p. 153-184.
50. Cheng, Z. and J. Lin, *Layered organic–inorganic hybrid perovskites: structure, optical properties, film preparation, patterning and templating engineering.* CrystEngComm, 2010. **12**(10): p. 2646-2662.
51. Stoumpos, C.C., C.D. Malliakas, and M.G. Kanatzidis, *Semiconducting tin and lead iodide perovskites with organic cations: phase transitions, high mobilities, and near-infrared photoluminescent properties.* Inorganic chemistry, 2013. **52**(15): p. 9019-9038.
52. Baikie, T., et al., *Synthesis and crystal chemistry of the hybrid perovskite (CH 3 NH 3) PbI 3 for solid-state sensitised solar cell applications.* Journal of Materials Chemistry A, 2013. **1**(18): p. 5628-5641.
53. Bi, D., et al., *Effect of different hole transport materials on recombination in CH3NH3PbI3 perovskite-sensitized mesoscopic solar cells.* The Journal of Physical Chemistry Letters, 2013. **4**(9): p. 1532-1536.
54. Edri, E., et al., *High open-circuit voltage solar cells based on organic–inorganic lead bromide perovskite.* The Journal of Physical Chemistry Letters, 2013. **4**(6): p. 897-902.
55. Frost, J.M., et al., *Atomistic origins of high-performance in hybrid halide perovskite solar cells.* Nano letters, 2014. **14**(5): p. 2584-2590.

56. Burschka, J., et al., *Sequential deposition as a route to high-performance perovskite-sensitized solar cells.* Nature, 2013. **499**(7458): p. 316-319.
57. Zheng, L., et al., *A hydrophobic hole transporting oligothiophene for planar perovskite solar cells with improved stability.* Chemical Communications, 2014. **50**(76): p. 11196-11199.
58. Niu, G., et al., *Study on the stability of $CH_3NH_3PbI_3$ films and the effect of post-modification by aluminum oxide in all-solid-state hybrid solar cells.* Journal of Materials Chemistry A, 2014. **2**(3): p. 705-710.
59. Li, W., et al., *Post modification of perovskite sensitized solar cells by aluminum oxide for enhanced performance.* Journal of Materials Chemistry A, 2013. **1**(38): p. 11735-11740.
60. Tarascon, J.-M. and M. Armand, *Issues and challenges facing rechargeable lithium batteries.* Nature, 2001. **414**(6861): p. 359-367.
61. Fergus, J.W., *Recent developments in cathode materials for lithium ion batteries.* Journal of Power Sources, 2010. **195**(4): p. 939-954.
62. Yu, H. and H. Zhou, *High-energy cathode materials (Li2MnO3–LiMO2) for lithium-ion batteries.* The Journal of Physical Chemistry Letters, 2013. **4**(8): p. 1268-1280.
63. Capsoni, D., et al., *Inhibition of Jahn-Teller cooperative distortion in LiMn2O4 spinel by Ga3+ doping.* The Journal of Physical Chemistry B, 2002. **106**(30): p. 7432-7438.
64. Jang, D.H., Y.J. Shin, and S.M. Oh, *Dissolution of Spinel Oxides and Capacity Losses in 4 V Li/Li x Mn2 O 4 Cells.* Journal of The Electrochemical Society, 1996. **143**(7): p. 2204-2211.
65. Ouyang, C., S. Shi, and M. Lei, *Jahn–Teller distortion and electronic structure of LiMn 2 O 4.* Journal of Alloys and Compounds, 2009. **474**(1): p. 370-374.
66. Aurbach, D., *Review of selected electrode–solution interactions which determine the performance of Li and Li ion batteries.* Journal of Power Sources, 2000. **89**(2): p. 206-218.
67. Wang, E., et al., *Stability of lithium ion spinel cells. III. Improved life of charged cells.* Journal of The Electrochemical Society, 2000. **147**(11): p. 4023-4028.
68. Du Pasquier, A., et al., *Mechanism for Limited 55° C Storage Performance of Li1. 05Mn1. 95 O 4 Electrodes.* Journal of The Electrochemical Society, 1999. **146**(2): p. 428-436.
69. Freitag, R. and J. Conradie, *Understanding the Jahn–Teller Effect in Octahedral Transition-Metal Complexes: A Molecular Orbital View of the Mn (β-diketonato) 3 Complex.* Journal of Chemical Education, 2013. **90**(12): p. 1692-1696.
70. Yamada, A., *Lattice instability in Li (Li x Mn 2− x) O 4.* Journal of Solid State Chemistry, 1996. **122**(1): p. 160-165.
71. Thackeray, M.M., et al., *Structural Fatigue in Spinel Electrodes in High Voltage (4 V) Li/Li x Mn2 O 4 Cells.* Electrochemical and Solid-State Letters, 1998. **1**(1): p. 7-9.
72. Ammundsen, B. and J. Paulsen, *Novel Lithium-Ion Cathode Materials Based on Layered Manganese Oxides.* Advanced Materials, 2001. **13**(12-13): p. 943-956.
73. Kalyani, P., et al., *Lithium metal rechargeable cells using Li 2 MnO 3 as the positive electrode.* Journal of power sources, 1999. **80**(1): p. 103-106.
74. Armstrong, A.R., et al., *Demonstrating oxygen loss and associated structural reorganization in the lithium battery cathode Li [Ni0. 2Li0. 2Mn0. 6] O2.* Journal of the American Chemical Society, 2006. **128**(26): p. 8694-8698.
75. Pasero, D., L. Gillie, and A.R. West, *Lithium (De) Intercalation Capacity of Li1. 93Mn0. 97Ni0. 10O3− δ Role of Oxygen Deficiency.* Electrochemical and Solid-State Letters, 2005. **8**(8): p. A392-A395.
76. Robertson, A.D. and P.G. Bruce, *Mechanism of electrochemical activity in Li2MnO3.* Chemistry of Materials, 2003. **15**(10): p. 1984-1992.

77. Wu, X., et al., *Facile synthesis of Li_2MnO_3 nanowires for lithium-ion battery cathodes.* New Journal of Chemistry, 2014. **38**(2): p. 584-587.
78. Rana, J., et al., *Structural Changes in Li2MnO3 Cathode Material for Li-Ion Batteries.* Advanced Energy Materials, 2014. **4**(5).
79. Lee, H.-W., et al., *Ultrathin spinel LiMn2O4 nanowires as high power cathode materials for Li-ion batteries.* Nano letters, 2010. **10**(10): p. 3852-3856.
80. Kim, D.K., et al., *Spinel LiMn2O4 nanorods as lithium ion battery cathodes.* Nano Letters, 2008. **8**(11): p. 3948-3952.
81. Kim, K.J. and J.H. Lee, *Effects of nickel doping on structural and optical properties of spinel lithium manganate thin films.* Solid state communications, 2007. **141**(2): p. 99-103.
82. Capsoni, D.B., M.; Chiodelli, G.; Massarotti, V.; Azzoni, C. B.; Mozzati, M. C.,Comin, A. , *Inhibition of Jahn–Teller cooperative distortion in LiMn2O4 spinel by transition metal ion doping.* Physical Chemistry Chemical Physics, 2001. **3**: p. 2162.
83. Tsuji, T., H. Umakoshi, and Y. Yamamura, *Thermodynamic properties of undoped and Fe-doped LiMn 2 O 4 at high temperature.* Journal of Physics and Chemistry of Solids, 2005. **66**(2): p. 283-287.
84. Thirunakaran, R., et al., *Significance of Mg doped LiMn2O4 spinels as attractive 4 V cathode materials for use in lithium batteries.* Ionics, 2001. **7**(3): p. 187-191.
85. Ding, Y., et al., *Enhanced elevated-temperature performance of Al-doped single-crystalline LiMn2O4 nanotubes as cathodes for lithium ion batteries.* The Journal of Physical Chemistry C, 2011. **115**(19): p. 9821-9825.
86. Mori, D., et al., *Synthesis, phase relation and electrical and electrochemical properties of ruthenium-substituted Li 2 MnO 3 as a novel cathode material.* Journal of Power Sources, 2011. **196**(16): p. 6934-6938.
87. Kim, S., et al., *Effects of transition metal doping and surface treatment to improve the electrochemical performance of Li2MnO3.* Journal of Electroceramics, 2013. **30**(3): p. 159-165.
88. Gao, Y., et al., *Improved electron/Li-ion transport and oxygen stability of Mo-doped Li 2 MnO 3.* Journal of Materials Chemistry A, 2014. **2**(13): p. 4811-4818.
89. Xu, G., et al., *Strategies for improving the cyclability and thermo-stability of LiMn 2 O 4-based batteries at elevated temperatures.* Journal of Materials Chemistry A, 2015.
90. Sun, Y.-K., et al., *Electrochemical performance of nano-sized ZnO-coated LiNi 0.5 Mn 1.5 O 4 spinel as 5 V materials at elevated temperatures.* Electrochemistry Communications, 2002. **4**(4): p. 344-348.
91. Wu, Y. and A. Manthiram, *Effect of surface modifications on the layered solid solution cathodes (1− z) Li [Li 1/3 Mn 2/3] O 2−(z) Li [Mn 0.5− y Ni 0.5− y Co 2y] O 2.* Solid State Ionics, 2009. **180**(1): p. 50-56.
92. Ying, J., C. Wan, and C. Jiang, *Surface treatment of LiNi 0.8 Co 0.2 O 2 cathode material for lithium secondary batteries.* Journal of power sources, 2001. **102**(1): p. 162-166.
93. Sun, Y.K., et al., *The Role of AlF3 Coatings in Improving Electrochemical Cycling of Li-Enriched Nickel-Manganese Oxide Electrodes for Li-Ion Batteries.* Advanced Materials, 2012. **24**(9): p. 1192-1196.
94. Wu, F., et al., *Spinel/Layered Heterostructured Cathode Material for High-Capacity and High-Rate Li-Ion Batteries.* Advanced Materials, 2013. **25**(27): p. 3722-3726.
95. Wu, F., et al., *Ultrathin Spinel Membrane-Encapsulated Layered Lithium-Rich Cathode Material for Advanced Li-Ion Batteries.* Nano letters, 2014.
96. Zhang, S., K. Xu, and T. Jow, *A thermal stabilizer for LiPF6-based electrolytes of Li-ion cells.* Electrochemical and solid-state letters, 2002. **5**(9): p. A206-A208.

97. Li, W., et al., *Additives for stabilizing LiPF6-based electrolytes against thermal decomposition.* Journal of The Electrochemical Society, 2005. **152**(7): p. A1361-A1365.
98. Li, Y., et al., *Effect of heptamethyldisilazane as an additive on the stability performance of LiMn 2 O 4 cathode for lithium-ion battery.* Journal of Power Sources, 2009. **189**(1): p. 685-688.
99. Kim, J.H., et al., *Design of an efficient microwave plasma reactor for bulk production of inorganic nanowires.* Informacije MIDEM, 2008. **38**: p. 237-243.
100. Kumar, V., et al., *Alkali-assisted, atmospheric plasma production of titania nanowire powders and arrays.* Crystal Growth & Design, 2011. **11**(7): p. 2913-2919.
101. Kumar, V., et al., *Gas-Phase, Bulk Production of Metal Oxide Nanowires and Nanoparticles Using a Microwave Plasma Jet Reactor.* The Journal of Physical Chemistry C, 2008. **112**(46): p. 17750-17754.
102. Kumar, V., *Novel scalable, atmospheric plasma based manufacturing methods for metal oxide nanowires*. 2011.
103. *Waveguide Theory and Operation*. Available from: http://www.navymars.org/national/training/nmo_courses/nmo1/module11/14183_ch1.pdf.
104. George, S.M., *Atomic layer deposition: an overview.* Chemical reviews, 2009. **110**(1): p. 111-131.
105. Yan, X.-T. and Y. Xu, *Chemical vapour deposition: an integrated engineering design for advanced materials*. 2010: Springer.
106. Besra, L. and M. Liu, *A review on fundamentals and applications of electrophoretic deposition (EPD).* Progress in materials science, 2007. **52**(1): p. 1-61.
107. Qin, P., et al., *Inorganic hole conductor-based lead halide perovskite solar cells with 12.4% conversion efficiency.* Nature communications, 2014. **5**.
108. Tsujimoto, K., et al., *TiO2 surface treatment effects by Mg2+, Ba2+, and Al3+ on Sb2S3 extremely thin absorber solar cells.* The Journal of Physical Chemistry C, 2012. **116**(25): p. 13465-13471.
109. Nelson, J., *The physics of solar cells*. Vol. 57. 2003: World Scientific.
110. Van de Lagemaat, J. and A. Frank, *Nonthermalized electron transport in dye-sensitized nanocrystalline TiO2 films: transient photocurrent and random-walk modeling studies.* The Journal of Physical Chemistry B, 2001. **105**(45): p. 11194-11205.
111. Kopidakis, N., et al., *Ambipolar diffusion of photocarriers in electrolyte-filled, nanoporous TiO2.* The Journal of Physical Chemistry B, 2000. **104**(16): p. 3930-3936.
112. Williams, D.B. and C.B. Carter, *Transmission Electron Microscopy Plenum.* New York, NY, 1996.
113. Chattopadhyay, K., *Introduction To Nanoscience And Nenotechnology*. 2009: PHI Learning Pvt. Ltd.
114. Warren, B.E., *X-ray Diffraction*. 1969: Courier Dover Publications.
115. Klug, H.P. and L.E. Alexander, *X-ray diffraction procedures: for polycrystalline and amorphous materials.* X-Ray Diffraction Procedures: For Polycrystalline and Amorphous Materials, 2nd Edition, by Harold P. Klug, Leroy E. Alexander, pp. 992. ISBN 0-471-49369-4. Wiley-VCH, May 1974., 1974. **1**.
116. Deiana, C., et al., *Surface structure of TiO2 P25 nanoparticles: infrared study of hydroxy groups on coordinative defect sites.* The Journal of Physical Chemistry C, 2010. **114**(49): p. 21531-21538.

117. Li, Z., X. Zhang, and G. Lu, *Electron Dynamics in Dye-Sensitized Solar Cells: Effects of Surface Terminations and Defects.* The Journal of Physical Chemistry B, 2010. **114**(51): p. 17077-17083.
118. Lin, L.Y., et al., *Low-temperature flexible Ti/TiO2 photoanode for dye-sensitized solar cells with binder-free TiO2 paste.* Progress in Photovoltaics: Research and Applications, 2012. **20**(2): p. 181-190.
119. Vendra, V.K., et al., *Photoanode Area Dependent Efficiency and Recombination Effects in Dye-Sensitized Solar Cells.* Journal of The Electrochemical Society, 2012. **159**(8): p. H728-H733.
120. Liang, L.Y., et al., *Porosity effects on electron transport in TiO2 films and its application to dye-sensitized solar cells.* Journal of Physical Chemistry B, 2006. **110**(25): p. 12404-12409.
121. Gubbala, S., et al., *Surface properties of SnO2 nanowires for enhanced performance with dye-sensitized solar cells.* Energy & Environmental Science, 2009. **2**(12): p. 1302-1309.
122. Wang, H., et al., *Electrochemical investigation of traps in a nanostructured TiO2 film.* The Journal of Physical Chemistry B, 2001. **105**(13): p. 2529-2533.
123. Hagfeldt, A., et al., *Dye-sensitized solar cells.* Chemical Reviews, 2010. **110**(11): p. 6595-6663.
124. Tian, H. and L. Sun, *Iodine-free redox couples for dye-sensitized solar cells.* Journal of Materials Chemistry, 2011. **21**(29): p. 10592-10601.
125. Cheng, M., et al., *Efficient dye-sensitized solar cells based on an iodine-free electrolyte using L-cysteine/L-cystine as a redox couple.* Energy & Environmental Science, 2012. **5**(4): p. 6290-6293.
126. Li, D., et al., *Non-Corrosive, Non-Absorbing Organic Redox Couple for Dye-Sensitized Solar Cells.* Advanced Functional Materials, 2010. **20**(19): p. 3358-3365.
127. Feldt, S.M., et al., *Characterization of Surface Passivation by Poly(methylsiloxane) for Dye-Sensitized Solar Cells Employing the Ferrocene Redox Couple.* Journal of Physical Chemistry C, 2010. **114**(23): p. 10551-10558.
128. Hamann, T.W., O.K. Farha, and J.T. Hupp, *Outer-Sphere Redox Couples as Shuttles in Dye-Sensitized Solar Cells. Performance Enhancement Based on Photoelectrode Modification via Atomic Layer Deposition.* Journal of Physical Chemistry C, 2008. **112**(49): p. 19756-19764.
129. Jiayan Cong , X.Y., Lars Kloo and Licheng Sun, *Iodine/iodide-free redox shuttles for liquid electrolyte-based dye-sensitized solar cells.* Energy & Environmental Science, 2012: p. Advance Article.
130. Gubbala, S., et al., *Band-edge engineered hybrid structures for dye-sensitized solar cells based on SnO2 nanowires.* Advanced Functional Materials, 2008. **18**(16): p. 2411-2418.
131. Barnes, P.R.F., et al., *Simulation and measurement of complete dye sensitised solar cells: including the influence of trapping, electrolyte, oxidised dyes and light intensity on steady state and transient device behaviour.* Physical Chemistry Chemical Physics, 2011. **13**(13): p. 5798-5816.
132. Zaban, A., M. Greenshtein, and J. Bisquert, *Determination of the electron lifetime in nanocrystalline dye solar cells by open-circuit voltage decay measurements.* Chemphyschem, 2003. **4**(8): p. 859-864.
133. Law, M., et al., *ZnO-Al2O3 and ZnO-TiO2 core-shell nanowire dye-sensitized solar cells.* The Journal of Physical Chemistry B, 2006. **110**(45): p. 22652-22663.
134. Paracchino, A., et al., *Ultrathin films on copper (i) oxide water splitting photocathodes: a study on performance and stability.* Energy & Environmental Science, 2012. **5**(9): p. 8673-8681.

135. Kavan, L., et al., *Electrochemical and photoelectrochemical investigation of single-crystal anatase.* Journal of the American Chemical Society, 1996. **118**(28): p. 6716-6723.
136. Daeneke, T., et al., *Dye regeneration kinetics in dye-sensitized solar cells.* Journal of the American Chemical Society, 2012. **134**(41): p. 16925-16928.
137. Feldt, S.M., et al., *Regeneration and recombination kinetics in cobalt polypyridine based dye-sensitized solar cells, explained using Marcus theory.* Phys. Chem. Chem. Phys., 2013. **15**(19): p. 7087-7097.
138. Fabregat-Santiago, F., et al., *Electron transport and recombination in solid-state dye solar cell with spiro-OMeTAD as hole conductor.* Journal of the American Chemical Society, 2008. **131**(2): p. 558-562.
139. Hao, F., et al., *Lead-free solid-state organic-inorganic halide perovskite solar cells.* Nature Photonics, 2014.
140. Choudalakis, G. and A.D. Gotsis, *Permeability of polymer/clay nanocomposites: a review.* European Polymer Journal, 2009. **45**(4): p. 967-984.
141. Paul, D.R. and L.M. Robeson, *Polymer nanotechnology: nanocomposites.* Polymer, 2008. **49**(15): p. 3187-3204.
142. Su, Y., et al., *Impermeable barrier films and protective coatings based on reduced graphene oxide.* Nature Communications, 2014. **5**.
143. Kumar, N.A., et al., *Polyaniline-grafted reduced graphene oxide for efficient electrochemical supercapacitors.* ACS nano, 2012. **6**(2): p. 1715-1723.
144. Xu, B., et al., *Identifying surface structural changes in layered Li-excess nickel manganese oxides in high voltage lithium ion batteries: A joint experimental and theoretical study.* Energy & Environmental Science, 2011. **4**(6): p. 2223-2233.
145. Yong, Y.-C., et al., *Macroporous and monolithic anode based on polyaniline hybridized three-dimensional graphene for high-performance microbial fuel cells.* ACS nano, 2012. **6**(3): p. 2394-2400.
146. Hou, J., Z. Liu, and P. Zhang, *A new method for fabrication of graphene/polyaniline nanocomplex modified microbial fuel cell anodes.* Journal of Power Sources, 2013. **224**: p. 139-144.
147. Wang, G., S. Zhuo, and W. Xing, *Graphene/polyaniline nanocomposite as counter electrode of dye-sensitized solar cells.* Materials Letters, 2012. **69**: p. 27-29.
148. Wang, H., et al., *Graphene oxide doped polyaniline for supercapacitors.* Electrochemistry Communications, 2009. **11**(6): p. 1158-1161.
149. Wang, L., et al., *Graphene-based polyaniline nanocomposites: preparation, properties and applications.* Journal of Materials Chemistry A, 2014. **2**(13): p. 4491-4509.
150. Ebrahim, S., et al., *Dye-Sensitized Solar Cell Based on Polyaniline/Multiwalled Carbon Nanotubes Counter Electrode.* International Journal of Photoenergy, 2013. **2013**.
151. Chen, Z., et al., *Shape-controlled synthesis of organolead halide perovskite nanocrystals and their tunable optical absorption.* Materials Research Express, 2014. **1**(1): p. 015034.
152. Quarti, C., et al., *The Raman Spectrum of the $CH_3NH_3PbI_3$ Hybrid Perovskite: Interplay of Theory and Experiment.* The Journal of Physical Chemistry Letters, 2013. **5**(2): p. 279-284.
153. Christians, J.A., R.C.M. Fung, and P.V. Kamat, *An inorganic hole conductor for organo-lead halide perovskite solar cells. Improved hole conductivity with copper iodide.* Journal of the American Chemical Society, 2013. **136**(2): p. 758-764.
154. Im, J.-H., et al., *Growth of $CH_3NH_3PbI_3$ cuboids with controlled size for high-efficiency perovskite solar cells.* Nature nanotechnology, 2014. **9**(11): p. 927-932.
155. Cheng, F., et al., *Facile controlled synthesis of MnO2 nanostructures of novel shapes and their application in batteries.* Inorganic chemistry, 2006. **45**(5): p. 2038-2044.

156. Wang, X. and Y. Li, *Selected-control hydrothermal synthesis of α-and β-MnO2 single crystal nanowires.* Journal of the American Chemical Society, 2002. **124**(12): p. 2880-2881.
157. Wang, X., et al., *Sol–gel template synthesis of highly ordered MnO2 nanowire arrays.* Journal of Power Sources, 2005. **140**(1): p. 211-215.
158. Cvelbar, U., *Towards large-scale plasma-assisted synthesis of nanowires.* Journal of Physics D: Applied Physics, 2011. **44**(17): p. 174014.
159. Ostrikov, K.K., U. Cvelbar, and A.B. Murphy, *Plasma nanoscience: setting directions, tackling grand challenges.* Journal of Physics D: Applied Physics, 2011. **44**(17): p. 174001.
160. Amalraj, S.F., et al., *Study of the nanosized Li_2MnO_3: Electrochemical behavior, structure, magnetic properties, and vibrational modes.* Electrochimica Acta, 2013. **97**: p. 259-270.
161. Chernomordik, B.D., et al., *Photoelectrochemical activity of as-grown, α-Fe_2O_3 nanowire array electrodes for water splitting.* Nanotechnology, 2012. **23**(19): p. 194009.
162. Park, S.-H., et al., *Powder property and electrochemical characterization of Li_2MnO_3 material.* Materials chemistry and physics, 2007. **102**(2): p. 225-230.
163. Park, S.-H., et al., *Powder property and electrochemical characterization of Li_2MnO_3 material.* Materials chemistry and physics, 2007. **102**(2): p. 225-230.
164. Xiong, L., et al., *Excellent stability of spinel LiMn 2 O 4-based composites for lithium ion batteries.* Journal of Materials Chemistry, 2012. **22**(47): p. 24563-24568.
165. Thackeray, M.M., et al., *Li_2MnO_3-stabilized $LiMO_2$ (M= Mn, Ni, Co) electrodes for lithium-ion batteries.* Journal of Materials Chemistry, 2007. **17**(30): p. 3112-3125.
166. Choa, J. and M.M. Thackeray, *Structural Changes of LiMn2 O 4 Spinel Electrodes during Electrochemical Cycling.* Journal of The Electrochemical Society, 1999. **146**(10): p. 3577-3581.
167. Lin, F., et al., *Surface reconstruction and chemical evolution of stoichiometric layered cathode materials for lithium-ion batteries.* Nature communications, 2014. **5**.
168. Jiao, F., et al., *Synthesis of ordered mesoporous Li–Mn–O spinel as a positive electrode for rechargeable lithium batteries.* Angewandte Chemie International Edition, 2008. **47**(50): p. 9711-9716.
169. Robertson, D.A., Armstrong, A. Robert; Bruce, P.G., *Layered LixMn1-yCoyO2 Intercalation ElectrodesInfluence of Ion Exchange on Capacity and Structure upon Cycling*

Chem. Mater., 2001. **13**(7): p. 2380-2386.
170. Song, B., et al., *Structural evolution and the capacity fade mechanism upon long-term cycling in Li-rich cathode material.* Physical Chemistry Chemical Physics, 2012. **14**(37): p. 12875-12883.
171. Francis Amalraj, S., et al., *Study of the electrochemical behavior of the "inactive" Li_2MnO_3.* Electrochimica Acta, 2012. **78**: p. 32-39.

APPENDIX 1

Calculation of weight % of Li_2MnO_3 (W1) and $LiMn_2O_4$ (W2)

(a) From HRTEM measurements.

The diameter of the core (D_{core}), and total NW diameter (D_{total}) are measured for the Li_2MnO_3 NWs charged and discharged to several cycles and the following formula is compute the weight %.

$$Weight\ \%\ of\ core = \frac{V_{core} * \rho_{core}}{V_{core} * \rho_{core} + V_{shell} * \rho_{shell}}$$

$$= \frac{D_{core}^2 * \rho_{core}}{D_{core}^2 * \rho_{core} + (D_{total}^2 - D_{core}^2) * \rho_{shell}}$$

where V is the volume and ρ is the density

In case of a $LiMn_2O_4$ shell and Li_2MnO_3 core nanowire, diameter of the core = 31.5 nm ad total NW diameter= 56 nm (From Figure 7.9)

Weight % of Li_2MnO_3 core is calculated as 29.8 % and Weight % of $LiMn_2O_4$ shell is 70.1 %

Similarily for NWs where the core is in the form of $(Li_2O)_x .MnO_2$ (x is very small < 0.12) (core diameter = 15 nm and total nanowire diamter = 55 nm, From Figure 7.9), weight % of $(Li_2O)_x .MnO_2$ core = 7.4 , weight % of $LiMn_2O_4$shell is 92.6 %.

(b) From the charge-discharge curves

W1 + W2 = 1

From the charge and discharge profile, 75 mAh/g (From Figure 7.6) can be taken as the intial capacity of Li_2MnO_3. The first charge-discharge cycle does not show any plateau region near 4V, and hence $LiMn_2O_4$ fraction can be neglected in the first cycle. Based on an earlier report, the capacity of $LiMn_2O_4$ at 5 C is 108 mAh/g.[79]

Hence, W1 (75) + W2 (108) = C_{obs}

Where C_{obs} is the observed experimental capacity.

Based on these two equations the relative weight fraction of Li_2MnO_3 and $LiMn_2O_4$ at different cycles can be calculated and are summarized in the following table.

Table S1. Relative weight fractions of of Li_2MnO3 and $LiMn_2O_4$ at different cycles

Cycle number	Wt % of Li_2MnO_3	Wt % of $LiMn_2O_4$
1	100	0
5	81.1	18.9
10	62.1	37.9
30	43.2	56.8
40	24.2	75.8
100	15.1	84.9

CURRICULUM VITAE

Venkat Kalyan Vendra
v0vend01@louisville.edu
Doctoral Student, (315) 262-4352
Conn Center for Renewable Energy Research,
Department of Chemical Engineering,
University of Louisville,
Louisville, KY 40292.

Career Objective: To work with a strong multi-disciplinarian team involved in semiconductor research and development. Strongly motivated and highly interested in solving new challenges through collaboration and leadership.

Education

University of Louisville–Louisville, KY March 2015 (expected)
Doctor of Philosophy in Chemical Engineering,
Cumulative G.P.A 4.0/4.0
Thesis Advisors: Dr. Mahendra K. Sunkara and Dr. Delaina A. Amos

Clarkson University–Potsdam, NY May 2010
Master of Science in Chemical Engineering,
Cumulative G.P.A 3.92/4.0
Thesis Advisor: Dr. Sitaraman Krishnan

Andhra University –Visakhapatnam, India May 2008
Bachelor of Technology in Chemical Engineering,
Overall percentage 85.1 % (Top 4 in Class of 80 students)

Achievements

Peer Reviewed Publications

1. Vendra, V.K.,Absher, J., Ellis, S., Druffel, T., Amos, D., Sunkara, M.K., Photoanode area dependent efficiency and recombination effects in dye-sensitized solar cells, *Journal of Electrochemical Society* 2012, 159, H728-H733.
2. Pendyala, C., Jacinski, J., Kim, J.-H., Vendra, V.K., Sheetz, R.M., Menon, M., Sunkara, M.K., Nanowires as semi-rigid substrates for growth of thick, $In_xGa_{1-x}N(x>0.4)$ epi-layers without phase segregation for photoelectrochemical water splitting, *Nanoscale* 2012, 4, 6269-6275.

3. Sunkara, S., Vendra, V.K., Kim, J.H., Druffel, T., Sunkara, M.K., Scalable synthesis of copper oxide nanowires and their photoelectrochemical properties, *Catalysis Today* 2013, 199, 27-35.
4. Lupitsky, R., Vendra, V.K., Jasinski, J., Amos, D., Sunkara, M.K., Druffel, T., Towards high efficiency dye-sensitized solar cells with a photoanode fabricated via a simple water based formulation. *Progress in Photovoltaics* (Early view, DOI: 10.1002/pip.2502).
5. Moganty, S.S., Chinthamanipeta, P.S., Close, J.J.,Vendra,V.K., Krishnan, S., Baltus, R.E., Thermodyanmic and transport properties of 1,3-dialkylimidazolium ionic liquids for CO_2 capture, Chemical Engineering Journal 2014, 250, 377-389.
6. Vendra, V.K., Nguyen, T., Druffel, T., Amos, D., Sunkara, M.K., Nanowire architectures for iodide free dye-sensitized solar cells, *J. Mater. Chem. A.* 2014, 2, 3543-3550.
7. Nguyen, T., Thapa, A., Vendra, V.K., Jasinski, J., Sunkara, M.K., High rate capacity retention in binder free titania coated tin oxide nanowires for Li ion batteries, *RSC Advances* 2014, 4, 3312-3317.
8. Martinez, A., Vendra, V.K.,Sunkara, S., Haldankar, P., Sunkara, M.K., Tungsten oxide coated copper oxide nanowire arrays for enhanced activity and durability with photoelectrochemical water splitting, *Journal of Materials Chemistry A* 2013, 1, 15235-15241.
9. Sunkara, S., Vendra, V.K., Jasinski, J., Deutsch, T., Andriotis, A.N., Menon, M., Sunkara, M.K., New Visible Light Absorbing Materials for Solar Fuels, $Ga(Sb_x)N_{1-x}$ Alloys. *Advanced Materials* 2014, 26, 2878-2882.
10. Myrick, J.M., Vendra, V.K., Krishnan, S., Self-assembled polysaccharide nanostructures for controlled release applications, *Nanotechnology Reviews* 2014, Accepted.
11. Trada, H., Vendra, V.K.,Tinney, J.P., Jackson, D.J., Walsh, K.M., Keller, B.B., Development of a thin-film porous microelectrode array sensor for electrical stimulation of engineered cardiac tissue, *Manuscript Under Review*.
12. Vendra, V.K., Myrick, J.M., Sexton, F., Krishnan, S., Self-assembled hydroxypropyl cellulose for sustained oral delivery of biomolecules. *Manuscript in preparation*.
13. Vendra, V.K.,Thapa, A.K., Jasinksi, J., Nguyen, T.Q., Sunkara, M.K., Scalable Synthesis and Surface Stabilization of Li_2MnO_3 Nanowires (NWs) for High Rate Cathode Materials in Li-Ion Batteries, *Manuscript Submitted.*
14. Nguyen, T.Q., Vendra, V.K., Thapa, A.K., Jasinksi, J., Sumanasekara, G., Sunkara, M.K., Large Scale Solvo-plasma Production of Tin Oxide Nanowires for Energy Applications, *Manuscript Under Preparation*.
15. Rajamanickam, N., Vendra, V.K.,Kumari, S., Lavery, B.W., Ramachandran, K., Druffel, T., Sunkara, M.K. Moisture resistant methyl ammonium lead iodide perovskite solar cells. *Manuscript Submitted*.
16. Vendra, V.K.,Kumari, S., Lavery, B.W., Rajamanickam, N., Druffel, T., Sunkara, M.K. Atmospheric roll to roll processing in perovskite solar cells. *Manuscript under preparation.*

Book Chapter

1. Vendra, V.K., Wu, L., Krishnan, S., Polymer thin films for biomedical applications, Nanostructured Thin Films and Surfaces, Kumar, C. S. S. R., Ed., Nanomaterials for the Life Sciences, Vol. 5, Wiley, Weinheim.

Patents

1. Sexton, F.A., Krishnan, S., Vendra, V.K., Sustained release of nutrients *In Vivo*, *U.S. Pat. Appl.Publ.*, US 20090155409 A1 20090618, (2009).
2. Sexton, F.A. Krishnan, S., Vendra, V.K., Sustained release of nutrients in a time controlled manner, *PCT Int. Appl.,* WO 2010080557 A1 20100715, (2010).

Awards & Accolades

- Third prize for poster presentation at RE3 workshop on renewable energy, Louisville, KY (2013)
- Third prize for poster presentation at Kentucky Statewide Workshop on Renewable Energy and Energy Efficiency (2010)
- Awarded A+ grade (given to top student in the class) in Physical Electronics and Semiconductor Fundamental Courses offered by the Electrical Engineering Department at University of Louisville
- Most Creative Poster Award for the poster presented at Center for Advanced Materials Processing Annual Technical Meeting, Canandaigua, New York (2009).
- Second Prize in technical quiz competition conducted by Indian Institute of Chemical Engineers, Visakhapatnam (2007).

Talks at International Conferences (Underline indicates presenting author):

- Vendra, V.K., Nguyen, T., Amos, D., Druffel, T., Sunkara, M.K., Nanowire Architectures for Iodide free Dye-Sensitized Solar cells, ECS, Orlando, FL (2014)
- Vendra, V.K., Nguyen, T., Amos, D., Druffel, T., Sunkara, M.K., Tin Oxide Nanowires and Their Hybrid Architectures for Kinetically Fast Redox Couples in Dye-Sensitized Solar Cells, ECS Prime, Honoululu, Hawaii (2012).
- Vendra, V.K., Thapa, A., Sunkara, S., Nguyen, T., Sunkara, M.K., Production of Manganese Oxide Nanowire Powders and Their Characterization for Li Ion Batteries and Capacitors, ECS Prime, Honoululu, Hawaii (2012).
- Vendra, V.K., Absher, J., Ellis, S., Druffel, T., Amos, D., Sunkara, M.K., Photanode area dependent efficiency and recombination in dye-sensitized solar cells, AICHE 2011 Annual Meeting, Minneapolis, Minnesota (2011).
- Vendra, V.K., Druffel, T., Amos, D., Sunkara, M.K., Fundamental investigation of electron transport and recombination in titania nanowire/nanoparticle hybrid structures, AICHE 2011 Annual Meeting, Minneapolis, Minnesota (2011).

- Vendra, V.K., Pendyala, C., Kim, J.H., Sunkara, M.K., Synthesis of ternary InGaN alloys, on GaN nanowire substrates AICHE 2011 Annual Meeting, Minneapolis, Minnesota (2011).
- Vendra V.K., Sudheer, S., New methods for degradation of organic and inorganic effluents in chemical industries, ChemInsight 07, Indian Institute of Technology, Kharagpur, India (2007).

Poster Presentations

- Vendra, V.K., Nguyen T., Druffel, T., Amos, D., Sunkara, M.K., Titania nanoparticle-Tin oxide nanowire hybrid architectures for using alternate redox electrolytes in dye-sensitized solar cells, Materials Research Society Fall meeting, Boston, MA (2012).
- Vendra, V.K., Absher, J., Ellis, S., Druffel, T., Amos, D., Sunkara, M.K., Photanode area dependent efficiency and recombination in dye-sensitized solar cells, Kentucky State wide Workshop on Renewable Energy and Energy Efficiency, Louisville, KY (2010).
- Moganty, S.S., Kumar, P., Vendra, V.K., Krishnan, S., Baltus, R.E., Novel Ionic Liquids for CO_2 capture, AICHE 2009 Annual Meeting, Nashville, Tennessee (2009).
- Krishnan, S., Wu, L., Vendra, V.K., Lalitha, G., Functional Fluorinated Polymers as Anti-Biofouling Coatings and Ion Conducting Polymer Electrolytes, Center for Advanced Materials Processing Annual technical meeting, Canandaigua, New York (2009).

Experimental Skills and Expertise: Atomic layer deposition, Chemical vapor deposition, Semiconductor photoelectrochemistry, Materials characterization techniques: X-ray diffraction, scanning electron microscopy, energy dispersive X-ray spectroscopy, Raman spectroscopy, Electrochemical characterization of solar cells and Li-ion batteries: cyclic voltammetry, chronoamperometry and chronopotentiometry.

Relevant Coursework: Chemical Vapor Deposition, Physical Electronics, Semiconductor Principles, Electroanalytical Chemistry, Polymer Science and Engineering, Materials Characterization

Mentoring experience

- Mentored several high school students for science fair projects
- Mentored 2 undergraduate students and 1 Master Degree student for their research projects
- Taught a class of college freshman on fabrication and characterization of dye-sensitized solar cells

Professional Memberships

- American Institute of Chemical Engineers
- Electrochemical Society
- Materials Research Society